Copyright

by

Harry Chou

2018

The Dissertation Committee for Harry Chou Certifies that this is the approved version of the following Dissertation:

Two-Dimensional Materials Synthesis, Characterization, and Devices: Working with Hexagonal Boron Nitride and Graphene

Committee:

Sanjay K. Banerjee, Supervisor

Rodney S. Ruoff

Deji Akinwande

Emanuel Tutuc

Paul S. Ho

Luigi Colombo

Two-Dimensional Materials Synthesis, Characterization, and Devices: Working with Hexagonal Boron Nitride and Graphene

by

Harry Chou

Dissertation

Presented to the Faculty of the Graduate School of

The University of Texas at Austin

in Partial Fulfillment

of the Requirements

for the Degree of

Doctor of Philosophy

The University of Texas at Austin

August 2018

Dedication

For my sister, Eyleen. I wish every day that I could see you again.

Acknowledgements

My sister Eyleen died by suicide in August of 2013 after a relatively short and intense battle with mental illness. Her diagnosis and treatment were still unsettled when she died and showed how far there is to still go in these areas for mental healthcare. I dedicate my work here to her and I thank her for being such a positive part of my life as far back as I can remember. I thank her for being who she was. Even though she was the youngest and had many expectations put on her, she exceeded everyone's expectations and was one of the smartest, most thoughtful, and funniest people I have ever known and loved. Even though I showed potential when I was young, she was always ready to take a step beyond. She easily brought home better grades and class rankings than I did. She bettered my high standardized test scores. In high school, I was voted captain of my varsity swim team and she was voted captain of her varsity cross country team. She created a life full of broad and rich experiences in college and after. She traveled the world to learn, to love, and to help those less fortunate. I'm thankful to always have her example to consider when trying to be my best. I'm sorry that she is not in this world anymore and I'm sorry that she suffered what she did. It wasn't fair.

I've learned in the years since that the best way a layperson can reduce the impact of mental illness on our society is to reduce the stigma associated with it. I'm taking this small platform to do that in my own way. I feel that the stigma associated with mental illness is shrinking every day, but it still carries a lot of feelings of awkwardness and second-guessing for most in most social situations. I think that many now are aware of the free, anonymous, and always-available National Suicide Prevention Lifeline at 1-800-273-TALK (8255) and the textline (text HOME to 741741). I also think that for many who feel

down and stressed, that the lifeline can seem like a crisis measure or overkill, in a way. In my grief, I've had some experience with different mental health treatments and I know there are many things to do and think about to improve one's mental health. Eating, sleeping, and being active in a balanced and routine way has been the best thing I have been disciplined about in the past few years. I credit my late dog Pacino for forcing me into this routine when I otherwise would have slipped out of it. I imagined that I would have written much of this dissertation with him resting by my side, but his cancer precluded that. Rest in peace Pacino, you good dog! Another therapy helpful for my mental health is talk therapy. I learned about a quick way to find a therapist at the University's Counseling and Mental Health Center (which is itself a good resource). The therapist suggested to open two websites side-by-side; the PsychologyToday.com "Find a Therapist" page and my insurance provider's network page. This was a way to quickly compare between two lists to find matches which were in my network. I have student health insurance and there were many options available which accepted the insurance and charged only a $20 or less co-pay per visit. Even though this is a quick way to narrow down who to talk to that may help one's mental health, it is still a bit of a chore. Sending out a few emails to possible therapists and making a few calls can lead to a few initial meetings and I think that can be very helpful. A therapist, a social worker, a psychiatrist, and a psychologist can all be helpful, and I think they would be happy to make any referral they feel is appropriate.

I also want to use this space to show my immense thanks to my mother Chiu Chuang Chou and my father Jei Yee Chou. They have always *always* been there for me and provided more for me than anyone could reasonably ask for. I love you mom and dad! I am always held up by your belief in me most of all. Thank you, and I love you, to my partner Maria Chavez. I'm excited to continue to grow together and I'm so grateful for your love, help, and support every day.

I am forever thankful to Professor Sanjay K. Banerjee for supporting me as a member of his lab and for his advice and guidance. I've enjoyed the company of and input from many brilliant individuals because I have been fortunate to be a member of this group. Professor Banerjee has always given me the freedom to pursue any idea or experiment and provided deep insight and direction to help me along the way, I am grateful for this. Recently, I was fortunate to be present at a 30-year anniversary celebration for Professor Banerjee at UT Austin. Everyone made it clear that he has always been a generous guide and advisor and I was again full of the feeling of gratitude.

I also thank Professor Rodney S. Ruoff for advising me and welcoming me as a member of his lab at the beginning of my graduate study. I learned many lessons in that experience that continue to serve me well today. I am grateful for Professor Ruoff's insight and direction in my research.

I thank Professor Luigi Colombo, Professor Deji Akinwande, and Professor Emanuel Tutuc for their guidance and advice throughout my graduate study. Through their direction and connections with their lab members, I have been able to be a part of and contribute to many fruitful and exciting investigations. I thank Professor Paul S. Ho and Professor Emanuel Tutuc for their guidance in my research and for their courses. Learning from them was another key part of my graduate experience.

I would like to express my gratitude to Dr. Andrei Dolocan, Dr. Hugo Celio, and Dr. Richard Piner at the Texas Materials Institute. They have contributed a tremendous amount of work and expertise to my characterization work and I appreciate that they hold me to a high standard and maintain their institute at a world-class level. I also thank Dr. Rudresh Ghosh, Professor Ariel Ismach, Professor Shanshan Chen, Professor Yufeng Hao, and Dr. Carl Magnuson for their hard work and guidance in our shared research. I am particularly grateful for the help from Jae Hyun Ahn, who I have worked closely with in

recent years. Because of his help and hard work, we have been able to show results in incorporating new materials into real devices. We did it! I also thank April Pingping Zhuang, Sayema Chowdhury, Kirsten Cole, and Raul Ramos for their contributions to our shared research today and in the past. I am assured that some of them will carry the work on in the future. I am also grateful to my other lab members, especially Hema Chandra Prakash Movva, Dr. Anupam Roy, Dr. Christopher Corbet, and Dr. Sarmita Majumder who have spent hours to help me with my work. It is also important for me to thank the staff of the Microelectronics Research Center for everything they do to make the work here possible, particularly Jean Toll, James Hitzfelder, Darren Robbins, David Farnsworth, Terry Mattord, Bill Ostler, and Jesse James. I'm sorry I'm sure I have failed to adequately acknowledge many people who have made contributions to the work presented here. Thank you everyone!

Finally, I want to thank again Professor Banerjee as well as Dr. Burt Fowler, Lonnie Wilson, and Fred Wells. I'm fortunate to have the opportunity to join the GraphAudio venture and I'm very excited to see what we can build going forward.

Abstract

Two-Dimensional Materials Synthesis, Characterization, and Devices: Working with Hexagonal Boron Nitride and Graphene

Harry Chou, Ph.D.

The University of Texas at Austin, 2018

Supervisor: Sanjay K. Banerjee

Two dimensional materials have unique properties that are anisotropic in-plane and out-of-plane. They further exhibit unique properties when they are thinned down to an isolated monolayer or a few layers. These properties have the potential to greatly impact applications in energy, computing, construction, medicine, and other industries. Many researchers have published many reports working with two dimensional (2D) materials. This dissertation describes work which has contributed to the body of research around 2D materials synthesis, characterization, and device applications primarily with graphene and hexagonal boron nitride.

Graphene is a hexagonal lattice of carbon atoms which is stable in ambient down to a single monolayer. Hexagonal boron nitride is an isomorph of graphene but with boron and nitrogen atoms on the lattice instead of carbon.

Chemical vapor deposition (CVD) synthesis processes have shown to be replicable and capable for obtaining 2D materials of high quality, and experimenting with process conditions has improved the understanding about the synthesis mechanisms occurring. The objective of my 2D materials synthesis work is, broadly, to better understand the

mechanisms during growth for graphene and h-BN. The growth mechanism has multiple of forces acting on it, in competition, and many of them are detailed in chapter 2.

Growing the body of research and knowledge about 2D materials requires us to have techniques to characterize these materials accurately and precisely. It is important to develop and demonstrate new characterization techniques which are tailored for 2D materials. In chapter 3, the research done in characterizing 2D materials and interfaces between hetero-layers will be presented.

Devices which take advantage of the dimensionality and confinement within a layer of 2D material, or multiple materials, have shown high performance in a variety of applications. The range for 2D materials device applications is continually expanding and increasing in complexity. In chapter 4, research will be presented which returns to the relatively simple system of graphene to try and apply its many unique properties for a few different photovoltaic devices.

Table of Contents

List of Figures

Chapter One: Introduction

Two-dimensional (2D) materials are a class of materials which have a layered crystal structure. The atoms within the crystal are bonded covalently or ionically within a lattice plane but have weak van der Waals bonds from one plane to another. Due to the dimensionality of their structure, properties exhibit strong anisotropy comparing within-plane and layer-to-layer. The atomic bonds within a 2D crystal cause the material to have anisotropic mechanical properties, for example, within-plane the strong covalent and ionic bonds can give high tensile strength but layer-to-layer van der Waals bonds are weak and easily cleaved or exfoliated. These anisotropies are not limited to mechanical properties. This distinct dimensionality is used to distinguish 2D materials from other dimensionally constrained material forms such as 0D materials like quantum dots and nanocrystals, 1D materials like nanowires and nanotubes, and 3D bulk crystals and structures. A common and representative 2D material is graphite, which is known as graphene when thinned down to few or single atomic layers. One traditional use for graphite and other 2D materials are as solid lubricants or lubricant additives. The reduction in friction is attributed to the cleaving and sliding between layers in the solid.

The relevance of 2D materials, particularly in recent years, is high due to the anisotropic properties mentioned above. When 2D materials are thinned down to a few atomic layers or even to a single atomic layer, distinct physical phenomena can be observed due to the physical confinement from the 2D structure. The anisotropy in mechanical properties was alluded to above, and graphene well-illustrates the phenomenon also observed in other 2D materials. The intrinsic strength, σ_{int}, of graphene is 130 GPa, making it one of the strongest materials in existence.[1] However, cleaving and exfoliating between planes of graphene occurs readily. We can also use graphene to illustrate another example

of anisotropic properties in 2D materials, electronic properties. The carbon atoms in graphene are bonded by sp^2 hybridized bonds and are discussed in greater detail below in section 1.3. Each atom also has a p_z orbital out-of-plane. The two p_z orbitals per graphene unit cell disperse into two bands, bonding and anti-bonding, and give a unique dispersion relation and band structure. Charges in the graphene conduction band are extremely mobile, with electron mobility measured up to 230,000 $cm^2/V \cdot s$ at ~ 5 K and low pressure.[2] The mechanical and electronic properties of graphene are examples of the unique and attractive capabilities that 2D materials offer.

The research undertaken in this dissertation is predominantly focused on graphene and hexagonal boron nitride (h-BN) 2D materials. The research involving graphene and h-BN is organized into three focus areas; synthesis of 2D materials in chapter 2, characterization of 2D materials in chapter 3, and devices using 2D materials in chapter 4.

1.1 2D MATERIALS HISTORY

No sharp distinction has yet been drawn between materials with a layered structure and 2D materials. Historically, graphite and other layered materials were used in a variety of industrial applications, like as solid lubricants as mentioned above or as "platy" additives for structural materials like mica is. In solid state electronics, thin layers of III-V semiconductors were deposited by molecular beam epitaxy (MBE) to form high electron mobility transistors (HEMT) in the 1970s and demonstrated 2D electron gas formation. Abrupt and epitaxial interfaces between thin layers of compound semiconductors set off advances in condensed matter physics. Here, it is appropriate to make a distinction for 2D materials as those with strong anisotropy between in-plane and layer-by-layer bonding. Significant efforts are underway by researchers using 2D materials to create heterostructure devices pushing the ultimate limit of abrupt interfaces and atomically thin layers to

demonstrate ultra-low power or high frequency switching capabilities.[3] Thus, it is important to introduce the context for how 2D materials has become an influential area for research.

The generally accepted milestone which marked the beginning of the current excitement around 2D materials was the report from Geim and Novoselov having isolated and characterized a single atomic layer of graphene in 2004,[4] for which they were awarded the Nobel Prize in Physics. Importantly, that work described the process of mechanically exfoliating graphite repeatedly to obtain single atomic layers of graphene which was straightforward for others to replicate. Therefore, many researchers could quickly make new contributions and publish experimental results to expand the field.[5] Other milestones for graphene, as it became the first 2D material to receive broad research interest, were reports about other methods for obtaining single atomic layers of material. Out of work studying intercalation compounds between layers of graphite, a method for exfoliating graphite into graphene oxide sheets in liquid suspension was developed.[6–8] Other work has shown that graphene can be obtained by high temperature thermal decomposition of SiC single crystal wafers.[9] In 2009, work was published by colleagues at the University of Texas at Austin demonstrated a process for forming a single atomic layers of graphene on copper substrates by catalytic decomposition of methane gas on the substrate surface.[10] Much more on this process, often referred to as chemical vapor deposited (CVD) graphene, later in chapter 2.

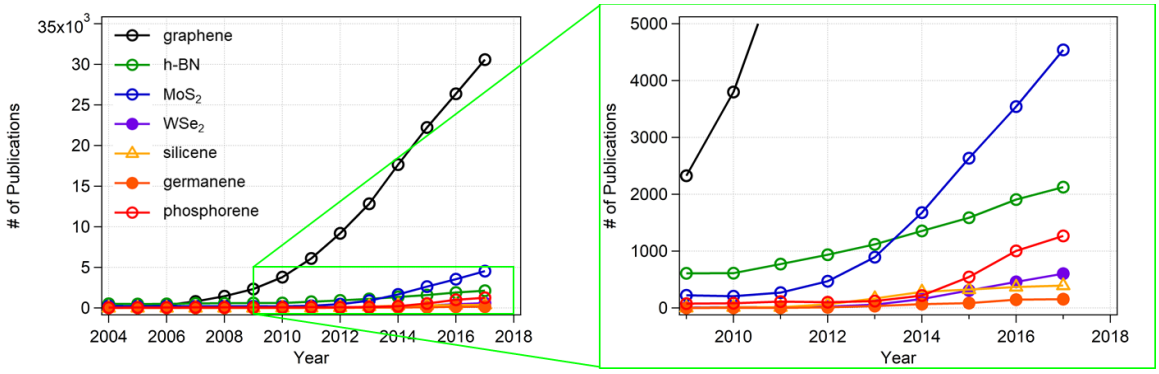

Figure 1.1: Plot of the number of publications about 2D materials over time, showing the rapid increase in research interest in the topic. Numbers taken from the Web of Science database, updated from version by Bhimanapati *et al*.[11]

Figure 1.1 shows the number of journal articles published about graphene since 2004, illustrating the rapid rise in research intensity. Other 2D materials have also experienced a sudden rise in research interest in recent years as they have shown unique properties on their own or when combined with graphene. In the early work demonstrating exceptional mechanical and electronic properties in graphene, those graphene samples were suspended to achieve the highest performance.[1,2] For an atomically thin film, it is observed that the substrate on which it sits can significantly affect its properties. Indeed, surface charges and other charge defects on the surface of SiO_2 substrates reduce the mobility of graphene significantly, despite the lack of dangling bonds or other defects in the graphene. It was shown that having an insulating 2D material substrate of h-BN resulted in a three-times increase in the mobility of charges in the graphene layer compared with an SiO_2 substrate.[12] It has since been shown that the improvement can be over an order of magnitude and is attributed to the sp^2 hybridized bonds found also in h-BN, the lack of dangling bonds, and atomic flatness.[13] A group of semiconducting 2D materials commonly known as transition-metal dichalcogenides (TMD), whereas graphene is a semimetal and h-BN is an insulator, have also experienced a sudden rise in research interest. It has been

shown that their electronic and optical properties can change when isolated into few and single layers.[11] The 2D semiconducting TMDs have fueled much research in solid state physics and electronic devices.[11] Other categories of 2D materials which have recently been studied include monoelement 2D materials like silicene and phosphorene, and MXenes based on transition-metal carbides or carbon nitrides.[11]

1.2 2D MATERIALS FORECAST

As is observed in Figure 1.1, the significant resources focused on 2D materials research have returned a significant body of knowledge about the synthesis, characterization, and applications of these materials. Of course, this is not nearly to the level of imminent and widespread technology adoption with 2D materials. There remain significant challenges for 2D materials in fundamental and applied research before they appear in new technology in a widespread way. From a synthesis perspective, CVD graphene and h-BN arguably have demonstrated processes that are scalable and have control over the layer number. However, for most other individual 2D materials, this is not the case. A more sophisticated understanding of growth mechanisms for all 2D materials is needed to truly have repeatable, scalable, and controlled synthesis processes. Also, there is a strong need for both improved handling/transfer of 2D materials as well as the robust bottom-up synthesis of heterostructures. The dimensionality of 2D materials gives them their unique properties, but also pose challenges for device integration. Consider, for example, a simple transistor made traditionally from bulk semiconductor material having impurity doping to define source and drain contacts. In this classic device, interconnects would connect through metallized volumes of material. In a single atomic layer device, we encounter dimensionality challenges. Defining and controllably doping source and drain regions, for example, is technically challenging. And contacting those regions is not

straightforward, for example the carrier mobility in graphene arises out of its bonding which does not translate to a metal pad deposited on top of a single layer nor would it for a "buried" layer in a multilayer film. Significant progress has been made toward integration and significant challenges remain. Characterization strategies will continue to advance as the 2D materials field matures to have more techniques in situ and in-line.

1.3 Graphene Properties

Graphene, as introduced in above sections, is a single atomic layer of carbon atoms arranged in a hexagonal lattice. The arrangement can be seen below in Figure 1.2. The carbon atoms in graphene, and graphite, are bonded together by sp^2 hybridized orbitals in-plane.[14] The bond length in graphene is 1.42 Å.[14] The unit cell of graphene is indicated in Figure 1.2 along with the lattice vectors a_1 and a_2. In graphite, the layer-to-layer spacing is 3.35 Å. Earlier theorists suggested that single atomic layer films were thermodynamically unstable and could not be isolated, but the strong carbon-carbon bonds in graphene allow it to be chemically and thermally stable.[5] These sp^2 bonds, also referred to as σ bonds, give graphene its incredibly high breaking strength, as mentioned above. Other excellent mechanical properties of graphene have been reported as well such as high strain > 20% before breaking and high Young's modulus of 1 TPa,[14] where structural steel has a Young's modulus ~ 200 GPa.

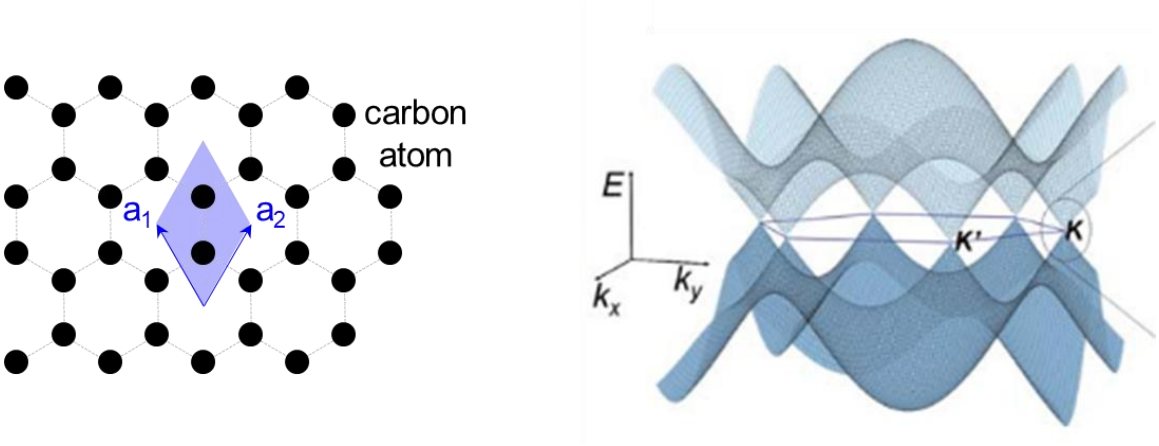

Figure 1.2: Hexagonal atomic arrangement of a single atomic layer of graphene. Lattice vectors a_1 and a_2 are labeled in blue along with the primitive unit cell. A perspective view of the bonding and anti-bonding bands of graphene in reciprocal space (reproduced from Reference 14).[14]

The exceptional electronic properties of graphene arise due to the p_z orbitals, also referred to as π orbitals, which disperse into bonding (valence) and anti-bonding (conduction) bands. These bands converge to zero gap at the *K* points of the Brillouin zone, or primitive unit cell in reciprocal space, of the graphene lattice.[14] Near the *K* points, the band edges are linear and the dispersion is approximated as $E = \hbar v_F|k|$. Here $\hbar$ is the reduced Planck's constant, k is the wave vector away from the *K* points, and v_F Fermi velocity in graphene (~ 10^6 m/s).[14] This linear dispersion means that charge carriers in graphene mimic relativistic particles with near masslessness and speed of light velocity, they are referred to as massless Dirac particles or fermions.[5,14] Single layer graphene also has exceptional thermal properties, with a thermal conductivity over 5000 W/m·K and a large and negative thermal expansion coefficient of ~ -6 x 10^{-6} K^{-1}.[14] A single layer of graphene is also optically transparent with each layer absorbing 2.3 % of incident light, independent of wavelength.[15] This optical behavior is due to the relativistic behavior of charges in graphene and incident light is absorbed due to coupling between light and

relativistic electrons dictated by the fine structure constant, $\alpha = e^2/\hbar c \sim 1/137$ where c is the speed of light.[15]

The unique bonding and band structure of graphene also makes it an ideal material for the Raman spectroscopy characterization technique. Raman spectroscopy probes a sample with coherent light, the energy of the incident radiation excites atoms in the sample to an elevated vibrational energy state. The majority of incident light is scattered elastically (Rayleigh), but a small fraction is inelastically scattered and the emitted light is shifted in energy by a quantity of a resonant vibrational mode of the sample. This resonant vibrational mode is based on the mass and bonding of the atoms in the sample and the inelastically scattered photons are shifted in energy by a Raman shift, commonly expressed in units of cm^{-1}. Raman spectroscopy is well-suited for graphene due to the zero-gap in the band structure, which makes any incident wavelength radiation resonant. The Raman spectrum of a graphene sample gives detailed information about atomic structure and electronic properties.[16] For example, the Raman spectrum of a graphene sample can give information about doping, defect density, stress and strain, and chemical functionalization.[16]

1.4 Hexagonal Boron Nitride Properties

Hexagonal boron nitride (h-BN) was referred to above as a complementary insulating material or a substrate for graphene. It is useful to consider h-BN along with graphene for several different reasons. Structurally, as its name suggests, h-BN has a hexagonal crystal structure with boron and nitrogen atoms arranged as carbon atoms are arranged in the graphene lattice. Figure 1.3 below illustrates the boron and nitrogen atom arrangement in the crystal as well as the lattice vectors for h-BN. Due to the electronegativity difference between boron and nitrogen, there is an ionic nature to the sp^2 bonds in h-BN, compared to graphene.[17] The B-N bond length is 1.44 Å, compared with

1.42 Å for the C-C bond in graphene.[17] There is a ~ 1.7 % lattice mismatch between h-BN and graphene.[17] While the layer-to-layer spacing for h-BN is similar to graphene, 3.33 Å for h-BN compared with 3.35 Å for graphene, the stacking between layers is distinct. In graphene and graphite, AB stacking is predominant with a carbon atom above the center of the hexagon below. In h-BN, AA' stacking is predominant with boron and nitrogen atoms directly above each other in succession.[17] The mechanical properties of a single atomic layer of h-BN were recently reported with a fracture strength of ~ 70 GPa and Young's modulus of ~ 0.87 TPa, making it one of the strongest insulating materials in existance.[18] Also like graphene, h-BN is stable in ambient conditions down to a single atomic layer due again to highly stable bonds.

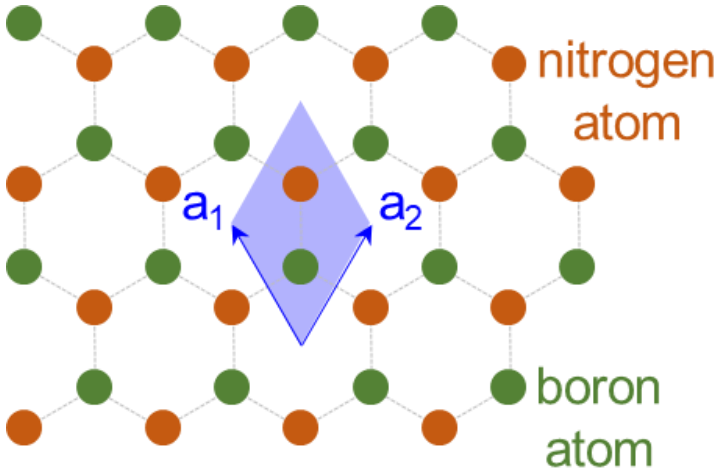

Figure 1.3: Hexagonal atomic arrangement of a single atomic layer of h-BN. Lattice vectors a_1 and a_2 are labeled in blue along with the primitive unit cell.

H-BN is an insulator with a wide bandgap of ~ 5.97 eV with the ionic nature of the B-N sp^2 bond, meaning the p_z orbital is localized.[17] The wide bandgap has consequence for its optical properties and h-BN gives light emission in the UV and deep UV range.[17,19] Thin

films of h-BN have been used as atomically flat and inert substrates for 2D materials devices and also as dielectric layers, with a dielectric constant of $\varepsilon \sim 4$.[17,20] Few-layer h-BN also demonstrates high thermal conductivity, reported at 360 W/m·K.[13] These different mechanical, electronic, optical, and thermal properties have driven the research interest in h-BN and h-BN combined with other 2D materials.

1.5 Chapter Organization

The chapters following this one are separated by research in three different focus areas for 2D materials. Chapter 2 will describe research done in 2D materials synthesis. A number of different synthesis processes for graphene and h-BN have been studied, and the focus will be on how those studies contribute to the understanding of the growth mechanisms. Chapter 3 will describe research done in 2D materials characterization. Due to their layered structure and atomically thin nature, 2D materials pose unique characterization challenges. Research utilizing a combination of analysis techniques will be described, with an emphasis on using ion mass spectroscopy to study 2D material vertical heterostructures and their interfaces. Lastly, Chapter 4 will describe research done in 2D materials device applications. Graphene and h-BN thin films were integrated in flexible solar cells. A conclusion chapter and an appendix has also been included, the latter documents the operation and maintenance of a graphene synthesis system.

Chapter Two: 2D Materials Synthesis

Isolating single atomic layers of graphene by researchers at The University of Manchester was the work that kicked off the rush of research interest into 2D materials,[21] and the researchers were awarded the Nobel Prize. Over one hundred layered materials have been identified that can be isolated into single atomic layers and among them exhibit metallic, semi-metallic, semiconducting, or insulating behavior.[22] To take advantage of these individual properties, and to demonstrate other exciting phenomena by combining multiple different 2D materials, it is necessary to be able to synthesize these different materials in a way that is controllable and gives consistent results. Thus another work which accelerated research interest into 2D materials was using a chemical vapor deposition (CVD) process reported by researchers here at the University of Texas at Austin to synthesize graphene on copper substrates.[10] Since that time the synthesis process has been studied to understand the growth mechanism and also processes to synthesize other 2D materials have also been reported.[11,23] In this chapter, research that was undertaken to further the understanding of graphene and h-BN synthesis will be described. An understanding of growth mechanisms is conditional for achieving controllable and consistent materials synthesis.

2.1 Synthesis Introduction

The 2009 report describing a graphene CVD process has proved repeatable and reliable for obtaining high quality graphene over large areas,[10] the electronic quality has recently been shown to be comparable to exfoliated graphene[24] and area coverage at the

---

Work described in this chapter is also published in References 41 and 44 where my contribution was in sample characterization, and also in References 54 and 56 where my contribution was in design of experiment, sample preparation and characterization. Appropriate citations appear in the text and figures as well.

commercial scale has been reported.[25] CVD processes have also been developed for other 2D materials as well. For h-BN, popular methods also synthesize using catalytic metal substrates like copper, nickel, platinum, sapphire, and others.[26–30] In the case of TMDs like MoS_2, CVD processes using solid precursors vaporized and reacting at high temperature on arbitrary substrates are popular.[31–33] Thus, CVD has shown to be a replicable process to obtain 2D materials of high quality and experimenting with process conditions has improved the understanding about the synthesis mechanisms occurring. Other synthesis techniques have also been reported, which have advantages and disadvantages. For example, reduced graphene oxide flakes suspended in fluid can be obtained from graphite powder.[34,35] This material is limited as a suspension in fluid or in a powder form, rather than as a continuous sheet. Other work has been done in ultra-high vacuum (UHV) systems to deposit on single crystal substrates, utilizing molecular beam epitaxy (MBE) systems.[36] However, these systems are not compatible with high volume processes, though tight control over parameters has allowed significant findings for growth mechanisms. For graphene, a segment of researchers have pursued deriving the material by sublimating Si out of SiC single crystals at high temperatures.[9,37] However, SiC single crystal substrates are relatively expensive and handling in high temperature and ultra high vacuum processes can be challenging. In this work, CVD processes are studied as they permit process condition control and also are scalable for synthesizing large areas of 2D materials.

2.2 Graphene Synthesis

In opening this chapter multiple 2D materials synthesis methods, including those specifically for graphene synthesis, are mentioned and the CVD process is among them. The availability of graphene, at an earlier date than for other 2D materials, was a key factor

in how rapidly research interest grew. Here, research toward understanding the synthesis mechanism of graphene using CVD processes will be discussed.

2.2.1 Graphene Growth Mechanism

The mechanism for graphene CVD synthesis is understood to proceed by steps; (1) carbon-containing gas precursor decomposes on the catalytic metal surface at high temperature, (2) carbon radicals either are mobile on the surface (in the case of copper substrate) or fully decompose and dissolve into the bulk (in the case of nickel substrate), (3) the carbon radicals nucleate and grow graphene crystal domains (in the case of Cu substrate) or precipitate out of the bulk upon cooling (in the case of Ni substrate.[38] Indeed, kinetic and thermodynamic forces alter the synthesis result if conditions such as temperature and pressure are adjusted.[39] Other important factors in graphene growth include the carbon-containing precursor chemistry and form (such as solid or gas), the delivery of the precursor to the substrate, the substrate chemistry and morphology (such as roughness or impurity content), and applying energy to drive the growth (such as through chamber heating or substrate heating or remote sources like plasma).[40]

A benchmark graphene CVD process was reported in 2009 using methane precursor to grow on Cu foil substrate.[10] Methane is a readily available carbon-containing precursor showing efficient thermal catalytic decomposition on metal surfaces.[40] In addition to its catalytic activity to decompose precursor, Cu has a low carbon solubility even at high temperature. Thus graphene crystal domains nucleate and grow on the Cu surface and additional layers are prevented from forming once the Cu surface is fully covered. The general low pressure CVD (LPCVD) process approach begins with loading the Cu substrate into a quartz tube in a furnace and pumping down to base pressure, typically a few millitorr, as seen in Figure 2.1. The process is initiated with heating the furnace while

flowing hydrogen gas (10 sccm controlled with a mass flow controller, MFC) to maintain a reducing atmosphere such that the Cu substrate will not oxidize. The furnace temperature is ramped to the growth temperature, typically in the range of 900 – 1100°C, while the hydrogen continues to flow. This reduces any existing native oxide and can also serve to remove some surface contaminants, and an anneal time of a few minutes (10 – 60 minutes) is included. After the anneal, the methane precursor is introduced (also 10 sccm controlled with a MFC) for a short growth time of 1 – 30 minutes. After the precursor exposure time, the furnace power is cut and the system is allowed to cool. Typically the hydrogen and methane flows are shut and the substrate is cooled under argon, though it can also be cooled under only hydrogen or hydrogen and methane. After cooling to room temperature, the vacuum is broken (the valve leading to the pump is shut) and the sample can be retrieved and taken for further processing.

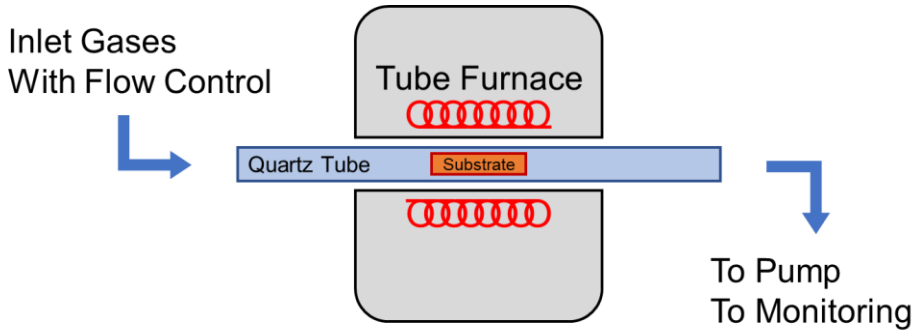

Figure 2.1: Schematic of graphene CVD synthesis system. Inlet gases, commonly hydrogen and methane, are controlled with mass flow controllers. Pump is commonly an oil roughing pump giving a base pressure of a few millitorr. Monitoring may include pressure gauge and/or residual gas analyzer (RGA).

2.2.2 Oxygen Effect on Growth

In addition to well-understood process parameters such as temperature and pressure during synthesis,[39] other factors can have an important impact on the formation of

graphene. To that end, the role of oxygen in the process was investigated,[41] because its partial pressure can be difficult to control even in vacuum systems. It was observed that oxygen serves a dual role in graphene CVD on copper; it both suppressed nucleation of graphene domains and boosted the growth rate through a lower energy pathway to attach additional carbon at the domain edge. In order to draw conclusions about the role of oxygen, it was necessary to directly measure the oxygen content in the copper substrate. For a project led by Dr. Yufeng Hao, I determined the oxygen content for the copper substrates such that the impact of the oxygen on graphene growth could be understood.

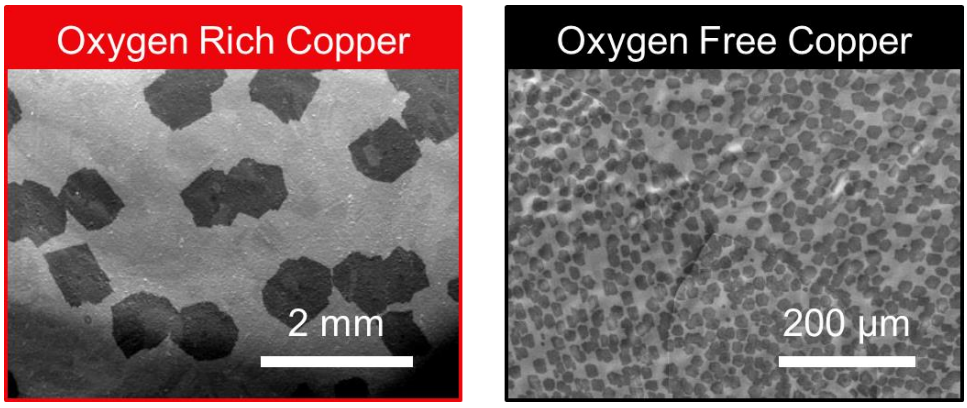

Figure 2.2: Scanning electron microscopy (SEM) images of graphene grown on copper with different oxygen content. The dark contrast indicates domains of graphene, domain size and density are distinct between the two different Cu substrates.[41] From Reference 41. Reprinted with permission from AAAS.

It is known that oxygen impurity levels in different Cu substrates vary depending on the vendor source. The objective of the study was to determine the effect of oxygen dissolved in the substrate, on the synthesis of graphene. Two different Cu foils, one with a relatively high concentration of oxygen impurity (oxygen rich, OR) and one with a low concentration of oxygen impurity (oxygen free, OF), were analyzed by secondary ion mass spectroscopy (SIMS).[41] The resulting graphene growth for the OR Cu and OF Cu can be

seen in the scanning electron microscope (SEM) images in Figure 2.2. To isolate the oxygen affect, a third sample was prepared with O_2 flowed to the OF Cu at high temperature (partial pressure P_{O2} = 1 mTorr, 1000 °C). Due to the low overall concentration of oxygen in Cu, the measurement needed to be highly sensitive and so the three samples were analyzed using secondary ion mass spectroscopy (SIMS). By capturing the secondary ions (SI) related to oxygen (O^-) and copper (Cu^-), depth profiles of the oxygen content in the different copper substrates were plotted.[41] SIMS analysis of a known concentration reference sample allows for the quantification of specific impurities, here oxygen in Cu. Further discussion about SIMS analysis can be found in Chapter Three section 3.2 and 3.3. This verified that the oxygen content in OR Cu was several orders of magnitude higher than for the OF Cu. It was also observed that oxygen gas exposure of the OF sample indeed increased the oxygen concentration at the Cu surface. As graphene growth occurs at the surface in the case of CVD on Cu, this analysis provided a basis to draw conclusions about the role of oxygen in graphene CVD synthesis.[41]

Figure 2.2 shows a distinct difference in the growth of graphene domains on OR Cu compared with OF Cu, for the same growth conditions. The domain size is significantly larger for OR Cu and the domain nucleation density is higher for OF Cu. The oxygen content for the substrate was measured by SIMS as described above. Figure 2.3 shows the depth profile of the oxygen concentration as a function of depth into the Cu bulk. Comparing between black (OF Cu) and red (OR Cu) traces, there exists a difference in oxygen concentration of > 2 orders of magnitude at the surface and > 4 orders of magnitude in the bulk. The result of the control experiment of exposing the OF Cu to oxygen gas during growth is also shown in Figure 2.3. Whereas OF Cu showed small domains and high nucleation density, OF Cu with oxygen gas exposure showed large graphene domain formation and low nucleation density, as was observed for OR Cu. These experimental

results are marked with blue. In the oxygen concentration depth profile in Figure 2.3, the blue trace shows slightly higher oxygen concentration at the surface as well as the bulk compared with OF Cu. Thus, the introduction of oxygen to a Cu substrate with low oxygen content altered the domain size grown and the nucleation density of graphene. To confirm the role of oxygen, isotopically pure oxygen, $^{18}O_2$, was used for the control experiment. The mass spectra obtained could easily distinguish between natural isotope abundance O_2 and $^{18}O_2$. The Cu foil surface after $^{18}O_2$ exposure showed again a large increase in oxygen content and was thus isolated from other sources of oxygen (such as from residual gas in the LPCVD chamber). Additional analysis was done with this graphene was to determine its quality. For instance, large single crystals of graphene are of interest for electronic applications and samples were probed by Dr. Babak Fallahazad. The carrier mobility measured ranged from 15,000 to 30,000 $cm^2V^{-1}s^{-1}$ at room temperature. Density functional theory (DFT) calculations, done by colleagues at A*STAR, Singapore, showed that oxygen reduces the edge attachment energy barrier for carbon to the graphene domain, thus giving a more rapid growth rate and larger graphene domains. It was also found that oxygen occupied possible nucleation sites and suppressed graphene nucleation.[41]

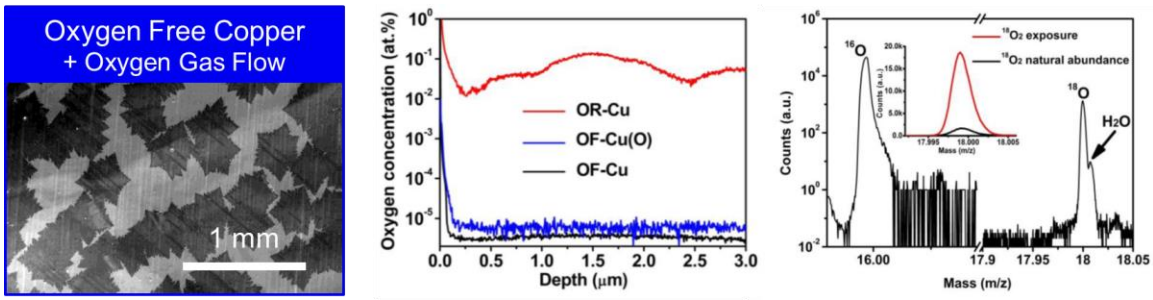

Figure 2.3: SEM images of graphene grown on oxygen-free copper with oxygen gas flow during growth. Depth profiles showing oxygen content with respect to depth into copper substrate. Mass spectra portion showing that oxygen

exposure (^{18}O isotopically enriched) increases surface oxygen content.[41] From Reference 41. Reprinted with permission from AAAS.

2.2.3 Adlayer Formation

Figure 2.4: Photographs showing a few steps for forming a copper enclosure substrate. Images were taken by Dr. Yufeng Hao (permission granted by Springer Nature).[42]

The basic LPCVD graphene growth process described above in section 2.2.1 was altered by using folded Cu foil enclosures, which restricted the flow of precursor gases to the interior surface.[43] It is observed that the graphene growth rate, and nucleation density is significantly lower for the interior surface of the Cu enclosure than for the exterior surface of the Cu enclosure. Figure 2.4 shows photographs of the folding process for forming a Cu enclosure. The Cu enclosure has been used to study various details related to the growth mechanism of graphene. It was used for understanding the formation of graphene adlayers in LPCVD on the interior surface of Cu enclosures.[44] Understanding the appearance/growth of adlayers during graphene CVD synthesis is important for developing process conditions for fully uniform films.[45,46] In this work, led by Dr. Shanshan Chen, it was the aim to show the stacking order of graphene adlayers and I provided the analysis and needed evidence. To show the stacking order of graphene adlayers, multilayer graphene domains were grown using isotopically pure methane precursors ($^{12}CH_4$ and $^{13}CH_4$). By alternately flowing the $^{12}CH_4$ and $^{13}CH_4$ during growth, graphene domains were

formed with alternating bands of ^{12}C and ^{13}C. In adlayer regions, it was observed that a given layer had a different layering pattern of ^{12}C and ^{13}C. To show layer order (with adlayers forming at the interface), SIMS depth profiling and mapping analysis was performed. The technique allows for imaging of secondary ions (SI) in real space and a low and uniform sputtering rate was used to remove the graphene layer-by-layer. Again, a detailed discussion about SIMS analysis can be found in Chapter Three section 3.2 and 3.3.

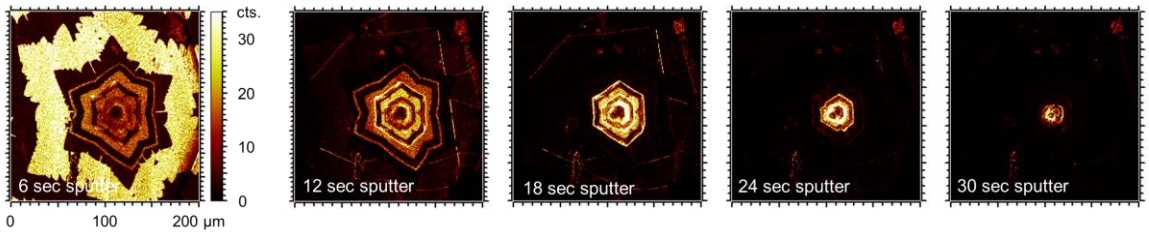

Figure 2.5: SIMS secondary ion maps of C_2^- SI showing progressive removal of multilayer graphene layer-by-layer.[44] Reprinted with permission from Reference 44. Copyright 2013 American Chemical Society.

Figure 2.5 shows the SI maps of ^{12}C for the depth profiling; at the beginning of sputtering (from left to right), the top layer of graphene is visible also showing the highest lateral growth rate. The growth rate is determined by the width of the isotopically pure band, recall that the isotopically pure methane was sequentially flowed with a constant time period (12 minutes each). Thus, the wider isotopically pure bands for the top layer show a higher lateral growth rate. After more sputtering, the adlayers are successively exposed with each adlayer showing a lower growth rate (narrower bands). Based on the analysis conditions, sputtering for 6 seconds removed roughly a single graphene layer. The SI maps are also collected and formed into side-on maps (X-Z and Y-Z direction cross-sections) shown in Figure 2.6. The adlayer structure could be clearly identified beneath the topmost (outer) graphene layer. This observation of the structure of the multilayer graphene proved

that the adlayers are growing at the interface between graphene and Cu, as depicted in Figure 2.7. In this nanoscale space, the partial pressure of carbon precursor is suppressed which in turn suppresses the lateral growth rate.

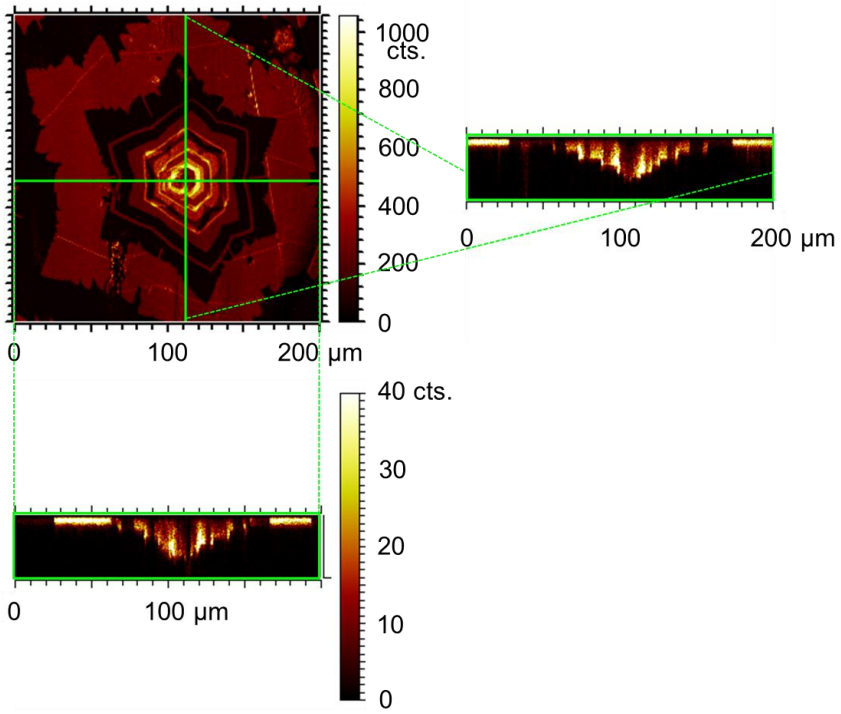

Figure 2.6: SIMS secondary ion map of C_2^- from multilayer graphene domain. X-Y and X-Z cross-section of the secondary ions are also shown to illustrate the adlayer structure.[44] Reprinted with permission from Reference 44. Copyright 2013 American Chemical Society.

The adlayer stacking order, with the adlayer forming at the graphene-Cu interface, was verified with another control experiment performed by Dr. Shanshan Chen. A bilayer graphene domain was transferred after isotope-labelled growth and then mapped by Raman. The Raman spectra shows distinct ^{12}C and ^{13}C graphene vibrational modes due to the difference in mass between the isotopes. Additionally, because of the high quality of the bilayer domain grown and the transfer, no defect D-band was detected by Raman. Then,

the sample was exposed to oxygen plasma for 5 seconds to damage the outer layer. On repeat Raman mapping, a defect D-band was clearly visible only for the thick ^{12}C band in the graphene domain, while the ^{13}C band remain defect D-band free. This result confirmed that the outer layer was the wide-band layer with higher growth rate. Other work studying the formation of graphene adlayers have also shown that they form at the interface between graphene and Cu.[47] Dr. Yufeng Hao, continuing his work studying the impact of oxygen on graphene growth, also found adlayer formation between the graphene and the substrate.[42]

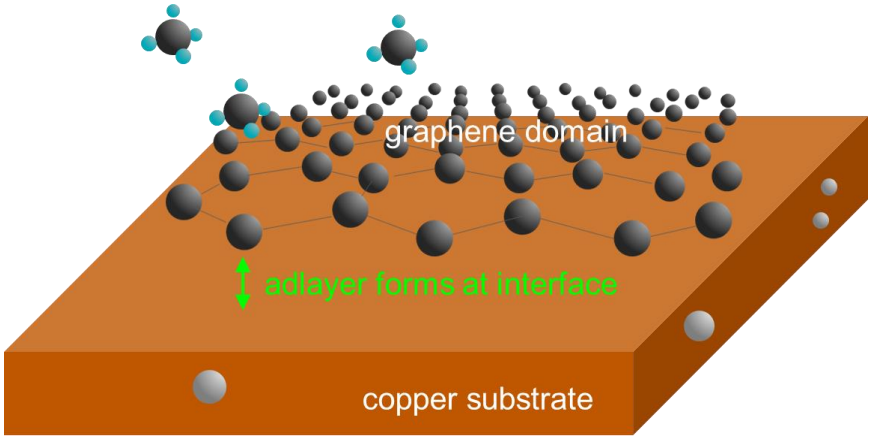

Figure 2.7: Schematic of graphene adlayer formation, which forms at the interface between the graphene and the copper, in this case, substrate.

2.2.4 Multilayer Formation and Growth on CuNi Alloy and Ni

Thus far, the graphene growth discussion has been centered around a LPCVD process growing on a Cu substrate, as described in Reference 10. Other growth processes were referenced briefly in section 2.2.1 which are described at length in Reference 39. Those experiments showed the difference in graphene growth on Cu substrates and Ni substrates; a single atomic layer is grown on Cu and multilayer is grown on Ni, owing to

the relatively high carbon solubility in Ni. Cu and Ni are fully miscible as an alloy and that gives the opportunity to explore more aspects of growth. Two articles were published exploring graphene growth on 70-30[48] and 90-10 Cu-Ni[49] alloy (the first number indicating Cu content, i.e. 70-30 is 70 % Cu and 30 % Ni alloy) substrates, which are both commercially available. I contributed heavily to the analysis in Reference 49, though both works address the issues of solubility and diffusion that are key to understanding the graphene growth mechanism. By controlling the solubility, through the Ni content, the amount of carbon was controlled and thus also the thickness of multilayer graphene grown was also controlled. Figure 2.8 shows graphene grown on Cu, 90-10 Cu-Ni, and 70-30 Cu-Ni substrates at 1050°C, after transfer to a glass slide. Each single atomic layer of graphene absorbs ~2.3% of incident light and so the thickest film (grown on 70-30 Cu-Ni substrate) appears darkest. This ability to tune solubility and consider diffusion has consequences for understanding other growth in section 2.3.6 and also for devices in section 4.2.

Figure 2.8: Photograph of graphene grown on pure copper (left), 90-10 Cu-Ni alloy (center), and 70-30 Cu-Ni alloy (right). Each layer of graphene absorbs ~ 2.3% of incident light and the darker films represent thicker multilayer graphene grown on substrates with increasing Ni content, which has high carbon solubility.

2.3 Hexagonal Boron Nitride Synthesis

Hexagonal boron nitride has been synthesized just like it has for graphene. Exfoliation is possible, also deposition is possible. CVD, sputtering, Plasma-Enhanced and Radio-Frequency deposition processes have been used to grow h-BN.[13,50,51] A common method is CVD on catalytic metal substrates as it has been with graphene on copper and nickel. The next sections will focus just on CVD processes for h-BN growth on metals.

2.3.1 Hexagonal Boron Nitride Growth Mechanism

Synthesis of high quality h-BN has been achieved and reproduced by several research groups using chemical vapor deposition (CVD) processes.[51–53] Though progress has been made to understand the growth mechanism, the understanding is incomplete and more must be learned to have a reliable process that can repeatably produce high quality h-BN.[13,54–58] To date, the limited understanding about the growth mechanism has meant that integrating h-BN with other 2D materials for various device applications has been limited.[23,59,60] Therefore a deeper understanding is needed to overcome the barrier and integrate h-BN into device applications.

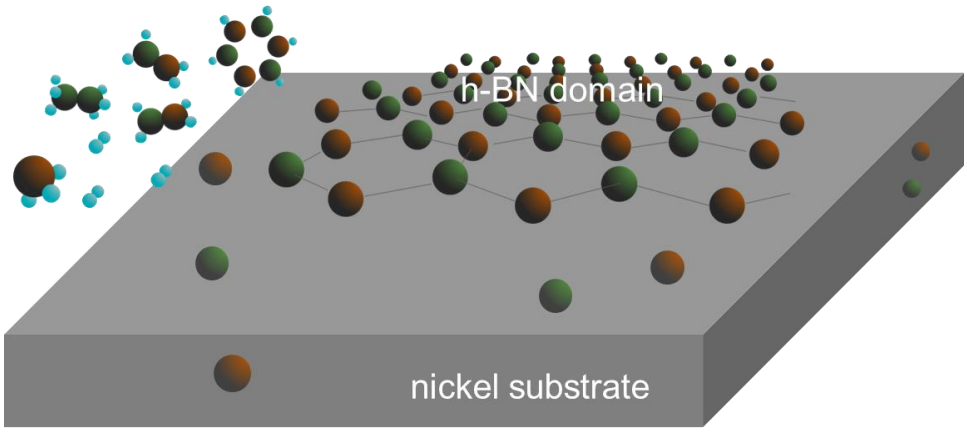

Figure 2.9: Schematic of h-BN synthesis.

In general, growth of h-BN in CVD occurs by B- and N- containing precursors decomposing on the catalyst surface, dehydrogenation continues at the surface and diffusing B and N form into h-BN layers, as depicted in Figure 2.9.[13] While growth of h-BN has been performed on many substrates, metallic/catalytic,[13,51,61] dielectric surfaces,[30,62] and even graphene,[63–65] more experiments are needed to achieve a better understanding of the growth mechanisms on different substrates.

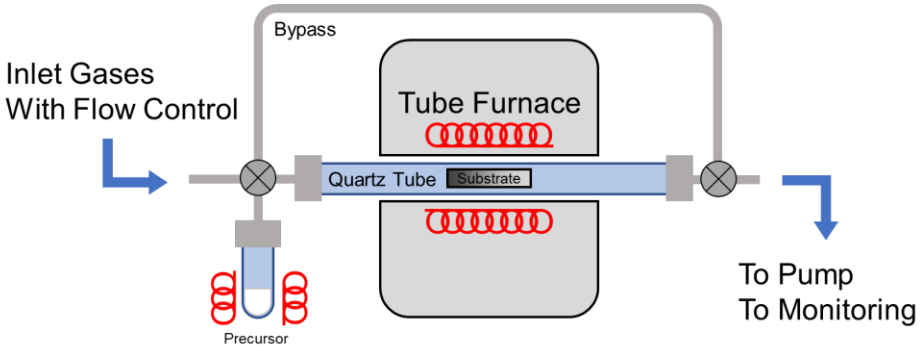

Figure 2.10: Schematic of h-BN CVD tube furnace synthesis system with a solid ammonia borane precursor vessel which is remotely heated and a bypass line for pressure release.

The h-BN growth experiments have been carried out using two systems. One is a modification of the tube furnace as used for graphene growth described above in section 2.2. An added precursor vessel with heating is used for solid precursors and a bypass line is incorporated for pressure release while heating the solid precursor, as shown in Figure 2.10. The other system is a steel vacuum chamber with a quartz window on the top. A high power lamp is positioned above the quartz window and used to heat the substrate, a schematic is shown in Figure 2.11.

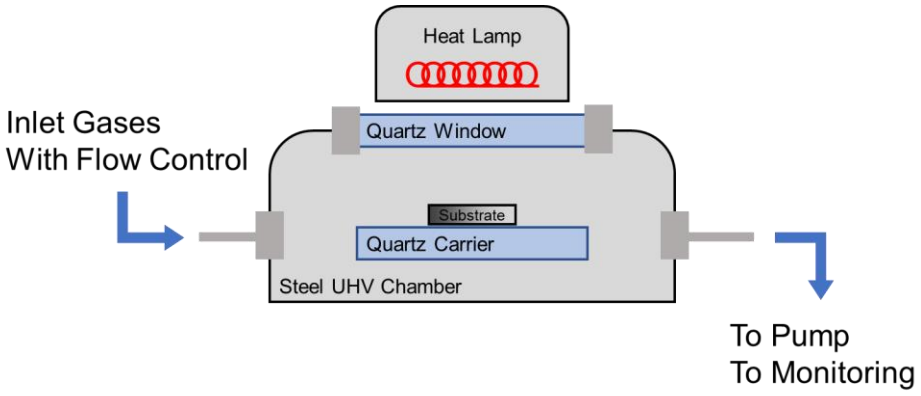

Figure 2.11: Lamp heated h-BN growth system which has gaseous diborane and ammonia precursors.

2.3.1.1 Precursors

Several different B- and N- containing compounds have been used to grow h-BN and Reference 13 contains a table summarizing many of these precursors. Explain that there have been many reports using different precursors. Among the most popular are ammonia borane and borazine, which are shown in Figure 2.12. These precursors have the advantage of having the 1:1 stoichiometry of the h-BN, however handling a solid precursor (ammonia borane) or a liquid precursor (borazine) is challenging for the control of flow rate or long term storage, for example. Upon heating, ammonia borane decomposes into various polyaminoboranes, one of which is borazine.[66,67] Another set of precursors also used for h-BN growth is diborane and ammonia gases, which are also represented in Figure 2.12. These precursors are more readily controlled when flowed into the growth chamber, but because the boron and nitrogen are separated the ratio of the precursors must be monitored to ensure h-BN growth. Also, diborane and ammonia both pose health and safety hazards, so it is important to take appropriate precautions related to monitoring and handling. In the experiments described here, either diborane and ammonia or ammonia

borane precursors will be used. Other precursors, such as BCl_3 and N_2 have also been reported by others.[13]

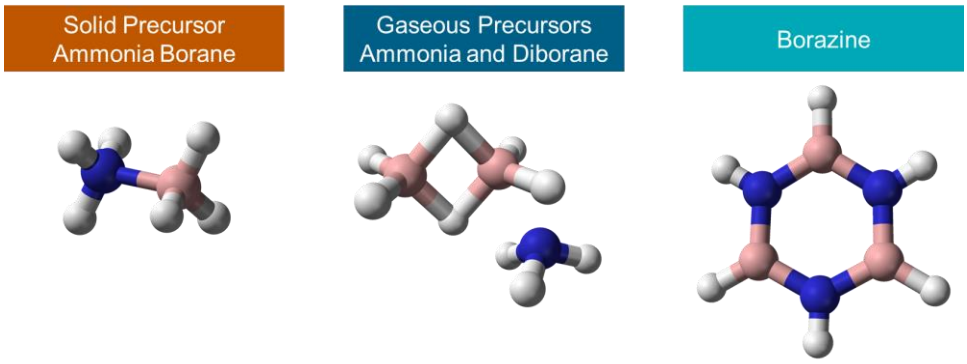

Figure 2.12: Ball and stick model of precursor molecules used in h-BN CVD synthesis.

In experiments using the ammonia borane precursor, the system shown in Figure 2.10 was used, where the solid ammonia borane powder (NH_3BH_3), which was heated separately above its decomposition temperature, and was carried to the CVD furnace by hydrogen gas. Diborane and ammonia precursor growths were performed in both types of growth system.

2.3.1.2 Substrates

Many different substrates have also been used for h-BN growth, and a table summarizing the different types can also be found in Reference 13. As is the case of graphene growth, catalytic metal substrates, such as Fe, Co, Ni, and Cu, are popular for h-BN growth. However, as was referenced in section 2.3.1, some dielectric substrates and 2D material substrates have also been used to grow h-BN.[13] The experiments here are investigating the growth of h-BN using Ni substrates. There will be parallels to graphene found in the growth mechanism relating to diffusion and solubility. The use of foil

enclosures, as discussed in section 2.2.3, will also be revisited to again show the growth mechanism, in this case for h-BN.

2.3.2 Growth of h-BN Films with Controlled Thickness

In experimental work led by Dr. Ariel Ismach, a process for growing thin films of h-BN using diborane and ammonia (B_2H_6 and NH_3) precursors was developed.[54] The basic process begins similarly to the graphene growth process, by loading a substrate (in this case Ni foil) into the center of a quartz tube in a tube furnace and pumping down to base pressure, in the system type of Figure 2.10. Next, hydrogen is flowed (10 sccm) through the tube and the furnace is heated, the reducing environment prevents the Ni from oxidizing. The furnace temperature is ramped to the anneal and growth temperature (1025°C) and hydrogen flow continues, this anneal step (10 to 60 minutes) removes surface oxide as well as some contaminants from the Ni. The diborane and ammonia precursors are flowed, at 1 sccm and 18 sccm respectively, to the substrate controlled by MFC and the hydrogen flow remains at 10 sccm. The growth step lasts for 1 to 30 minutes and then the furnace heating is shut, along with the diborane and ammonia gas flows. The system is allowed to cool back to room temperature, during which time the hydrogen flow is shut and argon is flowed at 20 sccm, and then the sample can be retrieved after breaking vacuum. The basic process flow is illustrated in Figure 2.13.

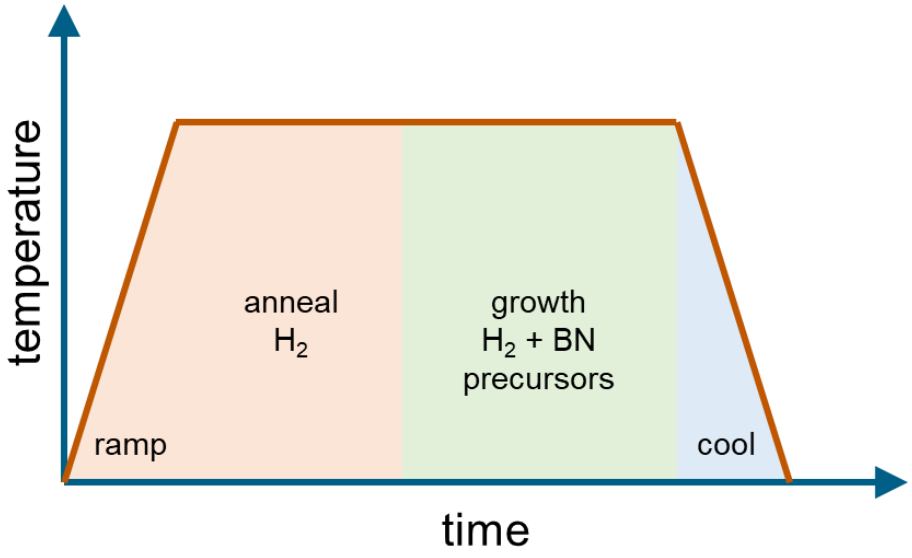

Figure 2.13: Basic growth process steps for h-BN.

For these growth experiments, the total pressure was typically 135 mTorr (1:18 diborane:ammonia flow ratio) for exposure of these gases at 1025 °C. The Ni foil was also treated prior to loading by sonicating in acetone and then rinsing with IPA to remove any grease or organic contaminants from the surface.

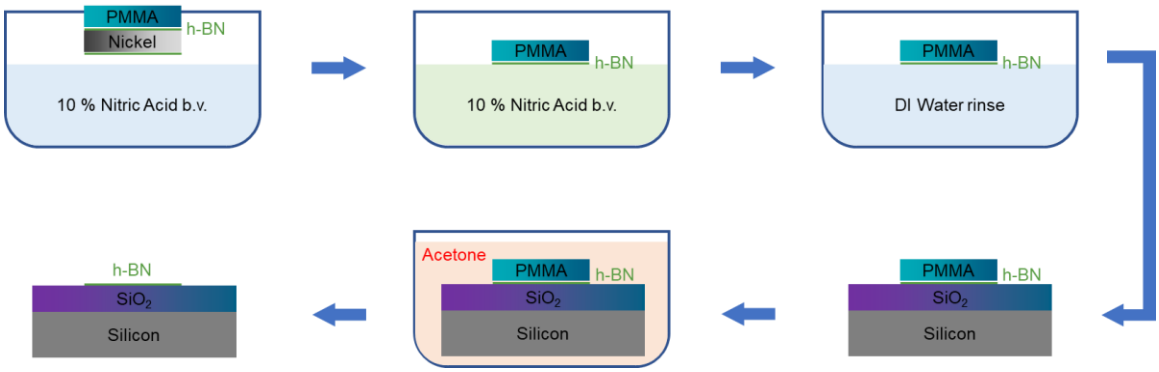

Figure 2.14: h-BN transfer schematic.

It was frequently necessary to transfer the h-BN from the growth substrate for additional characterization or other processing. The process was adapted from a common wet etching process used for graphene transfer.[10,68] Figure 2.14 illustrates the basic steps for transferring h-BN from the Ni growth substrate to an arbitrary target substrate (shown is a SiO_2/Si wafer). The h-BN, while still on the Ni growth substrate, was coated with poly(methyl methacrylate) (MicroChem A9 PMMA) at 3 krpm for 60 seconds. The PMMA/h-BN/Ni was then baked at 90° C for 60 sec. The PMMA/h-BN/Ni was then floated on a dilute nitric acid (HNO_3) solution (10 % by volume in water) (in the case of graphene-grown-on-Cu, the preferred etchant used was 0.1M – 0.5M ammonia persulfate in water). After the metal has been fully etched, the sample is floated on DI water (which is changed two more times) to rinse away any residue or etchant. Then the PMMA/h-BN is lifted from the liquid with the desired target substrate. I have found that for the best results, prior to removing the PMMA, it is preferred to re-spin the PMMA, as has been shown by others.[69] The PMMA removal process begins after the h-BN interface with the target substrate is dry, typically the sample is left in a vacuum box overnight. The PMMA/h-BN sample is placed on a hotplate at 90° C for 60 seconds to soften and then moved onto a spin coater. The PMMA is re-spun again at 3 krpm for 60 s and then baked at 90° C for 60 seconds one last time. The PMMA layer is then removed with acetone after the re-spin, and for best results we have a modified acetone process. The first part of the process involves filling a beaker partly with acetone on a hotplate at 75° C and placing a glass stand above the surface of the acetone (normally an inverted beaker that is smaller and fits fully inside the beaker with acetone). The PMMA/h-BN sample is placed on the glass stand and then the beaker is sealed (normally with a glass cover and using parafilm around the perimeter to prevent evaporation). At elevated temperature, the partial pressure of acetone vapor is also elevated and softens the PMMA. After one hour, the second part

of the PMMA removal process begins. A new beaker with acetone is prepared and placed on a hotplate at 65 C. The PMMA/h-BN from part one is put into the warm acetone to fully remove the softened PMMA, typically the sample is left in acetone for four hours. A final vacuum anneal step may also be performed to fully remove residue from the transferred film surface.[70]

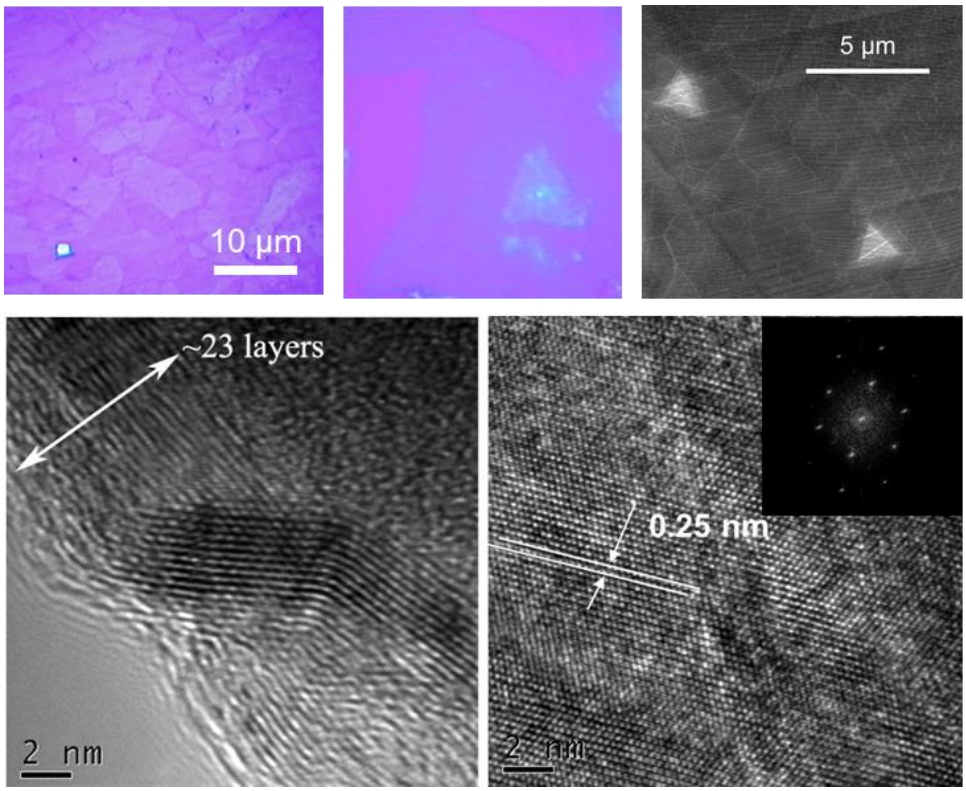

Figure 2.15: h-BN optical microscope images of transferred film. SEM image of h-BN on Ni substrate. Transmission electron microscope (TEM) image of layer-to-layer h-BN and SAED.[54] Adapted with permission from Reference 54. Copyright 2012 American Chemical Society.

The h-BN was characterized both as-grown on the Ni substrate and after transfer to other substrates to show that it was high quality. In Figure 2.15, optical microscope images show the h-BN film after transfer to a SiO_2/Si wafer substrate. The contrast differences,

between lighter and darker purple indicate h-BN of different thickness forming on different Ni grains of the polycrystalline Ni foil substrate. We also see a high magnification SEM image of the h-BN still on the Ni substrate, the lighter contrast triangular regions are adlayers of h-BN, there is h-BN covering the whole Ni substrate. More subtle contrast differences indicate Ni grain boundaries or h-BN film grain boundaries or wrinkles. Transmission electron microscope (TEM) images were captured of the h-BN film after transfer to a TEM sample grid. At the edge of the transferred film, folded edges were observed and the layered structure of the film could be seen, where the layer-to-layer spacing could be measured. The plan-view taken from the interior of the transferred h-BN film region showed spacing within the h-BN layer and also provided a clear hexagonal selected area electron diffraction (SAED) pattern.

Figure 2.16 shows more characterization results from the h-BN film. The Raman spectra show clearly the E_{2g} peak for h-BN. Raman maps show the h-BN E_{2g} peak intensity, position, and full width at half maximum (FWHM). UV-Vis spectrum allows us to calculate the optical band gap of 5.75 eV, in the deep UV, which closely matches the expected value for h-BN. X-ray photoelectron spectroscopy analysis (XPS) was also done for the h-BN film on the Ni substrate. XPS gives the binding energy of core level electrons in a material, whose energy depends on the atom as well as the what bonds are formed by that atom. B 1s and N 1s core electron energy levels are clearly detected for the h-BN film samples, with peak positions that are expected for h-BN bonding.

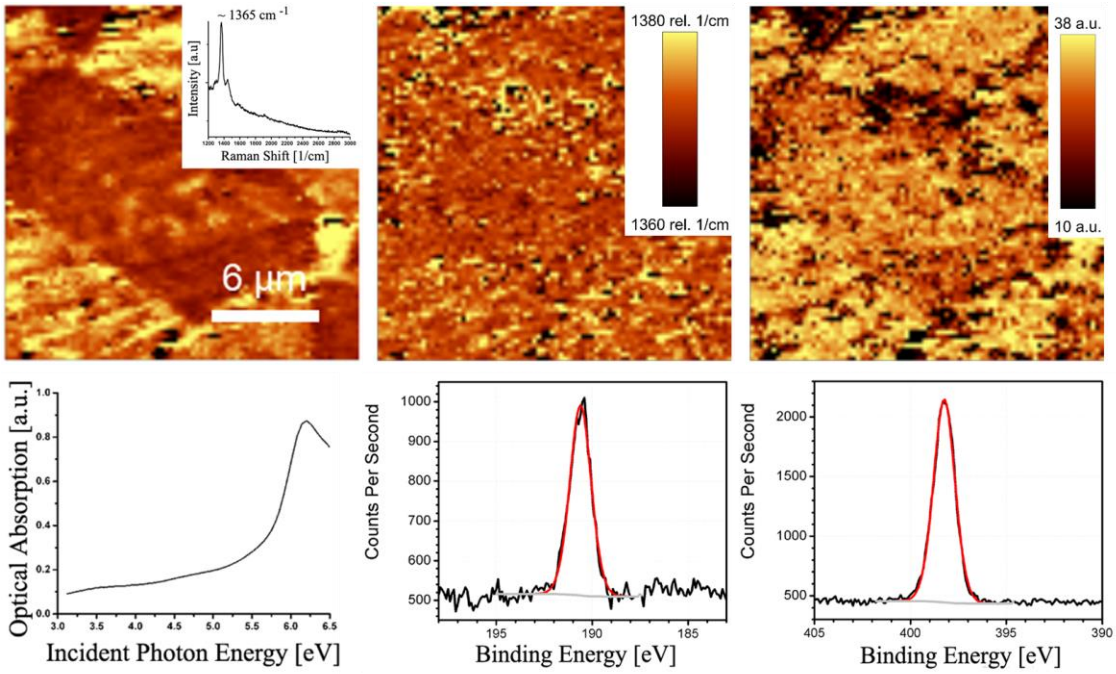

Figure 2.16: Raman mapping data of h-BN transferred film. UV-Vis of h-BN and XPS of h-BN still on Ni substrate.[54] Adapted with permission from Reference 54. Copyright 2012 American Chemical Society.

Figure 2.17 shows TEM cross-section images of h-BN thin films which show their thickness. A qualitative thickness measurement is given by XPS Ni 2p 3/2 peak also shown in Figure 2.17. XPS is a surface sensitive characterization technique, with photoelectrons ejected from the outer ~ 10 nm of the sample surface. By analyzing two h-BN films on Ni substrate with the same XPS analysis conditions, we compare the intensity of the underlying Ni signal. For a thicker h-BN film, the Ni signal is relatively weak, as seen in Figure 2.17. Multiple TEM cross-section samples were prepared from different h-BN films, with different growth times, and the h-BN film thicknesses were directly observed. A plot of h-BN film thickness, measured by TEM cross-section, vs. h-BN growth time is shown in Figure 2.17. There is a linear trend of increasing thickness with increasing time.

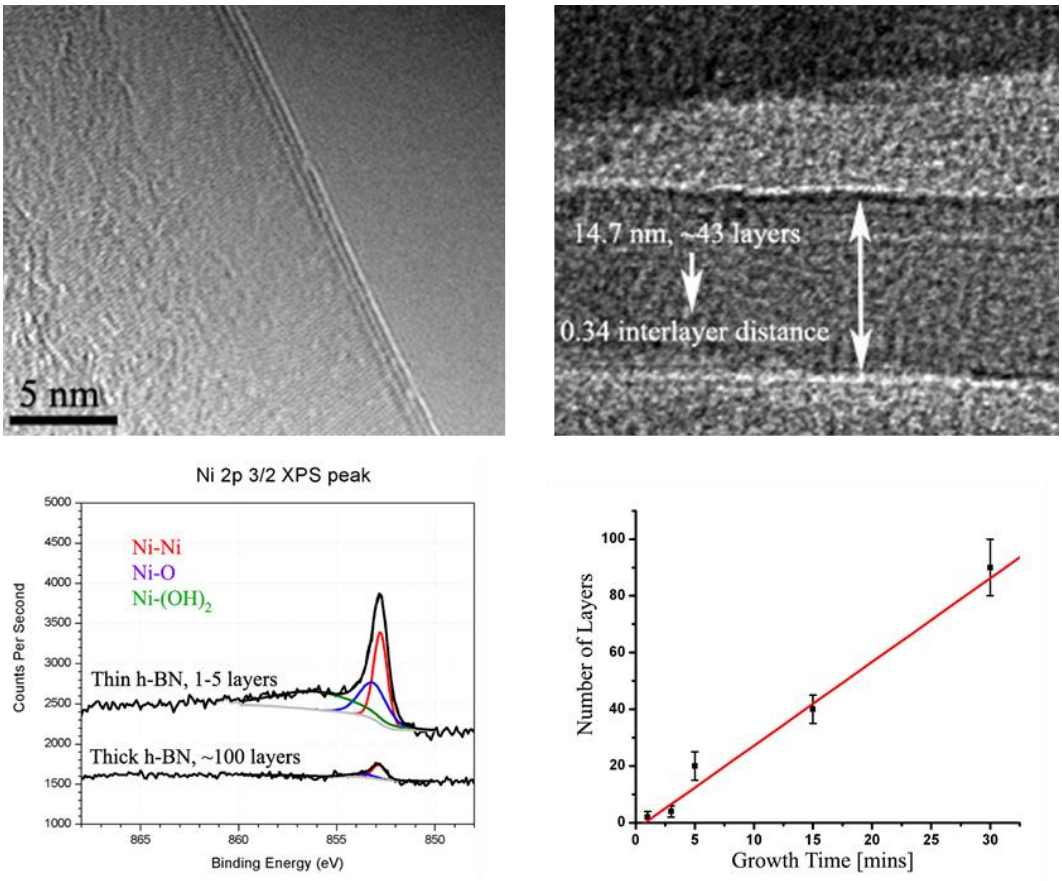

Figure 2.17: Thickness of h-BN film increases with growth time. Thickness determined by TEM cross section and qualitatively by substrate Ni XPS signal.[54] Adapted with permission from Reference 54. Copyright 2012 American Chemical Society.

2.3.3 Formation of Intermediary Compounds During Growth

In characterizing the h-BN films by XPS, observations were made which gave some indication about the growth mechanism. As was mentioned above, the core level electrons ejected in XPS, and the photoelectrons which are detected, have binding energies which depend on the bonding of the atoms in the sample. Thus, multiple binding energy peaks observed for B 1s core electrons, for example, are an indication that B atoms are bonded at multiple binding energies, or multiple oxidation states. Meaning that they are bonded to

different atoms. Different h-BN films which were produced indeed showed different bonding depending on the growth conditions, which was an indication that other intermediary compounds were formed during growth. To reiterate, this project was led by Dr. Ariel Ismach and I performed the XPS analysis. An additional insight was gained when performing experiments which sequentially flowed the two precursor gases, diborane and ammonia, rather than simultaneously flowing them as in a typical growth process. The XPS analysis showed different compounds on the substrate depending on the dosing order, in other words, diborane first followed by ammonia and vice versa. It was found that exposing only diborane resulted in boron oxide and nickel boride compounds on the substrate, as might be expected. The h-BN phase was detected by XPS in addition to the other compounds with "first, diborane only" flow followed by "ammonia only" flow. However, when the order was reversed, only the h-BN phase was seen with the "first, ammonia only" process. The boron-containing compounds observed in the diborane-first process suggest that there is a route to obtaining h-BN through the formation of intermediary compounds.

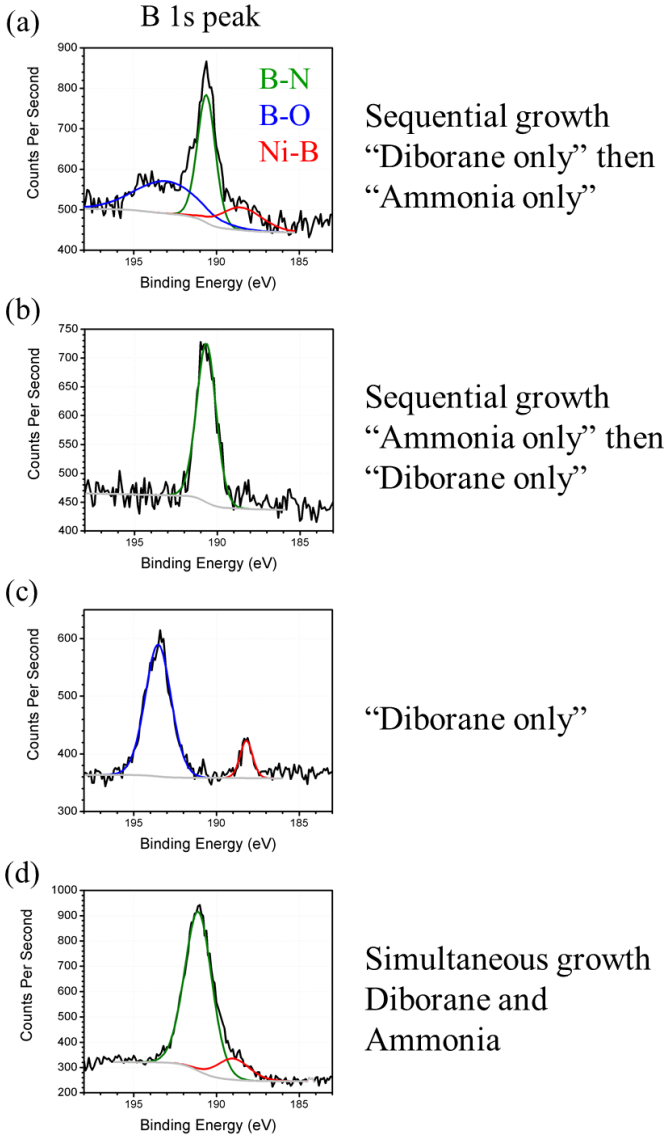

Figure 2.18: XPS of B 1s peak comparing (a) Diborane first sequential growth, (b) Ammonia first sequential growth, (c) Diborane only exposure, and (d) Simultaneous growth. B-O peak near 193.5 eV and Ni-B peak near 188.5 eV.[54] Adapted with permission from Reference 54. Copyright 2012 American Chemical Society.

To clarify the XPS analysis, the B 1s peak for different growth conditions is shown in Figure 2.18. The diborane-first, then ammonia (5 minutes flow of each precursor

separated by 10 minutes of only hydrogen flow) growth XPS spectrum is shown with B 1s peaks corresponding with B-N bond (190.6 eV), B-O bond (193.8 eV), and Ni-B bond (188.8 eV) all clearly distinguishable. This shows that oxide and boride compounds exist on the substrate surface along with the h-BN. For growth using the opposite precursor flow order, ammonia-first, XPS spectrum is shown with only a single B 1s peak for the B-N bond (190.6 eV). A control experiment was also performed with diborane-only precursor flow, and that XPS spectrum gave B 1s peaks with only B-O bond (193.4 eV) and Ni-B bond (188.3 eV). And a typical h-BN growth process was run with diborane and ammonia flowed simultaneously showed a B 1s XPS spectrum with B-N and Ni-B bonds detected. These analyses suggest that the formation of boron oxide and nickel boride on the substrate surface is an indication of a reaction pathway from the precursors to the h-BN product. The pathway including intermediate compounds forming during growth shows some competing reactions occurring at the surface which control the growth mechanism for h-BN.

2.3.4 Controlling the Reaction Pathway with Carbon

The work in section 2.3.3 showed that intermediary compounds are formed during h-BN growth, which is a concept written about by others in the field as well.[58] We continued to investigate the growth mechanism for h-BN growth on Ni, still led by Dr. Ariel Ismach. We were able to understand the reaction pathway through introducing carbon into the h-BN synthesis process. It was observed that boron oxide and nickel boride compounds were present during the formation of h-BN,[54] and those compounds were also observed in the synthesis with ammonia borane precursor. Others have also reported the presence and importance of boron oxide compounds during h-BN growth.[62] In this work, evidence was gathered showing that the CVD synthesis mechanism could be triggered via thermal reduction from oxide intermediate compounds to h-BN, whereas other synthesis

studies have attributed different mechanisms such as surface energetics of the growth substrate.[13] It is shown that the reduction to h-BN is aided by the inclusion of carbon, hence we adopt the phrase "carbo-thermal reduction" mechanism for h-BN synthesis.[71,72] This synthesis study shows that, for the interior of Ni enclosures (into which mass transport is suppressed), h-BN formation occurs through a boron oxide intermediary compound which is reduced in the presence of carbon.

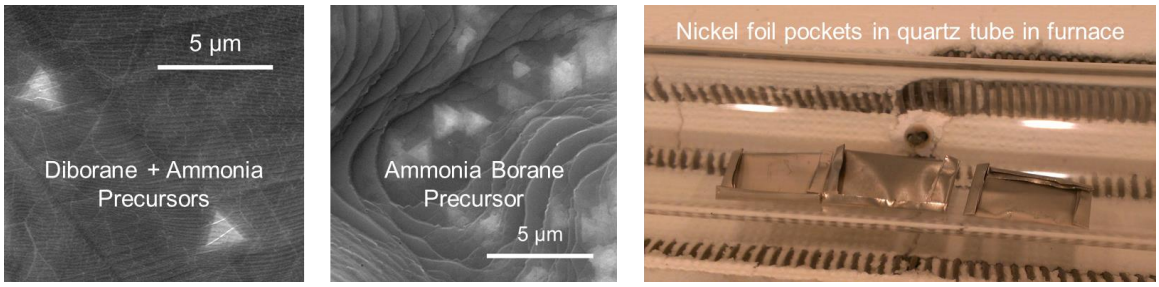

Figure 2.19: SEM images of h-BN grown on Ni foil, with different precursors use yielding similar h-BN films. Also photograph of Ni foil pockets.

Figure 2.19 shows SEM images of h-BN film grown on Ni substrates with different types of precursors. The growth process was modified from section 2.3.2 to using ammonia borane precursor. The SEM shows similar morphology of thin h-BN with triangular adlayers. The curved step shapes are a part of the Ni substrate and are commonly seen on some Ni grains in the substrate after growth.[56] These carbo-thermal reduction experiments were similarly performed in a tube furnace, as depicted in Figure 2.10. To control the flow of the solid ammonia borane precursor to the furnace and the growth substrate, there are two features of the growth system that are important. The first is the separately heated vessel holding the ammonia borane powder. As described above, heating ammonia borane causes a thermal decomposition process which has $B_xN_yH_z$ compounds as byproducts.[66] For this system, the vessel is heated by lowering into a heated oil held at 100 - 130° C. The

second feature of the growth system relevant for h-BN growth is the bypass valve. When the ammonia borane is heated to decomposition, the total pressure in the system also rises. To control the flow of precursor to the growth substrate, the precursor flow is diverted through the bypass as the pressure increases until the temperature and pressure reach a pseudo steady-state. At this point (pressure has increased ~ 50 mtorr), the valve is flipped and the precursor flow is instead directed into the furnace and growth substrate. In these carbo-thermal reduction h-BN growths, the enclosure substrate was again used. As described above in section 2.2.3 for a Cu foil substrate, a Ni foil was folded into an enclosure to create a different environment for the inner surface (precursor flow is greatly suppressed). Figure 2.19 shows a photograph of three Ni foil enclosures loaded in the quartz tube in the furnace before beginning the growth process.

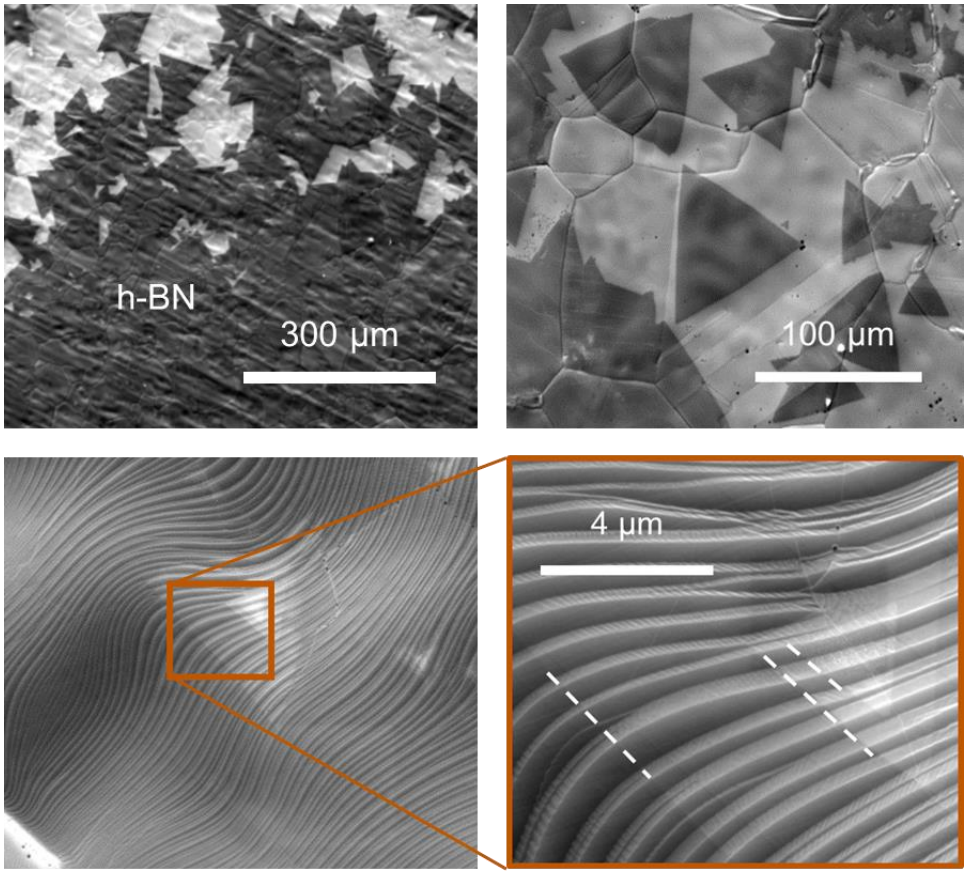

Figure 2.20: SEM images of h-BN grown on Ni foil by the carbo-thermal reduction process. The dark contrast in the top two images show the h-BN domains and the bottom two images show that adlayers of h-BN are lighter in contrast and triangular in shape.[56] Adapted from Reference 56.

The carbo-thermal reduction growth process begins the same as the earlier process described in section 2.3.2 and Figure 2.13, with loading a Ni foil substrate into the quartz tube and pumping down to base pressure, except that the substrate in this process is a Ni foil enclosure. During the heating process, the oil below the ammonia borane vessel is also heated. During the substrate annealing portion, the vessel is lowered into the oil and the decomposing precursor is directed through the bypass. The growth portion is initiated by flipping the precursor valve to flow into the furnace and recall that hydrogen flow is kept

constant throughout the heating and annealing step (typically 10 sccm flow rate). This growth process introduces carbon to the reaction in two primary ways, one with solid amorphous carbon powder and the other with methane gas, which will be described in greater detail below. The cooling process is the same as prior growth processes (cooling under hydrogen or argon). It was observed that thick h-BN is grown on the exterior of enclosures with ammonia borane precursor and no influence on the growth was detected due to the presence of carbon. The h-BN film on the exterior of the enclosure was similar to that obtained on Ni foil using the earlier process described in section 2.3.2. However, h-BN is not grown in the interior surface of the enclosure except when carbon is present. Figure 2.20 shows SEM images of h-BN domains grown on the interior surface of the Ni enclosure with amorphous carbon present. As with previous growths, we clearly observe triangular h-BN domains and adlayers, as well as curved steps of the underlying Ni substrate.

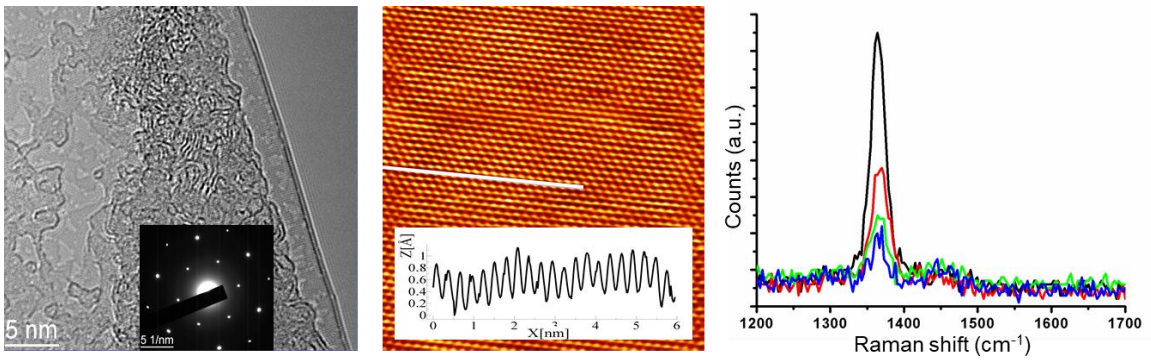

Figure 2.21: TEM and Scanning tunneling microscopy (STM) images of h-BN synthesized by carbo-thermal reduction process, TEM was transferred. Raman spectra showing peak intensity corresponding to thickness.[56] Adapted from Reference 56.

Figure 2.21 shows more characterization of the h-BN grown on the interior surface of the Ni enclosure. The TEM here shows a folded edge of the h-BN showing two atomic layers and an inset SAED showing a single hexagonal crystal pattern. Scanning tunneling microscope (STM) maps were also taken of h-BN on the Ni substrate. This analysis also gives atomic resolution and verifies that h-BN was formed given the atom arrangement and spacing. The Raman spectra shown in Figure 2.21 are taken from an adlayer region of h-BN where an increasing number of layers gives a more intense E_{2g} h-BN peak at ~ 1370 cm^{-1}.

Carbon was introduced into the h-BN growth process in two different ways, as first mentioned above. The first was to add a small quantity (~ 2 mg) of amorphous carbon powder into the Ni foil enclosure. After completely folding shut, then the carbon remains inside the enclosure. It was observed after the growth process that some carbon would diffuse into the Ni and re-segregate as graphite. However, the h-BN did form on the interior surface of the enclosure away from the powder and the graphitic regions. No graphitic material was observed to be incorporated with the h-BN. Due to the difficulty in controlling the positioning of the carbon using a solid source, the second method for introducing carbon was by flowing methane gas. Methane was flowed to the chamber (2 – 10 sccm) during the ammonia borane exposure step only. Again in this case, only h-BN was detected on either the interior or exterior surface of the Ni enclosure and no graphitic material was detected. We see in the Raman spectra from Figure 2.21 that no graphitic peaks are detected from the h-BN film.

In section 2.3.3, diborane and ammonia precursor growth experiments were done and intermediary compounds were detected after h-BN growth (boron oxide and nickel boride) by XPS. Here, we again use XPS to analyze the carbo-thermal reduction growth results and to understand the h-BN growth mechanism. In Figure 2.22, we compare four

different growth samples, all measuring the interior surface of the Ni enclosure. The top row sample is from a growth where no carbon was present at any point in the process. The second row sample is a growth with solid amorphous carbon inside the Ni enclosure where the growth gave isolated h-BN domains, as can be seen in the SEM image. The third row from the top is from a sample also with solid amorphous carbon inside the Ni enclosure but where the growth was a continuous h-BN film. The bottom row sample is a growth with methane exposure during the precursor exposure step. The left column shows a SEM image from each sample, the darker contrast indicating the presence of h-BN. The B 1s spectra from each sample shows a parallel with the results from section 2.3.3. In the carbon-free experiment, only B-O bond was detected and no h-BN was synthesized. Also, there was no nitrogen detected as seen in the N 1s spectra for the top sample. The B 1s and N 1s spectra for the remaining three samples show a trend of increasing B-N bond intensity, from isolated h-BN domains, to full h-BN coverage with solid amorphous carbon, and last to full h-BN coverage with methane. Simultaneously there is a trend of weakening B-O bond intensity. We interpret this as boron oxide formation giving way to h-BN growth, in other words, boron oxide reducing to h-BN. The C 1s and O 1s spectra for the samples also show a trend where more complete h-BN growth (with methane exposure giving full h-BN coverage) means less oxide presence. We see that the presence of carbon reduces primarily the B-O bonds, but also C-O and Ni-O bonds, to grow h-BN, with methane being most effective in driving this reaction.

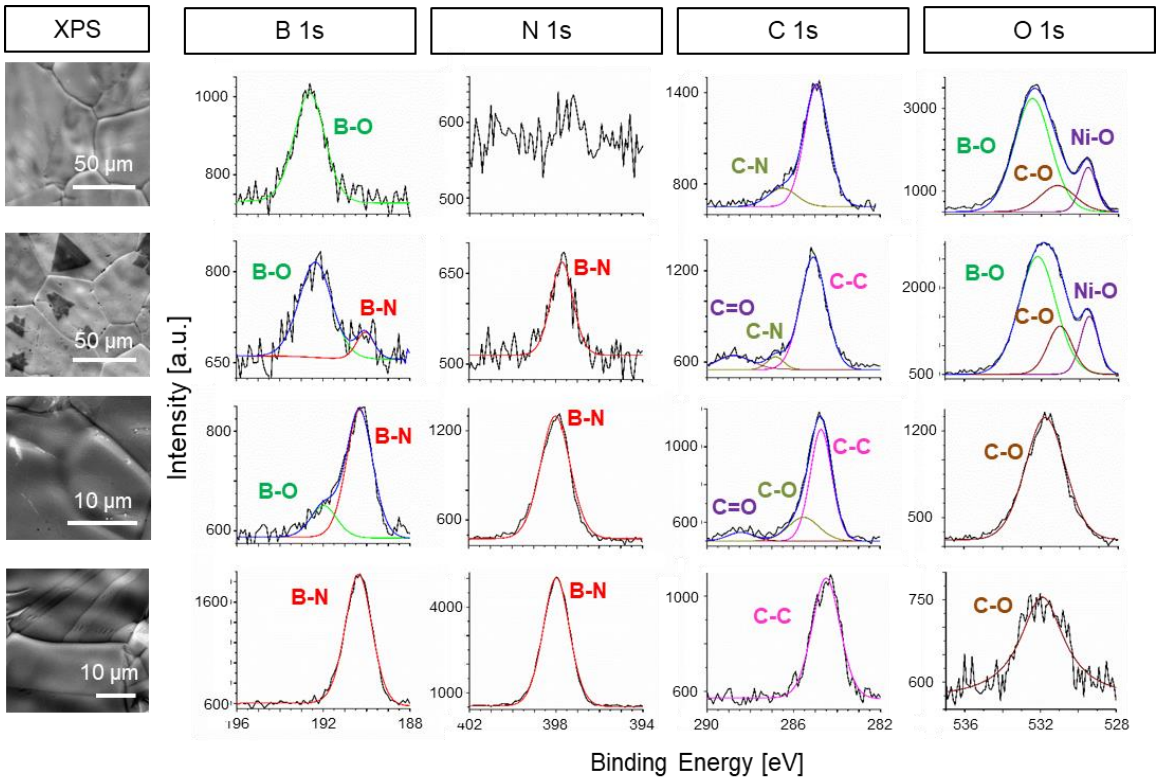

Figure 2.22: XPS analysis comparing different samples in each row. Oxide formation appears in cases where h-BN has not covered.[56] Adapted from Reference 56.

The role of carbon in the growth mechanism for h-BN is understood to be in aiding the reduction of oxides, which is explained by the thermodynamic driving forces acting in the growth process. Often reaction mechanisms are summarized as competitions between thermodynamic (or energetic) forces and kinetic (like diffusion or other mass transport) forces. The growth of h-BN on the interior surface of Ni enclosures was controlled by the energetic forces because of the observed growth products (including oxides) and because of the suppressed mass transport into the enclosure interior. Work by Dr. Yufeng Hao on Cu enclosures showed gaps in the foil after folding and annealing less than one micron in size.[42] Such a small gap would result in a pseudo steady state flow of precursor to the interior of the enclosure. To support the conclusion that thermodynamic driving forces

control the growth mechanism, based on the observed growth products, the possible chemical reactions occurring at the sample surface were tabulated and the free energy of formation (ΔG_f) for each reaction was plotted. Figure 2.23 shows two plots of Ellingham curves associated with the tabulated possible chemical reactions. They are separated by oxidation reactions and reduction reactions. Note that in addition to ammonia borane (decomposition byproducts), carbon, and hydrogen, oxygen is an inevitable element present in the system, due to the nature of vacuum systems. The Ellingham curves are plotted from known thermodynamic constants for each compound in each reaction found in the CRC Handbook of Chemistry and Physics. The more negative the free energy of formation for a given temperature, the stronger the thermodynamic driving force for that reaction. For the growth temperature of our experiments, the favored oxidation reaction favors forming boron oxide over nickel oxide. For the growth temperature of our experiments, the favored reduction reactions include carbon-containing compounds in forming h-BN. Thus, the observed formation of h-BN in the presence of carbon is explained by the stronger thermodynamic driving force acting on the reduction reaction from boron oxide to h-BN. This type of growth mechanism also explains other observed phenomena. For example, there was no significant incorporation of carbon impurity in any h-BN, which can be understood because the favored reactions form gaseous carbon monoxide or carbon dioxide compounds.[73]

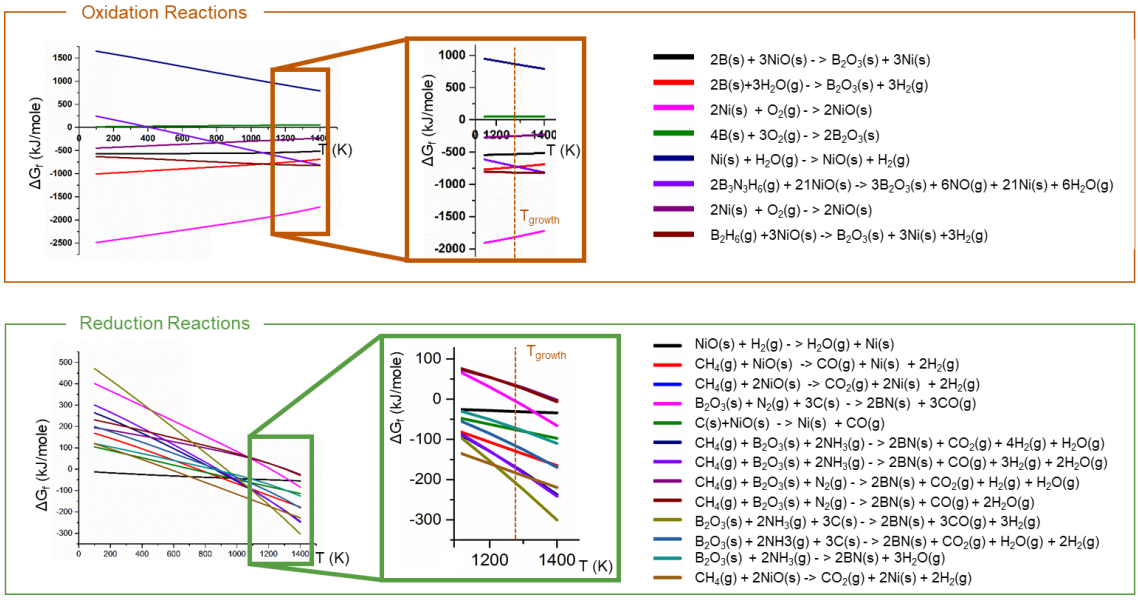

Figure 2.23: Ellingham curves for tabulated reactions during CVD. Top shows possible oxidation reactions and bottom side shows reduction reactions. The lowest curve at a given temperature is most thermodynamically favorable.[56] Adapted from Reference 56.

The growth mechanism for the carbo-thermal reduction to form h-BN can be described as initially oxidation occurring on the interior surface of the Ni enclosure, where mass transport is suppressed (and thus thermodynamic driving forces dominate). Based on the thermodynamics, we have boron oxide forming at elevated temperature and then being reduced via reactions involving carbon compounds to form h-BN. An additional analysis was done to verify this growth mechanism, SIMS depth profiling and mapping were used here. A sample with solid amorphous carbon powder included in the growth was taken, this way isolated domains could be studied. Figure 2.24 shows SI maps from a region with a few triangular h-BN domains, the left column showing SI maps after 1 second of sputtering (removes surface contaminants due to *ex situ* handling) and the right column showing SI maps after 4 seconds of sputtering (removing fully the h-BN atomic layers). The BN^- SI map shows clearly the location of the triangular h-BN domains. The BO_2^- SI

maps show that boron oxide was primarily located away from the h-BN domain, where there was no h-BN there was boron oxide which had not been reduced. The NiO^- SI maps show that nickel oxide formed also away from the h-BN domain. Depth profiles were also generated comparing the h-BN triangular domain region, shown in green in Figure 2.24, and the h-BN-free regions, shown in blue in Figure 2.24. We see the BN^- (and a lesser proportion of BO_2^-) SI falling off in intensity after the h-BN domain is sputtered away, and the Ni_3^- SI increasing as we profile into the bulk. The NiO^- SI signal is weak and near the detection limit. For the h-BN-free region, the BO_2^- SI is found at the outer surface, with the NiO^- SI beneath that. And then further sputtering shows the bulk nickel with Ni_3^- SI. The SI species were chosen as representative of the various compounds and is discussed in depth in Chapter 3. These SI depth profiles indicate that boron oxide is an intermediary compound in the formation of h-BN atomic layers. It is also noted in the SI depth profiles that surface oxide formation limits boron to the surface, in other words it does not diffuse into the bulk of the Ni.

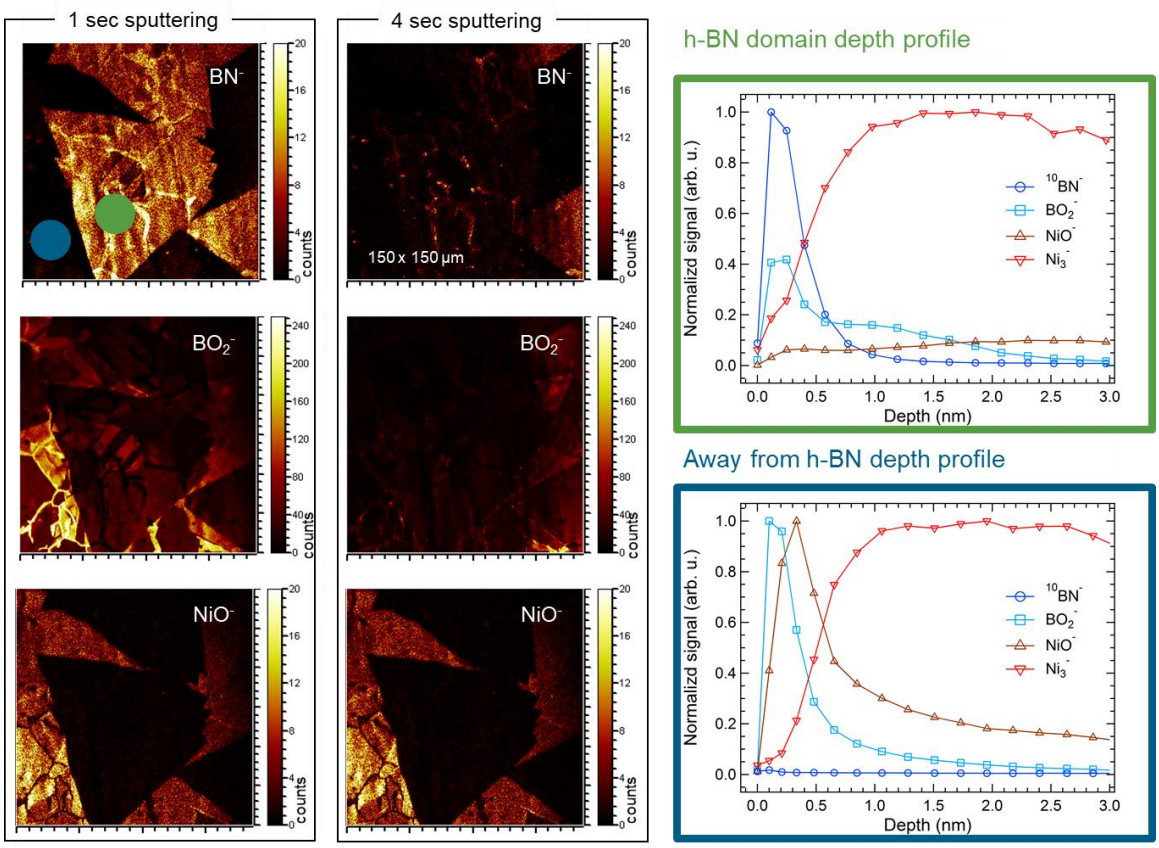

Figure 2.24: TOF SIMS mapping and depth profile showing oxide formation and location on h-BN synthesized by carbo-thermal reduction.[56] Adapted from Reference 56.

The growth experiments discussed here demonstrated a carbo-thermal reduction process that yielded h-BN films. The growth mechanism was shown to be thermodynamically controlled due to the use of Ni enclosure substrates and including a carbon source. To reiterate, this research was led by Dr. Ariel Ismach and I performed the growth experiments, the XPS analysis, and the SIMS analysis. The full report found at Reference 73 includes additional characterization done by collaborators at Carnegie Mellon University.

2.3.5 Diffusion Controlled Growth and Surface Energy Literature

The previous sections 2.3.3 and 2.3.4 summarized how the growth mechanism for h-BN formation was determined in a thermodynamic, or energetic, driven process. For section 2.3.4, thermodynamic control was enabled, in part, by using Ni enclosure substrates. The enclosure substrate is useful to restrict mass transport of precursors to the interior surface, but their hand-made nature is not compatible with large-scale growth processes. Therefore, it is important to perform growth experiments on bare substrates and to continue to evaluate the growth mechanism. The competition between energetic driving forces and kinetic driving forces acting to control the growth mechanism was mentioned in section 2.3.4. In work published by Dr. Sushant Sonde, kinetic driving forces of diffusion and segregation were reported to control the growth mechanism of h-BN on nickel and cobalt thin films.[55] For the case of graphene growth, section 2.2.3 and 2.2.4 described processes where diffusion and segregation also controlled growth. Other researchers have also reported experimental results that show h-BN growth processes where kinetic driving forces (such as diffusion) are controlling the growth mechanism, such as the work by Dr. Stephan Hofmann's group at Cambridge.[74] In contrast to these reports, others have attributed the h-BN growth mechanism to energetic driving forces. Lee *et al.* and Cho *et al.* reported that the surface energy of the nickel substrate controlled the growth rate of h-BN thin films.[57,58] This discrepancy in the literature in some cases is due to a distinct growth process, such as our use of an enclosure substrate or others use of highly controlled molecular beam epitaxy (MBE) equipment, however it is important to clarify the growth mechanism so that processes for h-BN growth can be refined, optimized, and scaled.

2.3.6 Single Crystal Substrate Growth

The pursuit to better define the h-BN growth mechanism continued with more growth experiments. Single crystal substrates have often been used to isolate growth mechanisms for many different processes, because the surface is highly predictable and able to be modeled. For example, early work showing h-BN formation was done using MBE-type systems on Ni (111) single crystals.[52,75,76] Here, we use Ni single crystal substrates to study the h-BN growth of our scalable LPCVD process (in this case done in the rapid thermal CVD, RTCVD, system from Reference 55). As was mentioned in section 2.3.5, other researchers have considered the effect of the Ni substrate crystal orientation on the growth process. Lee *et al.* observed that Ni (100)-like grains in poly-crystalline Ni (polyNi) foil showed a higher growth rate. The higher growth rate was attributed to a higher surface energy of the (100) catalyst surface, enhancing the sticking coefficient of the precursor on the Ni surface, though they acknowledged that the catalytic effect was not fully understood, and that there are multiple reaction pathways for the growth of h-BN.[58] Cho *et al.* observed that Ni (110)-like grains in polyNi showed a higher growth rate and determined that precursor radicals had different sticking coefficients on Ni based on the surface energy of the Ni grains.[57] Hite *et al,* on the other hand, considered the surface energy effect in CVD synthesis of h-BN with another catalytic substrate, Cu, and found it was not a limiting factor.[77] In continuing to better understand the growth mechanism, single crystal Ni substrates were used to try to understand the growth kinetics of h-BN using diborane and ammonia as precursors. We find that, under the same growth conditions, h-BN has the highest growth rate on (110), followed by (111), and with (100) having the lowest growth rate. We associate the orientation dependence to not only surface energy, but also to a difference in the diffusion of B and N in the bulk of Ni and also the h-BN/Ni interface, depending on the orientation of Ni. The diffusion difference necessarily affects

the diffusion, precipitation, and h-BN layer-by-layer growth on the Ni substrate. That is, the growth for h-BN on Ni is not strictly dictated by surface energy as others have reported, but that the energetic forces must be reconciled with kinetic forces, such as diffusion along the Ni/h-BN surface, to better describe the growth.

These single crystal substrate growth experiments were done using the system shown in Figure 2.11, with lamp heating. Diborane and ammonia precursors were used during growth. Recall from Figure 2.15 the visible thickness differences in h-BN film which was transferred to an SiO_2/Si wafer substrate. We observed, as well as was reported in References 57 and 58, that the h-BN film thickness was different depending on the underlying Ni grain in the case of a polycrystalline Ni (polyNi) substrate. Figure 2.25 shows h-BN films after they have been transferred to a TEM grid. Again, we observe the layered structure (and layer spacing) indicative of h-BN and also the hexagonal SAED pattern.

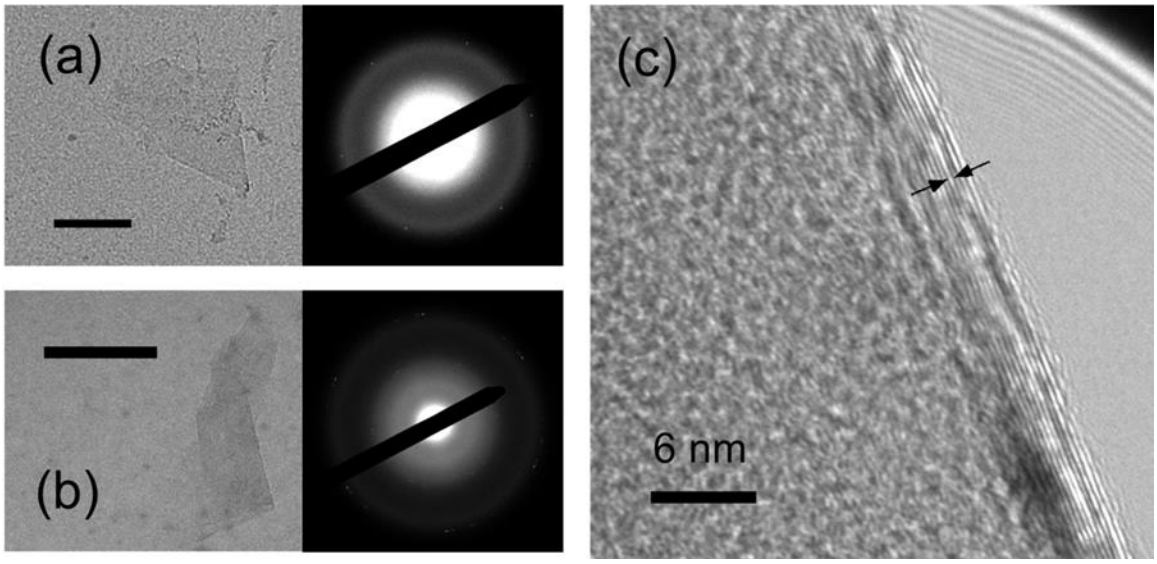

Figure 2.25: TEM images of h-BN film transferred to sample grid showing diffraction and layer-to-layer spacing indicative of h-BN.

Figure 2.26 further shows an EBSD map overlaid onto a SEM image of h-BN on polyNi with corresponding high magnification SEM images for 3 regions with a crystallographic orientation close to (100), (110) and (111). There was no observed preferred orientation of the Ni substrate, such as the low surface energy surface (111) as noted in other reports.[57,78]

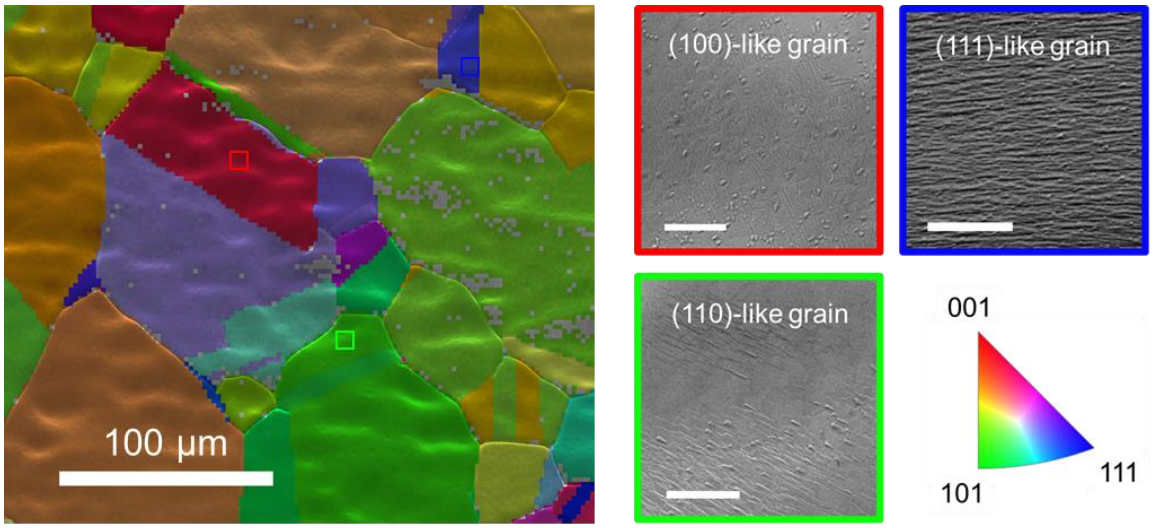

Figure 2.26: SEM and EBSD of h-BN film grown on polyNi substrate.

It is noted that the h-BN thickness on polyNi depends on the underlying Ni grain orientation and the grain-to-grain difference in h-BN thickness affects the measured thickness of h-BN on polyNi. To correlate the relative thickness of h-BN grown on different Ni grains, the sample grown on polyNi was also taken for time of flight secondary ion mass spectroscopy (TOF SIMS) after EBSD. The TOF SIMS mapping of secondary ions representing h-BN are shown Figure 2.27 and show that relatively greater h-BN content was seen for a Ni (110)-like grain than for a neighboring Ni (100)-like grain. The greater h-BN content shows that the h-BN is thicker on the Ni (110)-like grain than for the Ni (100)-like grain. Figure 2.27 shows the secondary ion map of $^{10}BN^-$ integrated from 0

to 5 seconds of sputtering with a 1 keV Cs^+ sputtering ion beam in the middle image. There is a greater intensity of counts of $^{10}BN^-$ for the h-BN on top of the Ni (110)-like grain compared with a neighboring Ni (100)-like grain. The $^{10}BN^-$ secondary ion species forms from the analysis ion beam (30 keV Bi^+) impinging on the h-BN and is used to reliably locate and track h-BN.[55,79] This indicates that there is a thicker h-BN film over the Ni (110)-like grain which qualitatively agrees with the thickness trend of h-BN film observed for the Ni single crystal substrates. The C_2^- secondary ion map is also shown in the right image in Figure 2.27, it gives a clearer picture of the sample surface and the Ni grains. The C_2^- secondary ion map also shows a grid-like pattern of spots which are due to electron-beam induced deposition which occurred during EBSD analysis. This confirms that the TOF SIMS analysis location matched the EBSD analysis location. The left image of Figure 2.27 is the SEM and EBSD map of the same sample region before TOF SIMS depth profiling. The inset cubes represent the orientation of the Ni (110)-like grain in green and the Ni (100)-like grain in red.

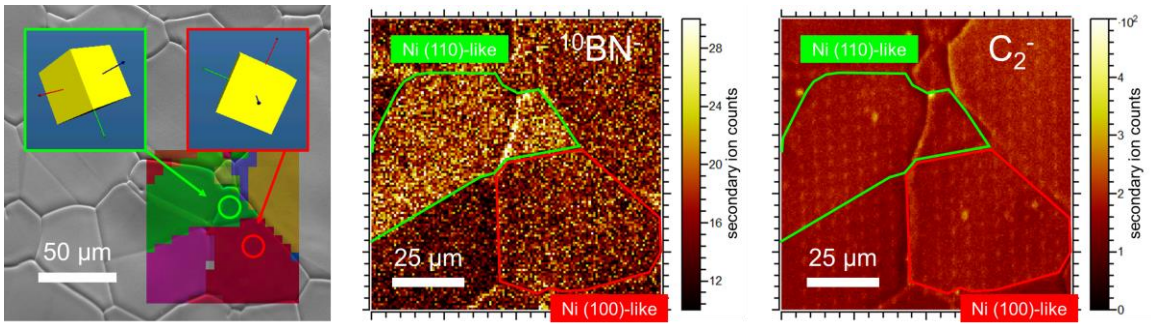

Figure 2.27: Left image shows a SEM image and EBSD map overlaid for an h-BN film grown on polyNi substrate. The Ni grain boundaries are visible in the SEM image and the EBSD map color indicates the orientation of the underlying Ni grain. The color shown follows the same key as in Figure 2.26. The inset boxes are representations of the cubic crystal orientation of the Ni at the location indicated. The green outline indicates a Ni (110)-like grain and the red outline indicates a Ni (100)-like grain. The middle image shows the secondary ion map of $^{10}BN^-$ ions collected from the same region of the same sample. The green outlines Ni (110)-like grains and have greater $^{10}BN^-$ counts, indicating a comparatively thicker h-BN film. The red outlines the Ni (100)-like grain and has comparatively fewer $^{10}BN^-$ counts, indicating a thinner h-BN film. The right image shows the secondary ion map of C_2^- ions and more clearly shows the Ni grain boundaries.

Hexagonal BN on single crystal Ni was grown using the same conditions as growth on previous polyNi substrates, and for each run we place a polyNi substrate as a control. The single crystal Ni substrates were purchased from MTI Corporation and with dimensions of 10 x 10 x 0.5 mm, a purity of > 99.99% and the orientation was within ±2° of the indicated plane. Figure 2.28 shows SEM and XPS analysis for polyNi and the single crystal Ni substrates with three orientations after h-BN CVD growth. The first column shows high magnification SEM images, and second and third columns show the XPS spectra of B and N, respectively. The second column shows the B 1s XPS spectrum for each sample taken under the same conditions, *i.e.* integration time and energy range. The B 1s XPS spectra show a single peak near 190.5 eV, which is the same as measured in previous sections and published reports, without any other B-containing phases, such as

boron oxide. The third column shows the N 1s peak for each sample and again we observe only a single N 1s peak for each scan, suggesting there are no other N-containing compounds forming on the Ni substrates. The N 1s peak is seen near 398.0 eV for all samples, which is the value expected for B-N bonds. An XPS survey scan, which also captures the substrate Ni transition peaks for thin films, was used to determine the relative thickness of the h-BN layer on each sample as shown in Figure 2.2. We consider the work by Hite *et al.* and take a similar approach, though we normalize to the polyNi sample for a relative thickness, rather than an effective thickness.[77] The relative thickness of the h-BN was obtained by normalizing to that of h-BN on the polyNi (1.0); thus the h-BN on the Ni (100), (110), and (111) have relative thicknesses of 1.0, 1.8, and 1.5, respectively.

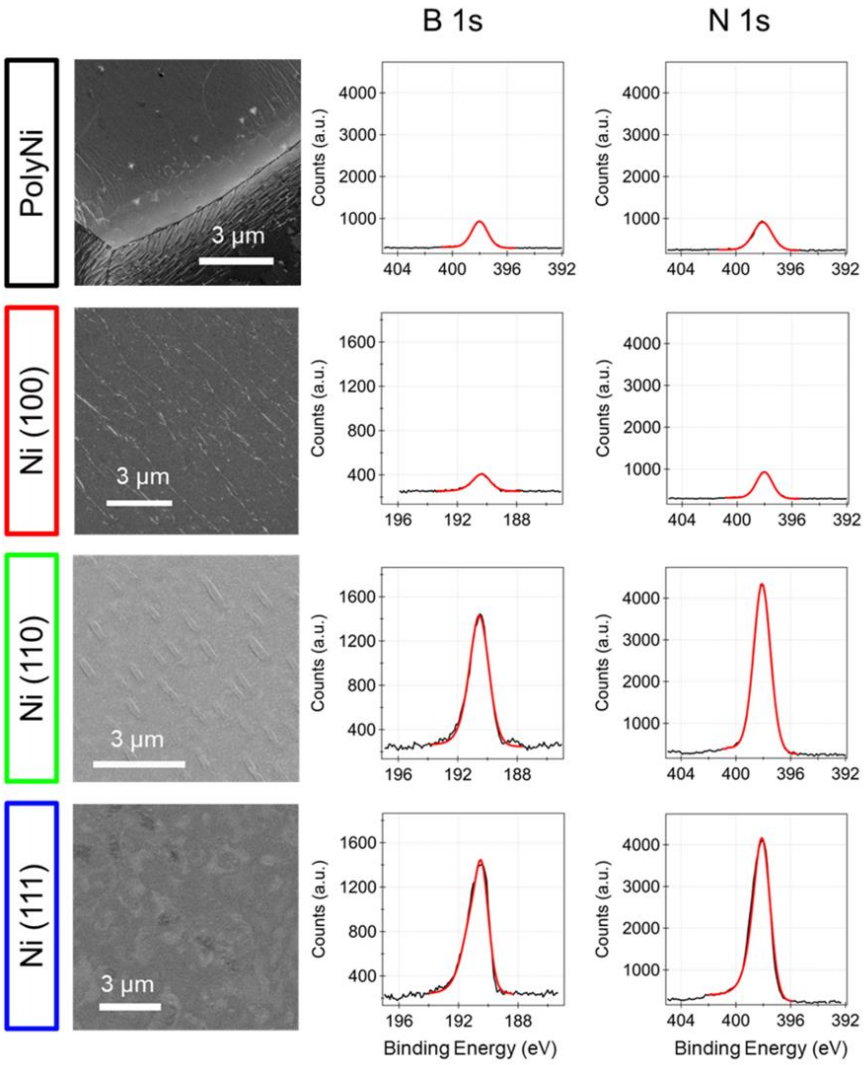

Figure 2.28: XPS B 1s and N 1s peaks showing h-BN films formed on each Ni substrate.

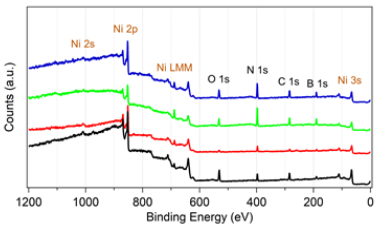

h-BN Substrate	B conc. (at. %)	N conc. (at. %)	Ni conc. (at. %)	O conc. (at. %)	C conc. (at. %)
Poly Ni	15.4	15.2	17.4	21.8	30.2
Ni (100)	24.0	24.4	26.5	10.5	14.6
Ni (110)	31.2	31.3	5.8	9.8	21.9
Ni (111)	25.9	25.7	10.4	25.6	12.4

Figure 2.29: XPS surveys from each h-BN CVD sample grown and a table comparing the atomic concentration of different elements in the h-BN samples.

In order to preserve the relatively valuable Ni single crystal substrates, a different transfer process was utilized which does not etch the Ni. Figure 2.30 illustrates the bubbling transfer method which was adapted from other published work.[80] After spin-coating the sample with PMMA, the PMMA/h-BN/Ni was connected to the positive lead of a DC power supply. The negative lead was connected to a counter electrode Ni foil. 0.1 M NaOH was used for the electrolyte and 0.7 - 0.9 A current was driven at 18 V to form H_2 bubbles at the h-BN/Ni interface. When the bubbling had fully separated the PMMA/h-BN from the Ni substrate, the sample floated off and was transferred into deionized water for rinsing. The PMMA/h-BN was then lifted out of the water by a wafer substrate, and after drying the PMMA was removed with acetone.

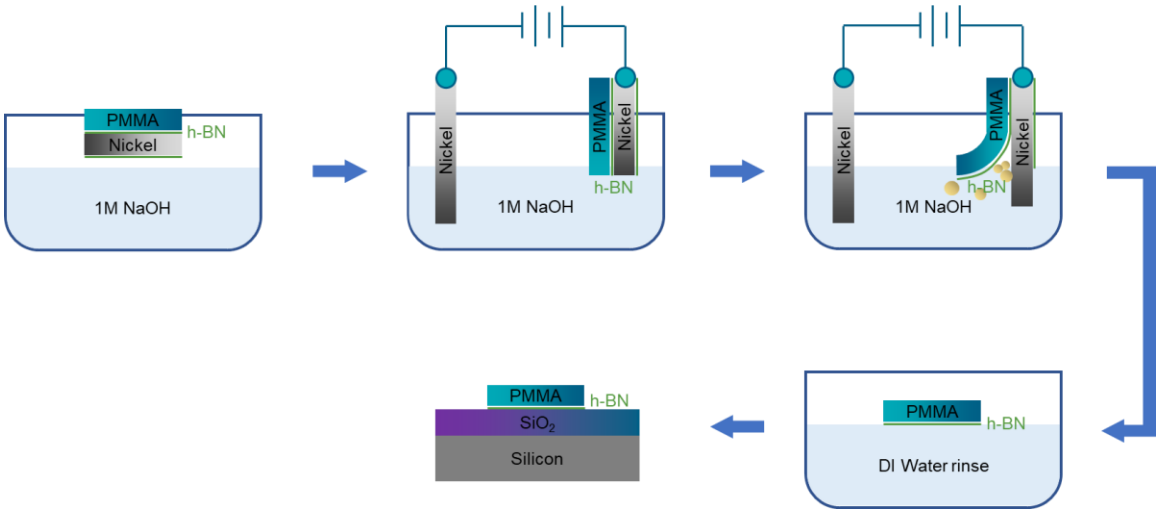

Figure 2.30: Schematic of bubbling transfer process for h-BN.

The h-BN films were transferred onto SiO_2/Si wafers and analyzed by Raman and AFM. Figure 2.31 shows the Raman spectra from each the polyNi grown h-BN, Ni (100), (110), and (111). We see that the h-BN E_{2g} peak intensity follows the same trend as relative

h-BN thickness measured by XPS, Ni (110) with highest intensity, followed by (111), and (100) ~ polyNi.

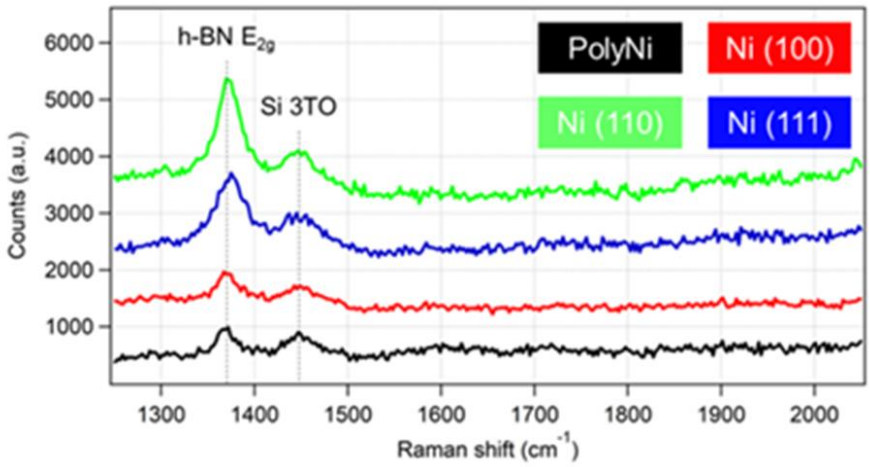

Figure 2.31: Raman spectra from h-BN films grown on each Ni substrate.

Figure 2.32 shows AFM images at the edge of a transferred h-BN (or a region with folded h-BN) film from each Ni substrate. The AFM gives a thickness of 4.5 of h-BN for Ni (110), 3.4 nm for Ni (111), 2.5 nm for Ni (100), and 3.0 nm for polyNi substrate. The XPS, Raman, and AFM analyses all indicate that the h-BN film thickness depends on the Ni grain orientation and has a decreasing order, from thickest to thinnest, of Ni (110), (111), and (100) ~ polyNi. It is noted that the h-BN thickness on polyNi depends on the underlying Ni grain and may affect the measured thickness of h-BN on polyNi.

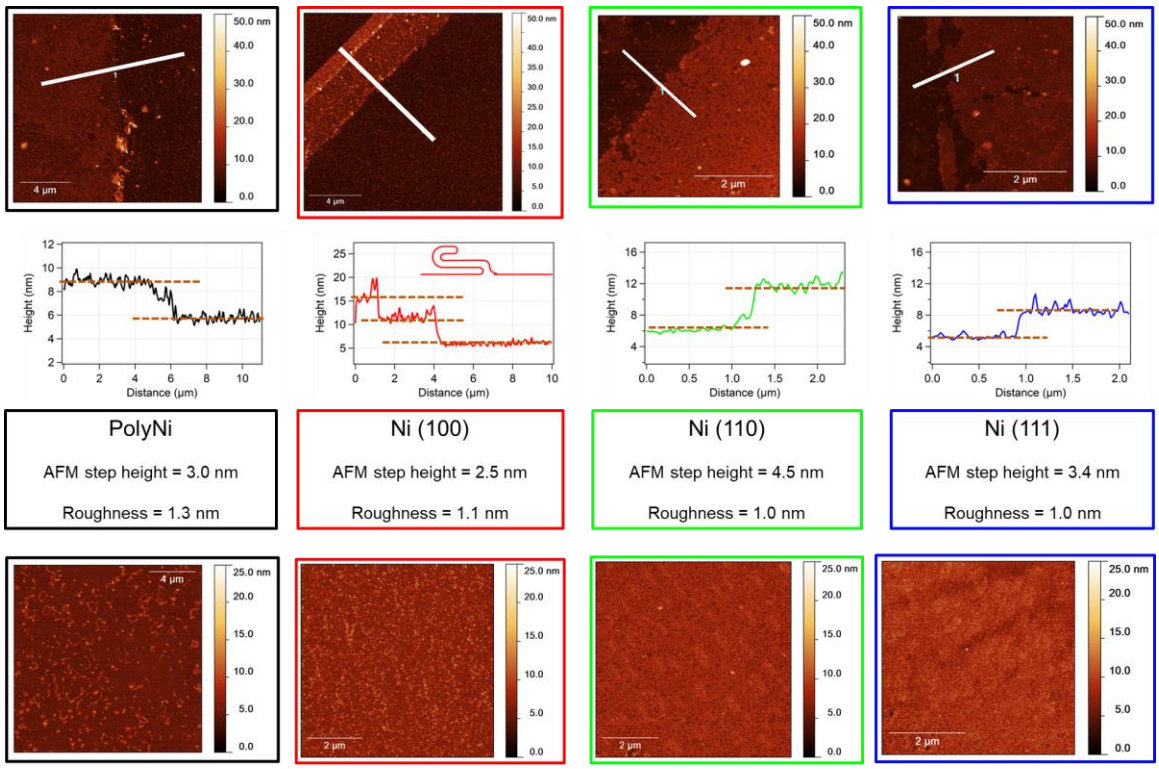

Figure 2.32: Step height profiles by AFM from h-BN transferred to SiO_2/Si wafer substrates showing the thickness of h-BN grown on different Ni substrates (each column represents a different Ni substrate sample). The top row shows the AFM scan from each h-BN film, the second row shows the step profile along the white line in the top row scan, and the third row indicates the sample details and the AFM results. The last row shows the AFM scan of the h-BN film giving the roughness of the transferred h-BN after vacuum annealing to remove PMMA residue.

A direct method for measuring the layer number for the h-BN film can be done with TEM cross section. The atomic resolution of the TEM allows us to individually count the number of h-BN layers. TEM cross sections are shown in Figure 2.33 from h-BN grown on the different Ni single crystal substrates. The nature of preparing TEM samples is such that the layer number determined for the h-BN film is for only a small region of the overall sample. In the case that there is non-uniformity in the sample thickness, then the thickness of the h-BN as determined by TEM is less meaningful. Taken together with the AFM-

determined roughness of the h-BN and the observation that the h-BN layer number is varying within a single TEM sample, we see that the thickness trends qualitatively hold up (and supported with the XPS and Raman characterization), but also that the precise layer number of the h-BN film depends on the uniformity. The cross-section TEM for h-BN on Ni (100) shows 5-6 layers of h-BN and the sample prepared from the Ni (110) substrate shows ~ 5 layers of h-BN. The cross-section TEM for h-BN on Ni (111) showed faceting of the Ni substrate and h-BN was not observed in the field of view. The inset for the h-BN on Ni (100) cross-section TEM image shows an SAED pattern from the Ni substrate showing the expected cubic pattern. The cross-section samples all show individual Ni atoms in the substrate and no Ni grain boundaries. An issue in observing growth on different single crystal orientations here, with respect to uniformity, is illustrated by the h-BN grown on Ni (111). Cho *et al.* noted difficulty in observing growth on the Ni (111)-like grains of polyNi.[57] The surface diffusion work showed that faceting was prominent on the Ni (111) orientation.[81,82] Our TEM cross-section from the Ni (111) sample also showed high roughness and the appearance of facets, which is clearly visible in Figure 2.33. This rough topography may result in some non-uniformity of h-BN film growth and difficulty in determining a dependable thickness.

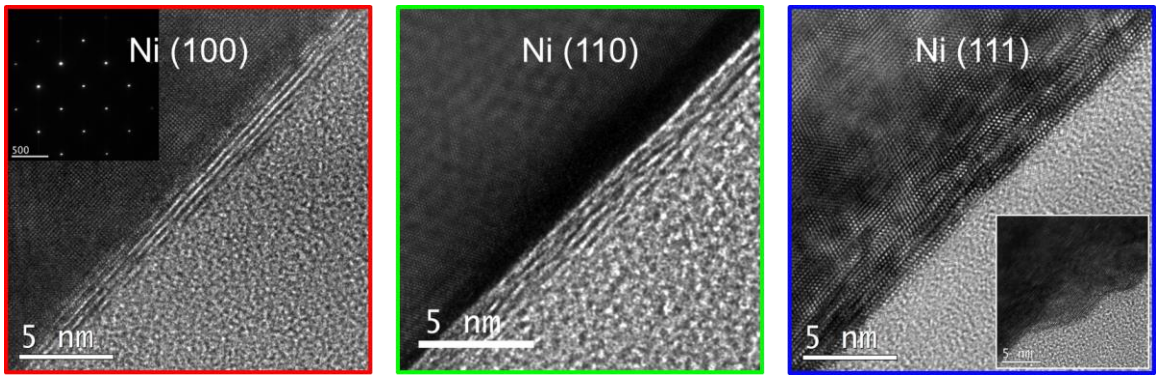

Figure 2.33: TEM cross section samples taken from the single crystal Ni substrate and the h-BN film grown. The upper left of the images shows the substrate Ni and the layered fringes show the h-BN layers. The Ni (111) substrate shows no observed h-BN on the prepared TEM sample, and the inset shows a region where faceting of the Ni (111) was seen. The inset of the Ni (100) TEM image shows the diffraction pattern from the Ni substrate part of the field of view, giving a single cubic pattern.

Figure 2.34 shows SEM and EBSD maps of h-BN on Ni from each of the single crystal substrates, with each column representing a different Ni substrate orientation. The EBSD maps in the second row show that after the growth process the Ni substrate retains its original orientation with negligible recrystallization. With these maps, we can conclude that the h-BN is indeed forming on the expected single crystal surface, rather than forming on a recrystallized Ni surface of another orientation. This is consistent with results observed by others who have studied h-BN grown on Ni,[83] however it contrasts with the recrystallization of Cu single crystals observed by Hite *et al.* during their h-BN growth.[77]

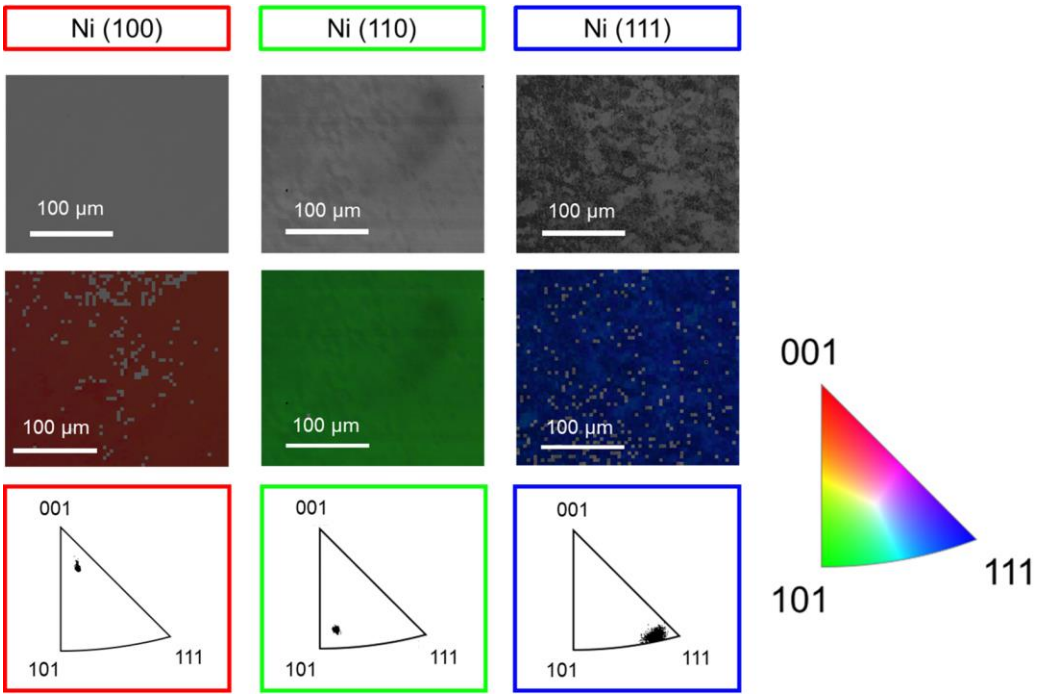

Figure 2.34: EBSD and SEM from h-BN grown on each Ni single crystal substrate, the orientation is of the substrate Ni.

We observed h-BN formation on Ni single crystal substrates with different orientations and it is seen that the thicknesses of the h-BN grown are different, which has also been observed by others.[57,58] However, our results show that under our growth conditions, h-BN has a higher growth rate on Ni (110), followed by Ni (111), and Ni (100). This is in contrast with Lee *et al.* who reported Ni (100)-like as having the highest h-BN growth rate which was ascribed to its relatively high surface energy compared with other orientations.[58] In comparison with this work, Lee *et al.* carried out the CVD process at higher growth pressure and gas flows, as well as a different precursor (ammonia borane) and a lower temperature (800°C). On the other hand, Cho *et al.* observed that Ni (110)-like yielded the thickest h-BN films, followed by (100)-like and (111)-like, and concluded that the sticking coefficient of precursor-containing compounds (which is governed by the

surface energy of the different Ni grains) affected the thickness.[57] Cho *et al.* used a CVD process with a higher temperature, 1100°C, and with a different precursor, borazine, to grow on polyNi substrates as compared with this reported process. It is clear that there are many factors that influence the growth kinetics of h-BN on Ni, from surface energy to surface reactions and diffusion on Ni.[13,56] In our earlier work, we showed with the addition of carbon, that competing surface reactions would favor the reduction of boron oxide to form h-BN. It was important to create a "protected" surface (the interior of a Ni enclosure) to effectively control the Ni surface energy and reactivity.[56] From section 2.3.4, it was noted that oxide formation at the Ni surface prevented B diffusion into the Ni bulk, which is consistent with other reports which studied oxidation of Ni surfaces after implanting B ions.[84,85] In the growth experiments here, where the substrate surface did not oxidize, the B and N are free to diffuse into the Ni. In contrast, it has also been reported that B and N diffusion play a primary role in h-BN film growth (rather than surface energy and reactivity).[55,86,87] Indeed, it is necessary to consider the formation of h-BN multilayers on catalytic surfaces via diffusion and segregation. Therefore, surface energy effects as well as diffusion, or kinetic, effects must be reconciled during the formation of h-BN on Ni and other similar metals. The degree of each effect is dependent on process conditions which can be challenging to disentangle.

In this work, we used Ni single crystal substrates with different orientations to grow h-BN films under the same conditions to clarify some of these competing growth mechanisms. Prior reports, which argued that substrate orientation dependence of h-BN growth is connected to the surface energy of each distinct orientation (thus affecting the sticking coefficient of precursors, for example), showed inconsistencies in which orientation gives the fastest growth and the ascribed growth mechanisms neglected to consider B and N diffusion.[57,58,83] The results reported in this work show yet another

different trend in h-BN growth rate for each orientation of Ni substrate, though to the best of our knowledge this is the first study to compare growth rate using multiple single crystal Ni substrate orientations (as opposed to measuring orientation of polyNi substrates). These varying reported results suggest that the h-BN growth mechanism on Ni depends on multiple process parameters. These results show that the growth is not controlled by surface energy, since when taken together with the orientation dependence observed by Lee *et al.*[58] and *Cho et al.*[57] do not agree with the surface energy hierarchy for Ni single crystal orientations Ni (110) > Ni(100) > Ni(111).[78,88,89] As discussed in section 2.3.5, diffusion has been identified as a controlling factor in h-BN growth and Desrosiers *et al.* have shown how diborane is decomposed and B readily diffuses into Ni bulk at high temperatures.[90] It is understood that both impurity diffusion and self-diffusion are connected to vacancy formation and mobility in the matrix crystal, in this case Ni.[84,85] Earlier work by Azzerri and Colombo, building on work by Blakely *et al.*, which studied the orientation dependence of Ni surface self-diffusion at high temperatures, reported that at 1300 K (close to our growth temperature) the diffusivity of the different Ni orientations increased in order from (100), to (111), to (110).[81,82,91] This diffusion rate trend qualitatively matches the h-BN growth rate observed here. This observed difference in h-BN growth can be due to the diffusion of B and N in the Ni bulk and at its surface, or at the interface of Ni and h-BN. Formation of h-BN may occur at the Ni/h-BN interface by B and N segregating out from the bulk and diffusing at the Ni surface. Without observing the nucleation and growth of h-BN domains and multilayers, this cannot be conclusively proven and is left for future work. From Azzerri and Colombo, the surface self-diffusion coefficient of Ni at 1300 K, which is near the growth temperature used here, for (100), (110), and (111) surfaces are 3.1×10^{-6}, 1.3×10^{-5}, and 6.9×10^{-6} cm^2/s, respectively.[81] Interestingly, in the same work by Azzerri and Colombo, the surface self-diffusion coefficient of Ni at 1400 K is reported

to increase from (111), to (100), to (110) (1.7×10^{-5}, 1.9×10^{-5}, and 2.9×10^{-5} cm^2/s, respectively) which is a trend that is in qualitative agreement with the observed h-BN growth rates reported by Cho *et al.* for their growth temperature of 1100°C. The results shown here support the conclusion that diffusion and segregation, at the surface and in the bulk, on different substrate orientations is a function of that orientation and that it affects the growth rate and the final thickness of h-BN films. It is worth considering similarities in growth mechanism here with the formation of graphene bilayers as occurring at the interface between graphene and substrate, as described by Dr. Yufeng Hao in Reference 42.

2.4 2D MATERIALS SYNTHESIS CONCLUSIONS

The objective of my 2D materials synthesis work is, broadly, to better understand the mechanisms during CVD for graphene and h-BN. The methods which have been used include characterization methods (SIMS and XPS) and analysis of thermodynamic driving forces. The characterization results provide evidence that furthers the understanding of graphene and h-BN CVD synthesis mechanisms, and the thermodynamic analysis suggests a specific CVD synthesis mechanism for h-BN which is backed up by characterization evidence. The growth mechanism has multiple of forces acting on it, in competition, and many of those have been outlined here. For graphene synthesis, kinetic control was shown in comparing Cu and Ni substrate growth in section 2.2.1 and 2.2.3 and 2.2.4. We showed energetic control with oxygen in growth in section 2.2.2. For h-BN synthesis, kinetic control was shown in B and N diffusion on single crystal substrates in section 2.3.6. We showed energetic control by carbon dosing in section 2.3.4 and also observed an energetic phenomenon in section 2.3.3.

Chapter Three: 2D Materials Characterization

Growing the body of research and knowledge about 2D materials requires us to have techniques to characterize these materials accurately and precisely. In Chapter 2, much of the supporting evidence for understanding 2D materials synthesis came from materials characterizations. Raman, X-ray photoelectron spectroscopy (XPS), scanning electron microscopy (SEM), transmission electron microscopy (TEM), atomic force microscopy (AFM), secondary ion mass spectroscopy (SIMS), and other techniques were introduced and their relevance for 2D materials was demonstrated in Chapter 2. Raman spectroscopy used for graphene characterization, and its uniquely powerful ability for analyzing graphene, was discussed in Chapter 1.[92] Raman has also proven to be uniquely useful for TMD 2D materials like MoS_2 and WSe_2 as there are unique spectral shifts and also photoluminescence (PL) spectra which can indicate few and single atomic layers of material.[93,94] It is important to develop and demonstrate new characterization techniques which are tailored for 2D materials. Their layered structure can give sharply defined interfaces which can be nicely imaged with TEM, for example, but having single atomic layers also means that in the out-of-plane direction there is a very limited amount of material to probe. This can create issues of interfering signals from surface versus buried layers, which complicates characterization and interpretation.

Combining different 2D materials into vertical heterostructures has given devices which demonstrate unique properties and phenomena,[95,96] going far beyond showing graphene's enhanced behavior on an h-BN substrate. To achieve the optimal performance, it is important that the 2D materials themselves must have as low a defect density as

---

Work described in this chapter is also published in Reference 79 where I led that study and designed experiments and performed sample characterization, and also in Reference 118 where my contribution was in sample characterization. Appropriate citations appear in the text and figures as well.

possible and also that the interface between layers is free from contamination. Therefore, characterization techniques that can probe individual atomic layers and their interfaces are needed.

In this chapter, the research done in characterizing 2D materials and interfaces between hetero-layers will be presented. Time-of-flight secondary ion mass spectroscopy (TOF SIMS) was utilized in conjunction with other characterization techniques to give composition and structural information about 2D materials and their heterostructures. The technique described is well-suited for 2D materials because it can separately analyze single atomic layers and interfaces between layers.

3.1 Unique Challenges to Characterizing 2D Materials

A key driver for research interest in 2D materials is the ability to fabricate vertical heterostructures with different layers to take advantage of different physical and electronic properties, as is written above.[95–98] As the vertical heterostructures consisting of 2D materials contain atomically thin interfaces, analytical techniques that show the planar chemical composition of buried interfaces with atomic resolution are needed. The common fabrication methods for 2D heterostructures, including mechanical exfoliation and polymer-based lift-off processes, introduce contamination as the 2D materials are exposed to several environments before the final stacking configuration.[40,99,100] Because the performance of a 2D heterostructure device is directly linked to the amount, location, and composition of any impurity contaminant, characterization and mitigation of residues are important to study. However, surface characterization techniques all have limitations when dealing with low concentrations in ultra-thin (few nanometers) structures.

Common methods for characterizing 2D material heterostructure contaminants include Raman spectroscopy, electronic device testing, XPS, and TEM. A common

practice is for the 2D materials to be annealed at moderate temperatures (100-400°C) under vacuum for a few hours in order to remove residues.[12,70,101] The effectiveness of these countermeasures can be measured indirectly, such as by shifts in Raman peaks which indicates doping from impurities.[70,102] Several indirect methods, such as Raman and electrical characterization, have been used to determine the quality of 2D materials.[69,103] All fabricated devices have shown some influence from the fabrication process, and the performances of the devices are contingent on the countermeasures. Efforts to directly measure any residues and contaminants have also been reported. Direct characterization techniques such as XPS and TEM have been used to show polymer residues which remain on samples fabricated by the transfer of CVD-grown 2D materials.[100,104] XPS is able to detect carbon bonded in the PMMA structure after the transfer process, and those signals were absent after the sample was annealed under vacuum.[100] In another study, a graphene/h-BN heterostructure was characterized with TEM. In the stacked structure, the researchers detected polymeric carbon residues trapped between the graphene and h-BN layers and is shown in Figure 3.1.[104] Also in Figure 3.1 is an illustration showing surface and interface contaminants in a 2D materials vertical heterostructure. While work has been reported on both indirect and direct measurement of residues and contaminants affecting 2D materials and 2D material heterostructures, each characterization technique has its limitations. For example, TEM can provide a clear image of a local clean or contaminated interface, but that image is local and limited by the number of TEM samples which can be realistically prepared. On the other hand, Raman mapping can give a clear picture of a relatively large area, but the information from different materials often gives overlapping Raman peaks or differences in peak signal. Such is the case for the h-BN peak and the graphene D-band peak.[102] Raman also will have difficulty when characterizing stacked

heterostructures. The laser spot penetration and Raman signal escape from the sample complicates the usefulness especially as more and more layers are added.

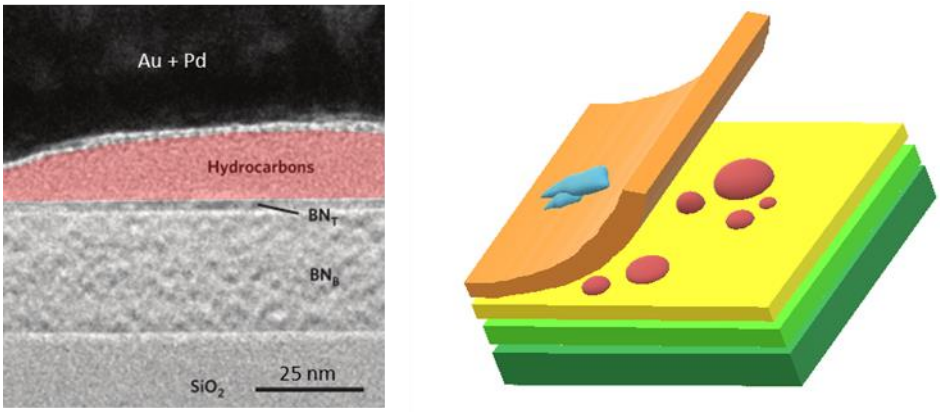

Figure 3.1: Example of 2D material characterization, here a cross-sectional TEM image showing trapped contaminant between 2D material layers of a vertical heterostructure, adapted from Reference 99 (permissions granted by Springer Nature).[99] At right, an illustration showing layered vertical heterostructure with surface and interface contamination.

We published a technique to directly characterize 2D material heterostructures which can provide additional insight for researchers over other commonly used characterization methods. We have used time of flight secondary ion mass spectroscopy (TOF SIMS) in conjunction with Raman mapping and AFM to characterize a graphene-on-h-BN heterostructure.[79] Possessing ultra-high (virtually atomic) in-depth chemical selectivity and parts-per- billion sensitivity, time-of-flight secondary ion mass spectrometry (TOF-SIMS) is a good candidate for characterizing the composition of 2D heterostructures. As an example, in conjunction with atomic force microscopy (AFM), TOF-SIMS can accurately provide fundamental features such as atomic mixing and chemical composition at buried interfaces. This work represents expanded research which focuses on 2D materials characterization compared with analysis described in chapter 2.

3.2 INTRODUCTION TO TOF SIMS

Time of flight secondary ion mass spectroscopy (TOF SIMS) collects secondary ions generated from a sample under analysis. Sample molecules are ionized and ejected from the surface by primary ions focused onto the sample from an ion beam. The mechanism of secondary ion generation is physical, as in sputtering.[105,106] The TOF SIMS analysis described in this chapter was done using a commercial TOF.SIMS5 system made by IONTOF GmhH. Figure 3.2 illustrates the basic TOF SIMS instrument. There are two different primary ion beams used, the (1) analysis beam and the (2) sputter beam. The sputter beam, in our case a Cs^+ ion beam, is operated at relatively lower energy (0.5 – 2 keV) and higher current (10 – 30 nA) and is used for removing the sample surface in depth, for forming sputter depth profiles. The analysis beam, in our case a Bi^+ ion beam, is operated at relatively high energy (20 – 30 keV) and low current (1 – 5 pA) and is used for generating the secondary ions from the sample that are collected by the time of flight mass analyzer. The mass analyzer collects the secondary ions from the sample and times their flight in the analyzer section, higher mass secondary ions take longer time to reach the detector and low mass secondary ions take less time. The analyzer collects a full mass spectrum for each pulse of the analysis beam. By alternating the analysis beam and the sputter beam, mass spectra are collected as the sample surface is sputtered away, giving a depth profile.

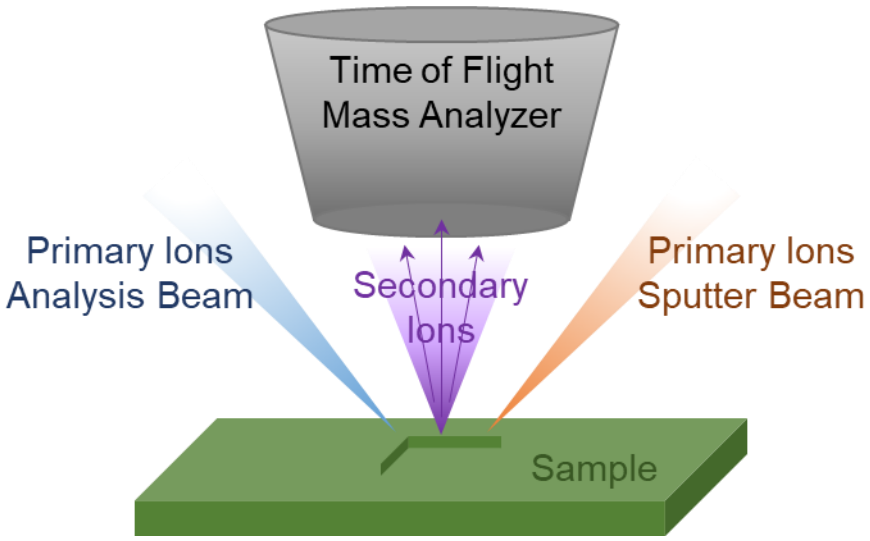

Figure 3.2: Schematic of TOF SIMS analysis technique shows two primary ion beams (1) analysis beam and (2) sputter beam, and also secondary ions generated. The secondary ions are collected by the mass analyzer.

Figure 3.2 is a very basic schematic, for clarity, and it leaves out some other component details. Certainly all ion beam elements for primary ion beams and secondary ion collection (lenses, deflectors, etc.) are not shown in the figure and more fundamental information about SIMS and TOF SIMS are found in References 105 and 106. For example, the analysis chamber is under ultra-high vacuum conditions (base pressure ~ 10^{-9} torr). Charge compensation is often needed to prevent the sample from charging and altering the behavior of secondary ions. An electron gun is used to neutralize any charge buildup at the sample surface. The primary ion bombardment generates secondary ions but those from the sputter beam can be excluded by timing the analyzer column to only accept secondary ions based on the pulses of the analysis beam. Also, secondary ions ejected from the sample may be positively charged, negatively charged, or neutral. The mass analyzer is biased to either accept positive or negative secondary ions and therefore the mass spectra collected for a given analysis can only be one or the other.

By controlling parameters like the primary ion energy, exposure time, and rastering area conditions can be found which give a very slow depth profiling rate. To convert a sputtering time scale into a depth scale, it is necessary to know the thickness and structure of a thin sample. In later sections, it will be shown that combined AFM and Raman characterization was used to determine the sputter rate for 2D material heterostructures. In TOF SIMS, the ability to tightly control the primary ion energy and exposure time, sputter rates significantly slower than a single atomic layer per second can be achieved.

The ionization of the sample and generation of secondary ions is a complex mechanism and so quantitative TOF SIMS analysis is done using relative sensitivity factors (RSF). A reference sample of known concentration for species of interest is analyzed using the same analysis conditions to determine the RSF and then the analysis sample can be run and the concentration, with respect to depth for example, can be calculated. The amount of secondary ions collected in the analyzer and are detected as counts are important to making a reliable quantitative measurement and increasing the integration time (more pulses) of the analysis ion beam is a simple method for increasing counts.

3.3 Combined Characterization to Target Layers and Interfaces of 2D Heterostructures

Our work demonstrating a combined characterization technique using TOF SIMS to characterize 2D heterostructures was written up and published at Reference 79. The technique showed individual characterization of single atomic layers, as well as contaminants at interfacial regions between layers, by focusing on a graphene-on-h-BN vertical heterostructure. The technique shows that there exist detectable residues on top of the heterostructure surface and at the interface between graphene and h-BN. With the

chemical information, the interfacial contamination could be attributed to the CVD growth and transfer process steps.

As was established in chapter 1, graphene on h-BN is a popular heterostructure of 2D materials, and has been used to show some high material performance.[12,107] Recall that the properties of graphene are necessarily influenced by its environment and especially the substrate on which it sits. In chapter 1, the example was used to show the electrical conductivity is an order of magnitude greater on h-BN than for SiO_2 and desirable phenomena such as quantum Hall effect have been achieved in graphene with h-BN as the substrate.[12] Others have shown that an h-BN/graphene/h-BN sandwich structure maintains pristine graphene properties and protects from environmental changes, such as temperature stress.[107]

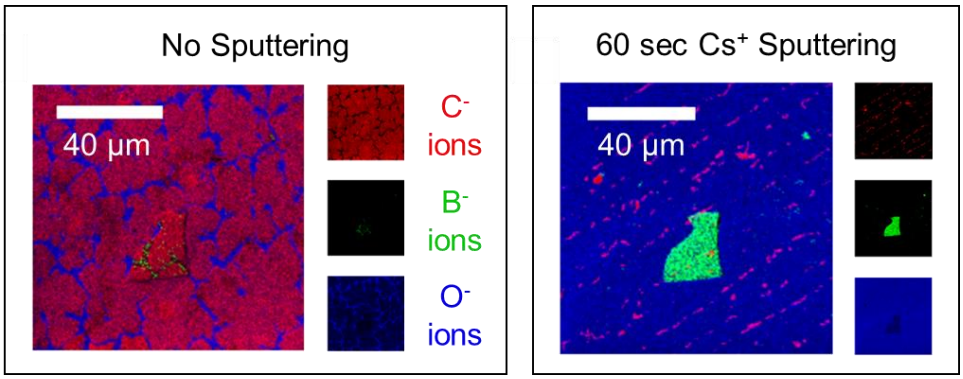

Figure 3.3: TOF SIMS maps of CVD graphene on h-BN flake, C^- in red, B^- in green, and O^- in blue. As-fabricated heterostructure with graphene domains covering the surface at the left and after 60 seconds of Cs^+ sputtering, the graphene layer is removed, revealing the h-BN flake at the right. Scale bars are 40 μm.[79] Adapted from Reference 79.

We prepared a 2D material heterostructure sample in order to study both the material itself and its interface. Our structure was a CVD graphene layer on top of an h-BN flake. The graphene was grown on Cu foil using the CVD process described in chapter

2, and then transferred to a target substrate by a commonly used process.[10] For this transfer, PMMA ($(C_5O_2H_8)_n$) was spin-coated onto the graphene and the Cu was dissolved in 0.5 M ammonia persulfate solution, similar to the process shown in Figure 2.14. Separately, h-BN flakes were exfoliated and deposited onto a SiO_2/Si wafer using a mechanical exfoliation method.[108] The SiO_2 film was 285 nm thick. The CVD graphene, supported by a PMMA film was then placed on top of the h-BN/SiO_2/Si. Lastly, the PMMA was dissolved with acetone (C_3H_6O). This gave the final heterostructure of graphene on top of h-BN on a SiO_2/Si substrate. We deliberately used common processing and transfer techniques in order to study materials and interfaces which are typical of other published results.

Raman spectroscopy, AFM, and TOF SIMS were used to characterize our 2D material heterostructure. The TOF SIMS was configured with a 500 eV Cs^+ sputtering ion beam and a 30 keV Bi^+ analysis ion beam. The detector and analyzer were configured for both high mass resolution collection and high spatial resolution collection, for depth profiling analysis and secondary ion mapping, respectively. Figure 3.3 shows the heterostructure by TOF SIMS mapping before and after sputtering away the CVD graphene layer. The following sections give details on how it is proved that single atomic layers can be controllably sputtered away and analyzed, and other details related to this characterization work.

3.3.1 Raman and AFM to Determine Layer Number

The 2D material heterostructure was first characterized to confirm the desired structure. The CVD-grown graphene was not fully covering the substrate with domains about 10 to 20 μm across, which is commonly referred to as sub-monolayer growth and has been used in synthesis studies to understand nucleation and growth (such as in section

2.2.2).[39,41,109] The heterostructure was first analyzed with Raman to determine the quality of the graphene overlayer. Figure 3.4 shows a map of the graphene G band at 1580 cm^{-1}. The domains are clearly visible here, as are the gaps between the domains. Figure 3.4 also shows representative spectra from the mapped. The spectrum from the graphene region shows a clear G/2D ratio of ~ 0.5, indicating that the graphene domains are monolayer.[109] The spectrum from the h-BN flake region shows a strong and sharp peak at 1365 cm^{-1}.[110] This is attributed to the fact that the flake is relatively thick and the signature is similar to bulk h-BN.[110] The graphene D peak, around 1350 cm^{-1}, is barely detected on the graphene regions and is attributed to defects and dangling bonds in the graphene lattice. Despite the graphene sitting on top of the h-BN, the signal from the buried h-BN is strong. The Raman cannot easily distinguish between layers and a heterostructure with more layers and other 2D materials would compound that problem. In a space from between neighboring graphene domains, the blue spectra in Figure 3.4, we see the h-BN peak in isolation and no graphene Raman signal is detected. AFM results are also shown in Figure 3.4. The flake is clearly visible as it is significantly thicker than the graphene regions. The graphene domains are also visible. From the AFM and the Raman, we see the domains remain continuous despite being ‘draped’ over the h-BN flake. The AFM data also gives the surface topography of the as-fabricated heterostructure. It is determined that the vertical heterostructure is composed of monolayer graphene domains on top of a relatively thick h-BN flake.

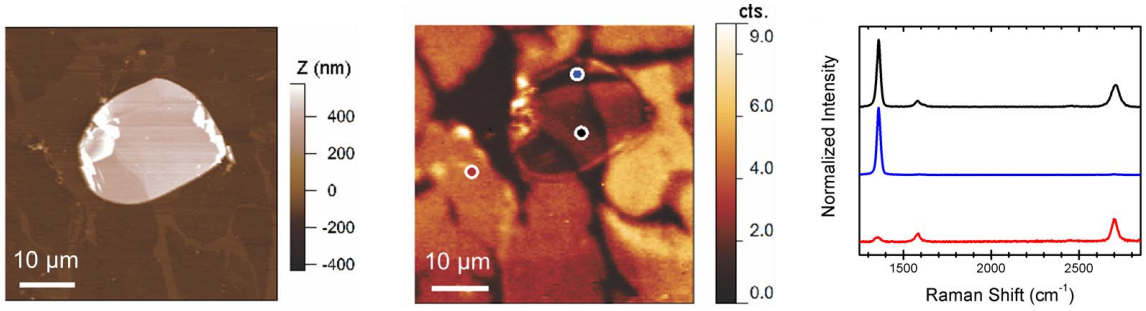

Figure 3.4: Raman and AFM characterization of the graphene on h-BN heterostructure. Left AFM image shows the thick h-BN exfoliated flake with graphene domains on top. The center shows a Raman map of the graphene G-band peak intensity. The right shows characteristic spectra from the location indicated on the center Raman map.[79] Adapted from Reference 79.

3.3.2 TOF SIMS Depth Profiling and Atomic Mixing

The vertical heterostructure sample was put into the TOF SIMS instrument after AFM and Raman for further analysis. By studying the mass spectra, species which originated from the various layers and interfaces were identified. Recall sections 2.2.2 and 2.2.3 where depth profiles of graphene on the growth substrate were shown, here we demonstrate conditions with much higher depth resolution and quantitative analysis that are applied to a 2D material vertical heterostructure. Figure 3.3 in the above section 3.3 shows a secondary ion map of our sample in its initial state and after 60 s sputtering with the 500 eV Cs^+ sputter beam. These maps show clearly that the graphene, as indicated by C^- ions, is completely removed and only the underlying SiO_2, indicated by O^- ions, and h-BN, indicated by B^- ions, remains. This image also demonstrates the high lateral resolution obtained in the "Burst Align" mode of the TOF SIMS. The resolution is similar to that seen in the Raman mapping in Figure 3.4 Some patches of graphene remain even after sputtering. These patches are likely rolled edges of graphene which is a consequence of the transfer process.[109] By controlling the removal of the outer layers to such a slow rate, we

can progressively study the outer adsorbed species, the top graphene, the "sandwiched" interfacial contaminants, and the underlying h-BN and SiO_2.

The secondary ions collected during depth profiling are subject to the roughness of the surface from which they are sputtered. The initial roughness and any roughness induced through sputtering will affect the depth resolution of the collected profiles.[106] In order to (i) understand the physical effects of sputtering on the graphene/h-BN and graphene/SiO2 interfaces, and (ii) estimate sputtering rates for the different 2D material layers, the surface topography of the vertical heterostructure was investigated by AFM before and after 35 seconds of sputtering with Cs^+ at 500 eV energy, shown in Figure 3.5. Both height distributions exhibit two main peaks attributed to the SiO_2 substrate ($Z \approx$ - 65 nm) and h-BN flake surface ($Z \approx 150$ nm). An obvious change in shape from Gaussian to Lorentzian and a strong reduction of the full width at half maximum (FWHM) for the two main peaks suggest that the Cs^+ sputtering significantly decreases the surface corrugation of both the substrate and the h-BN flake surface, where corrugation is defined as the root mean square (RMS) or standard deviation of the height distribution and proportional to its FWHM. The sputtering-induced FWHM reduction of the second peak, representing the h-BN flake, by 10 % (from ~6.6 nm to ~5.9 nm, based on Gaussian and Lorentzian fits indicated in blue, respectively) can be accounted for by the lack of long range flatness of the h-BN flake top surface which contains several terraces and large out-of-plane features. The sputtering-induced FWHM reduction of the first peak, representing the SiO_2 surface, shows a factor of ~5 decrease in FWHM (from ~7 nm to ~1.4 nm) following the sputtering process due to the intrinsic long range flatness of the Si wafer. During depth profiling, the corrugation at the regressing surface which exposes the interface between the graphene and h-BN is assumed to be a combination of the corrugation measured before and after sputtering.[111] Based on the strong surface smoothing effect induced by sputtering, we conclude that the

initial corrugation is reduced substantially during the graphene removal (~10 - 15 seconds of sputtering) thus the interfacial roughness should be closer to the one of the h-BN or SiO_2 substrates, 0.7 and 0.2 nm, respectively. Complete removal of the h-BN flake (~215 nm) and SiO_2 (~285 nm) films reveals sputtering rates of about 0.04 nm/s and 0.14 nm/s, respectively. For the single layer graphene atop the h-BN flake, as shown by Raman mapping (Figure 3.4), the sputtering rate of graphene reads ~0.06 nm/s. The apparent h-BN flake height difference (i.e., spacing between the two major height distribution peaks in Figure 3.5, from ~208 to ~220 nm) reported by AFM following 35 seconds of Cs^+ sputtering can be attributed to the large disparity between the h-BN and SiO_2 sputtering rates and surface corrugation.

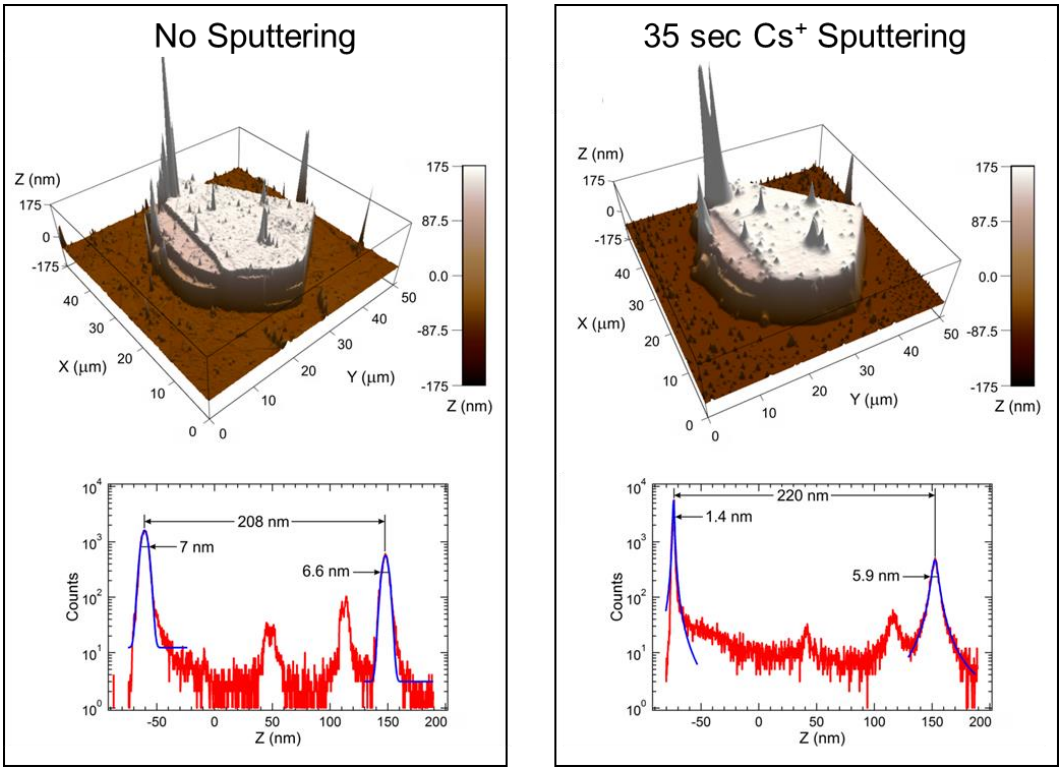

Figure 3.5: AFM characterization of the graphene on h-BN heterostructure before (left) and after (right) sputtering with the Cs^+ sputtering beam for 35 seconds. Bottom shows height histograms.[79] Adapted from Reference 79.

The sputtering time for the vertical heterostructure was converted into depth by applying a sputtering-rate model assuming that the instantaneous sputtering rate at the graphene/h-BN interface is a linear combination of the individual sputtering rates.[111,112] The sputtering rates of graphene and h-BN were estimated, in this case, at 0.09 nm/s and 0.06 nm/s, respectively, given the above calculations (shown in Figure 3.5) and linearity between removal rate of material and the Cs^+ beam areal dose density (inversely proportional with the sputtered area).[113] For converting the sputtering time, t, into a depth, z, a rate model assuming the instantaneous sputtering rate, $R(t)$, at the interface of two films (referred to herein as A and B) as a linear combination of the individual sputtering rates was used:[111]

$$R(t) = \left|\frac{I(t)-I_B}{I_A-I_B}\right| R_A + \left|\frac{I(t)-I_A}{I_A-I_B}\right| R_B = \dot{z} \qquad (3.1)$$

The terms given by $I(t)$ are the normalized secondary ion yield of a species representing one of material A or B, I_A and I_B are the values of $I(t)$ in material A and B, respectively, and $R_A$and R_B are the individual sputtering rates for A and B, respectively. The linear coefficients are essentially proportional to the molar fractions of the two materials at the sputtering time, t.[113] Thus, the sputtering depth, $z(t)$ corresponding to sputtering time, t, is expressed as:

$$z(t) = \int_{t_0}^{t} dt' R(t') \qquad (3.2)$$

Where t_0 is the initial sputtering time. Application of this model on the C_3^- marker for the graphene/h-BN interface permits the conversion $t \rightarrow z(t)$. Figure 3.6 shows normalized depth profiles of C_3^-, CB^- and $^{10}BB^-$ secondary ions representing single layer graphene, adventitious organic material chemisorbed at the h-BN surface, and h-BN substrate, respectively. Polyatomic species like C_3^- and $^{10}BB^-$ were chosen as markers for the graphene and h-BN, respectively, to avoid the intrinsic artifacts monoatomic species like C^- and B^- have due to residuals from oxides or other chemisorbed adventitious species.

An estimation of the atomic mixing length between graphene and h-BN can be obtained by applying the so called mixing-roughness-information (MRI) model to the measured interface length.[114] Details of this model and its application to our case are presented below in this section. Central to this model is the assumption that the measured interface length can be reduced to a convolution between the real atomic mixing, corrugation, and sputtering effects at the interface. There are several equivalent, standard

ways to extract the measured interface length from the depth profile of a heterostructure.[111,112,115] The most common way is to calculate the full width at half maximum (FWHM) of a combined species (in our case CB^-) depth profile. Although suggested by such profile in Figure 3.6, the extended atomic mixing (~0.6 nm after corrugation deconvolution) between graphene and h-BN substrate is ruled out by the CB^- profile of the pristine h-BN (Figure 3.7, h-BN flake-only and graphene-only depth profiles) which yields similar thickness and mass. Instead, the CB^- depth profile for the graphene-free h-BN system implies that adventitious carbon has already mixed with the h-BN surface before the graphene addition, forming a roughly 0.5 - 1 nm thick protective layer. Another way to measure the interface length of the graphene/h-BN interface is to calculate the depth comprised between the 90% and 10% levels of the C_3^- depth profile, leading to a value of ~ 0.3 nm. Based on the surface corrugation of graphene/h-BN surface before and after sputtering (~2.8 and ~0.7 nm, respectively; see Figure 3.5 and 3.6) it is inferred that the actual atomic mixing length between graphene and h-BN is negligible. Therefore, most of the interface length extracted from depth profiling of the graphene/h-BN system is given by corrugation effects. As a result, the graphene overlayer proves to be chemically inert with respect to the h-BN substrate. A similar argument can be made for the graphene/SiO_2 system (Figure 3.7, graphene-only depth profile) suggesting that graphene does not interact with the SiO_2 substrate.

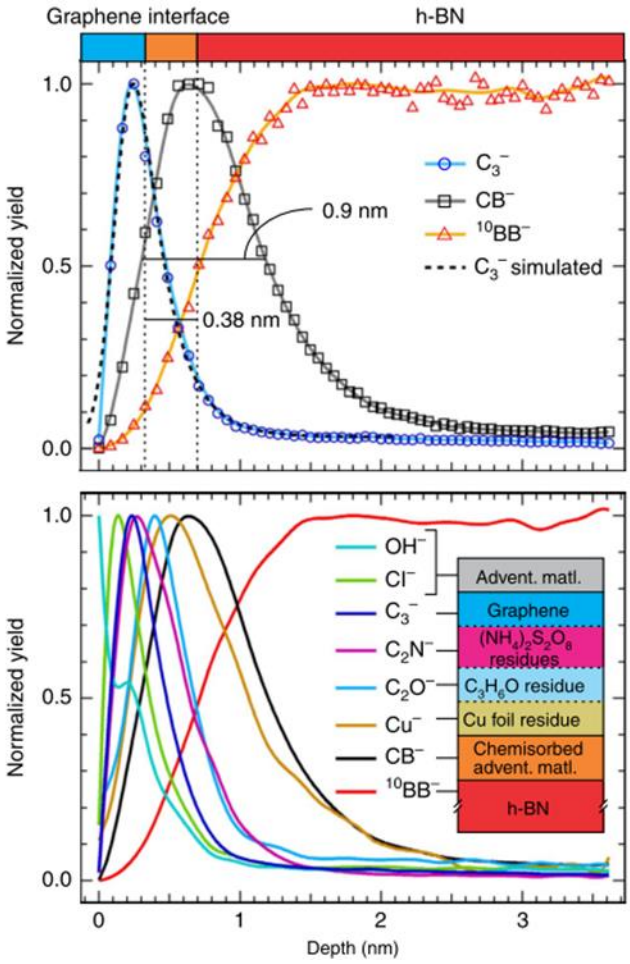

Figure 3.6: TOF SIMS depth profiles of species related to 2D materials and other contaminants. Top shows normalized depth profile for fragment attributed to graphene layer (C_3^-), to interlayer residue (CB^-), and to h-BN flake ($^{10}BB^-$). Bottom depth profiles for additional SI species of interest and schematic showing attribution and layer cake structure.[79] Adapted from Reference 79.

Additional residuals from the transfer process at the graphene/h-BN interface are represented by S^-, C_2N^-, C_2O^- and Cu^- species. Albeit in small amounts, S^- and C_2N^- species show the same depth profile localization as C_3^- thus indicating a chemical interaction between graphene and the lift-off solvent, $(NH_4)_2S_2O_8$. An oxidized, organic, partial monolayer (~0.4 nm thick), presumably a PMMA or, most probably, PMMA/acetone

residue and represented by the C_2O^- marker, can be observed right under the graphene overlayer, followed by a third layer containing traces of copper residue. In fact, a closer look at the shape of the C_2N^- depth profile suggests that its signal originates from three atomic-like layers, giving a pseudo three-layered structure of the transferred graphene system. Further, assuming a similar ionization probability for nitrogen in each layer, the fit of the C_2N^- profile with a sum of three Voigt functions convoluting equal shares of Gaussian and Lorentzian functions and constrained to monolayer graphene widths (Figure 3.6) leads to relative quantification of the amount of nitrogen residue in the graphene overlayer, PMMA/acetone residue underlayer and copper-doped third layer, with ratios of about 1 to 0.35 to 0.11, respectively. Consequently, assuming an isotropic distribution of the nitrogen residue in each layer, the coverage of these three layers reads 1 ML, 0.35 ML and 0.11 ML, respectively. Finally, the copper density at the graphene/h-BN interface was estimated at ~0.05 % of the bulk copper density based on direct comparison of Cu^- secondary ion signals between graphene/h-BN and graphene/copper foil systems (as analyzed and described in earlier chapter 2 sections 2.2.2 and 2.2.3). As a result, the amount of copper in the transferred graphene system (considering its pseudo three-layered structure) equates about 1.35 % of the total mass. Other identified interfacial species (BS^- and CB^-) are a result of chemisorbed adventitious sulfur or carbon, respectively, with h-BN and are formed before the CVD graphene addition. Most of the physisorbed adventitious species (CH_2^-, Cl^-) at graphene, h-BN, and SiO_2 surfaces are diffused to the sides of the graphene domains by the capillary forces exerted at the graphene/hBN or graphene/SiO_2 interfaces. Thus, we show the content and location (in depth) of not only the graphene and h-BN layers, but also remaining residuals from the CVD growth process (Cu^-), the transfer process (S^-, C_2O^- and C_2N^-), and from exposure to ambient (CB^-, CH_2^-, and Cl^-).

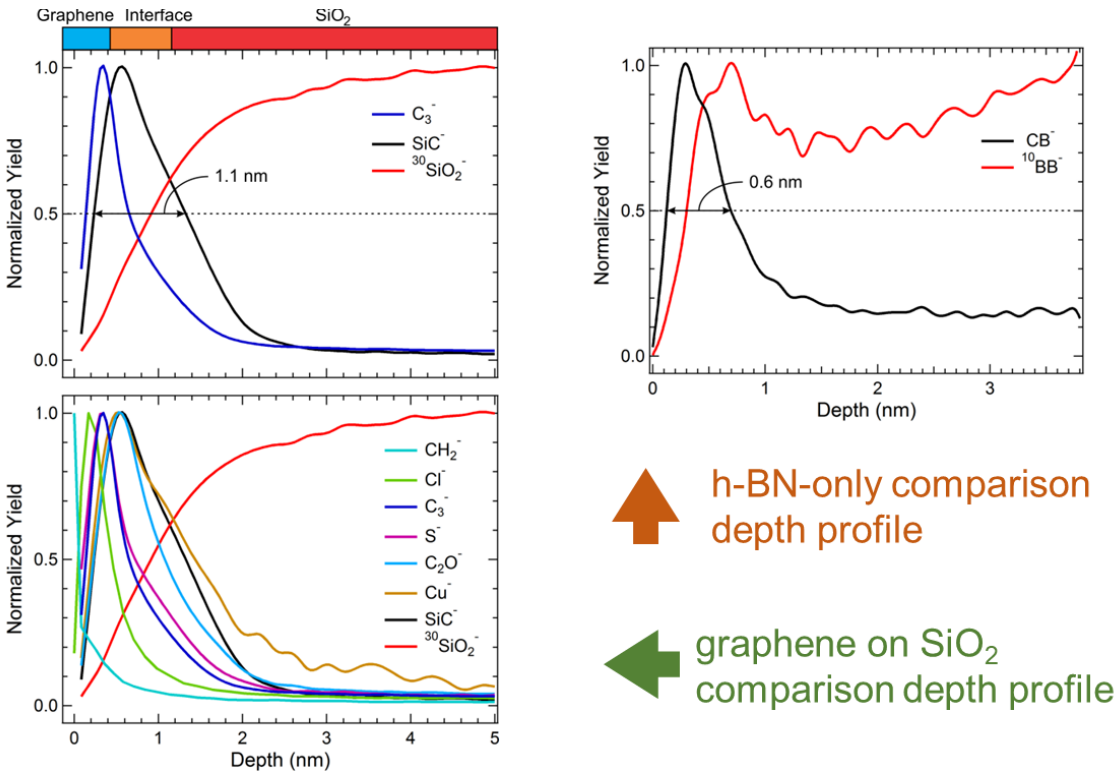

Figure 3.7: TOF SIMS depth profiles of comparison samples h-BN flake only and graphene on SiO_2 for modeling the interface profile.[79] Adapted from Reference 79.

The mixing-roughness-information (MRI) model was utilized to determine the atomic mixing between the graphene and h-BN layers under TOF SIMS analysis.[114] This model is composed of three factors broadening the interface "thickness" (i) sputter-induced atomic mixing, (ii) corrugation of the interface, both as-fabricated and due to sputtering and (iii) the "information depth", or the depth of origin for the secondary ions. The MRI model assumes that these contributors to interface "thickness" can be deconvoluted and is described by analytical functions of depth which are known as the depth resolution function (DRF) when convoluted. Deconvoluting the DRF thus will give the true interface "thickness". Reference 114 gives the functions representing (i), (ii), and (iii) as

$$g_w(z - z_0) = A_w exp\left[-\frac{(z-z_0+w)}{w}\right]\theta(z - z_0 + w) \quad (3.3)$$

$$g_\sigma(z - z_0) = A_\sigma exp\left[-4\ln(2)\frac{(z-z_0)^2}{\sigma^2}\right] \quad (3.4)$$

$$g_\lambda(z - z_0) = A_\lambda exp\left[\frac{(z-z_0)}{\lambda}\right]\theta(z_0 - z) \quad (3.5)$$

Where z is the sputtered depth, z_0 is the running depth for which the contributions are calculated, w, σ, and λ are the (i), (ii), and (iii) parameters, respectively. $\Theta(z)$ is the Heaviside step function (equal to 1 if $z \geq 0$, and 0 else) and A_w, A_σ, and A_λ are normalization constants such that

$$\int_{-\infty}^{\infty} dz\, g_{w,\sigma,\lambda}(z) = 1 \quad (3.6)$$

The (i) and (iii) parameters, w and λ, represent the length to which their respective contributions (g_w and g_λ) drop by a factor of $1/e$. The FWHM of the (ii) represents the RMS of the corrugation at the z_0 plane. This gives the DRF

$$g_{DRF}(z) = \int_{-\infty}^{\infty} dz' \int_{-\infty}^{\infty} dz'' g_w(z' - z'') g_\sigma(z'') g_\lambda(z - z') \quad (3.7)$$

Finally, the normalized depth profile of a certain species (to the maximum secondary ion intensity, I_0) can be written as

$$\frac{I(z)}{I_0} = \int_{-\infty}^{\infty} dz' g_{DRF}(z' - z)\chi(z') \quad (3.8)$$

Where $\chi(z)$ represents the molar fraction of the species at the depth z, i.e. that species' true normalized profile. For a given interface represented by the step edge of the normalized profile $I(z)$, the "thickness" (or depth) from 84.13 % and 15.87 % of $I(z)$ gives the measured interface "thickness". The 84 to 16 % profile levels are standard in the SIMS community and can be used where the DRF can be represented by a Gaussian.[113] The modeled normalized profile for the graphene layer is used for the forward calculation procedure with the C_3^- profile in the form[114]

$$\chi(z) = \theta(z - z_0 + d_{gr}) \left\{1 + exp\left[\frac{3.33587(z-z_0)}{w_0}\right]\right\}^{-1} \quad (3.9)$$

Where d_{gr} is the graphene thickness as determined by Raman and AFM and w_0 is the (i) atomic mixing length and is then further deconvoluted for the contributions of w, σ, and λ parameters. The resulting calculated normalized depth profile is a match for the normalized depth profile as-measured, and the C_3^- profile is shown in Figure 3.8 for the graphene on h-BN vertical heterostructure.

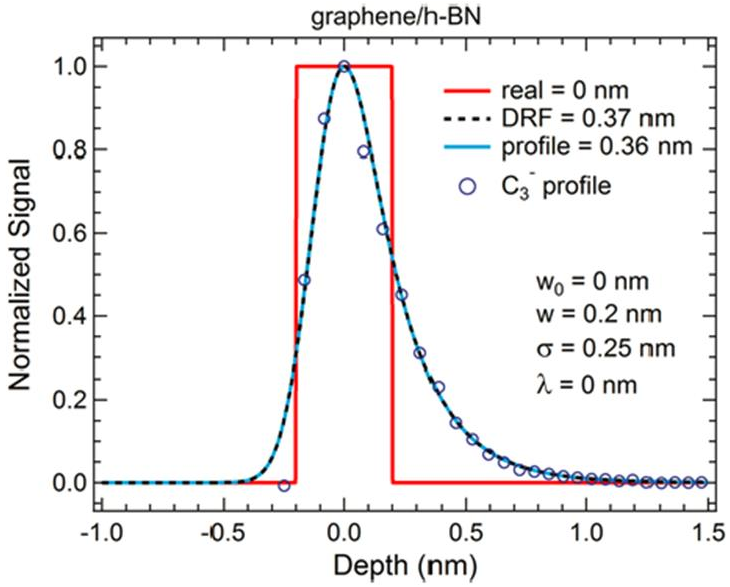

Figure 3.8: MRI model simulated profile for graphene C_3^- for graphene on h-BN vertical heterostructure, showing DRF parameters.[79] Adapted from Reference 79.

A note of caution: atomic mixing and roughness cannot be completely disentangled. Within the MRI model one must clearly define the roughness such that it is completely separated from atomic mixing. In this case, we define the roughness as the RMS roughness given by AFM. The most common technique is to measure the roughness before and after the full depth profile is done through the interface.

The instrument conditions for the depth profile analysis utilized a primary ion beam of Bi^+ ions with a short (18 ns) pulse and high energy (30 keV) with a current of ~3 pA which was rastered over a 100 x 100 μm^2 area. The analysis ion beam was centered within a 250 x 250 μm^2 regressing area that was sputtered by the sputter ion beam (Cs^+ at 500 eV and ~60 nA). The instrument operating pressure was 7.5 x 10^{-10} Torr and the analyzer was biased to collect negative SI.

3.3.3 TOF SIMS Mapping

Figure 3.9 presents a series of secondary ion maps (50 x 50 μm^2) recorded in high lateral resolution (~200 nm) "Burst Align" mode with a Bi_3^+ analysis ion beam, on a separate h-BN flake with CVD graphene on top. These maps are recorded after ~ 0.3 nm of the surface have been removed by Cs^+ sputtering at 500 eV energy and represent the main species of interest related to the graphene overlayer (C_3^-), chemisorbed copper solvent residues (C_2N^- and S^-), PMMA/acetone residues partial underlayer (C_2O^-), chemisorbed adventitious organic material at the h-BN flake surface (CB^-) and SiO_2 substrate (SiO_2^-). Due to intrinsically very low current of the analysis ion beam when using bursting in high lateral resolution mode, Bi_3^+ clusters were preferred instead of Bi_1^+ as analysis ion beam species knowing that polyatomic sputtering increases the secondary ion yield of organic fragments (C_3^-, for example).[116] In this case, bursting was needed to add the high mass resolution capability otherwise unavailable in the high lateral resolution mode. Large defect areas are visible in the C_3^- maps corresponding to graphene patches inherent to the transfer process. The matching lateral localization of the C_3^-, C_2N^-, S^- and C_2O^- secondary ion signals indicate that the solvent residues are uniformly distributed within the graphene overlayer and oxidized organic partial underlayer. In addition, as the depth profiles of C_2N^- and S^- extend over the depth profiles of C_3^- and C_2O^-, as can be seen in Figure 3.6, we conclude that nitrogen and sulfur are most probably chemisorbed in the graphene layer during the copper wet etching process. The CB^- and SiO_2^- maps show the position of the h-BN flake and graphene grain boundaries (i.e., exposed substrate), respectively. As a clear indication of PMMA/acetone marker, the C_2O^- map follows both the C_3^- and SiO_2^- maps, as expected for a solvent that was used after deposition of the PMMA/graphene system onto the h-BN/SiO_2 substrate. Additional contaminants were below the detection limit or their signal was too low to produce a reasonable image, as in the case of Cu^-. Albeit

impossible to spatially map in plane, the copper residue is most probably chemisorbed at the bottom of the graphene layer, as inferred in Figure 3.6, following the transfer process from copper foil.

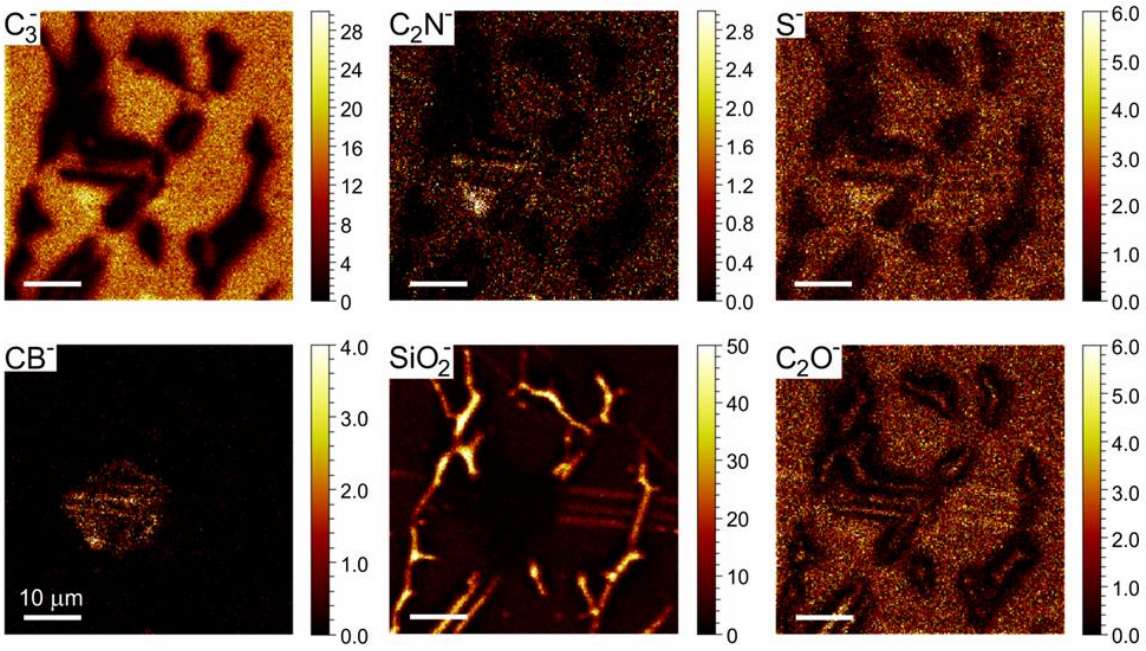

Figure 3.9: Mapping secondary ion analysis taken from the graphene on h-BN heterostructure showing the lateral position of various components both from the 2D materials as well as from contaminants.[79] Adapted from Reference 79.

Given its virtually atomic depth resolution and ultra-high sensitivity, TOF-SIMS depth profiling emerges as an attractive choice for investigating chemical composition at the atomic level of 2D materials synthesized via different methods. All detected interfacial species can be traced back to either the transfer or CVD growth process, thus TOF-SIMS profiling can directly measure the effects of synthesis, handling and fabrication processes on the final 2D materials and heterostructures with large implication in understanding their performance and quality. Consequently, TOF-SIMS can be applied to other layered

structures, providing detailed chemical analysis, as shown in the Supporting Information where a similar 2D heterostructure was characterized.

3.4 GRAPHENE/H-BN AND GRAPHENE/MoS_2 HETEROSTRUCTURES

This characterization technique can be broadly applied to other 2D materials heterostructures. 2D materials heterostructures have been fabricated using different materials and layer numbers and are becoming increasingly complex.[95–98] In order to demonstrate the broad applicability of this technique to 2D materials heterostructures, a sample was prepared with CVD MoS_2 and CVD graphene. The MoS_2 was prepared via CVD with MoO_3 and S by a previously reported process[117]. The CVD graphene was produced with the same method as the graphene and h-BN heterostructure. The graphene was transferred onto the $MoS_2/SiO_2/Si$ substrate with the same previously discussed process as well. This 2D heterostructure was also analyzed with TOF SIMS in the high resolution chemical mapping mode. Figure 3.10 shows the overlaid maps of C_2^-, S^-, and O^- ions after 0 - 4 seconds sputtering and 50 - 54 seconds sputtering.

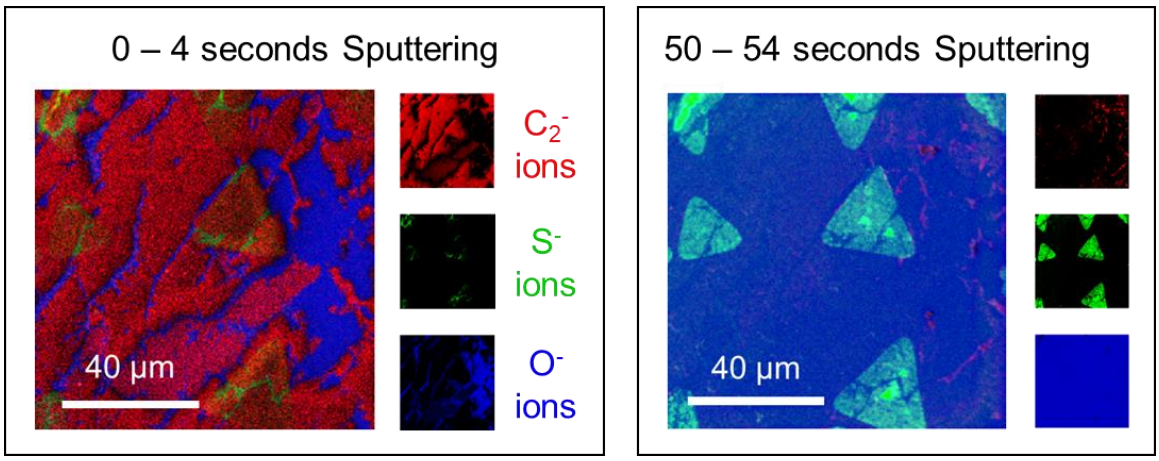

Figure 3.10: Mapping secondary ion analysis taken from the graphene on MoS_2 heterostructure showing that the single-atomic-layer depth resolution is not limited to the graphene on h-BN heterostructure that was investigated in depth.[79] Adapted from Reference 79.

3.5 Transfer Residue Characterization

Copper residue which was remaining with CVD graphene after the transfer process was detected and quantified using the TOF SIMS-based characterization technique and outlined in section 3.3.2. We connect it here to a new work that comparing copper residue remaining with CVD graphene which was transferred by other methods. This project was led by Dr. Seung Ryul Na and Dr. Nassibe Somayyeh Rahimi, who developed a new transfer technique.[118] Copper contamination levels were measured to be several orders of magnitude lower than the values for the more common PMMA-assisted transfer technique. The motivation for the project was to demonstrate other transfer techniques to advance graphene integration into devices and processes. The new transfer technique used graphene grown on copper thin films which were deposited on SiO_2/Si wafers. The graphene was then bonded to a silicon backing layer by an epoxy in a double cantilever beam (DCB) configuration. The strength and range of the adhesive interactions between graphene and copper film and copper and silicon oxide were determined by nonlinear fracture mechanics

concepts. Pulling the two wafer pieces apart transferred the graphene layer. Figure 3.11 illustrates the DCB transfer technique. The copper ion contamination on graphene obtained by the direct delamination method was measured by secondary ion mass spectroscopy (SIMS) and was as low as 10^{10} atom/cm^2, nearly 3 orders of magnitude smaller than what was measured for graphene transferred by wet PMMA-assisted process. This low concentration of copper contamination is crucial for achieving high performance devices.[118]

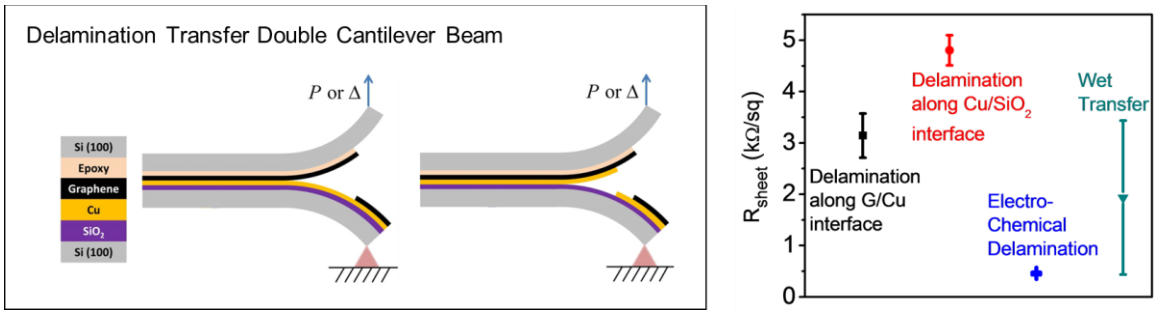

Figure 3.11: Illustration of the delamination transfer mechanics and sheet resistance comparison of graphene transferred by different common transfer methods.[118] Adapted from Reference 118 with permission from The Royal Society of Chemistry.

To investigate the electrical properties of the transferred graphene, two and four-probe devices were fabricated and used for measuring the sheet resistance (R_{Sheet}) of graphene, this was done by collaborators. In the case of the delamination along copper and silicon oxide surface, the copper film was first etched in ammonia persulfate solution diluted with DI water (1:1) and rinsed with DI water subsequently before the fabrication process. Low-power oxygen plasma was used for isolating the graphene channels and Ti/Au (3 nm/ 47 nm) were deposited as the source and drain contacts. Figure 3.11 compares the R_{sheet} of the graphene, obtained by this technique, to the sheet resistance data reported

for graphene transferred by PMMA wet-transfer process and by electrochemical transfer method on flexible substrates.[80] An average sheet resistance of 3 kΩ/sq and 4.7 kΩ/sq was observed for the graphene obtained by direct delamination from copper and from the graphene/copper stack obtained by delamination from the silicon oxide substrate. This is about 1.5 and 2.5 times larger than the value reported for graphene transferred with PMMA layers, respectively. This discrepancy is attributed to the greater graphene roughness caused by the growth process (RMS ~ 70 nm) on the copper thin film. The variation of the sheet resistance of the mechanically-delaminated graphene is ~3 - 5 times smaller compared to the PMMA-assisted technique, suggesting that the transferred monolayer possesses more uniform electrical properties. The reason could be lower levels of contamination caused by the transfer process. To validate this hypothesis, the copper contamination left on graphene during different transfer processes was characterized with TOF SIMS.

The samples were analyzed with a 30 keV Bi^+ analysis ion beam and 1 keV O_2^+ sputtering ion beam. The analysis beam was operated in the high current (HC) bunched mode (100 ns pulse duration) for high sensitivity. The sputter beam was rastered over 350 x 350 μm and the analysis beam over 200 x 200 μm to avoid crater-edge effects in the secondary ions. Positive secondary ions were collected in the analyzer column giving mass resolution better than 5000 (m/δm) for all masses. An electron gun was used to compensate for any charge accumulation in the sample.

The Cu^+ secondary ions collected represent the Cu impurities on the graphene films. By collecting a profile from a reference Cu thin film (e-beam deposited, by the same method as copper used as the substrate for CVD graphene growth), we obtain a reference intensity of Cu^+ counts with a known concentration which can then be compared with the transferred graphene films which have trace Cu contamination by the external reference

standard method.[105] This method gives the concentration of the analyzed sample (C_A) with respect to the reference sample (C_R) by the simple relation

$$\frac{I_A}{I_R} = \frac{C_A}{C_R} \tag{3.10}$$

Where I_A is the intensity of secondary ion signal of the analyzed sample and I_R is the secondary ion signal of the reference sample, and that the signal is from the same ion species (Cu^+ in this case). Here, we make the assumption that the Cu reference surface is the (111) surface, as it is energetically favorable and the closest packed configuration for Cu (thus calculations give a maximum Cu contaminant concentration). Given the Cu^+ depth profiles, the Cu^+ secondary ion signal intensity corresponding to the graphene layer can be fit at the precise depth because that depth corresponds to the maximum C^+ secondary ion signal intensity. The Cu (111) surface gives C_R of 2.21 x 10^{15} at/cm^2 and I_R of 3.4 x 10^4 counts. Figure 3.12 shows the secondary ion maps for Cu^+ from CVD graphene surfaces which have been transferred using different methods. A reference sample SiO_2/Si was also analyzed to determine the background level of Cu^+ signal. The copper content detected on graphene transferred using the common PMMA-assisted technique was high 1.19 x 10^{14} at/cm^2. The copper content detected on graphene transferred using the DCB method was much lower 1.39 x 10^{10} at/cm^2 for the direct delamination piece and 1.30 x 10^{12} at/cm^2 for the graphene/copper stack piece.

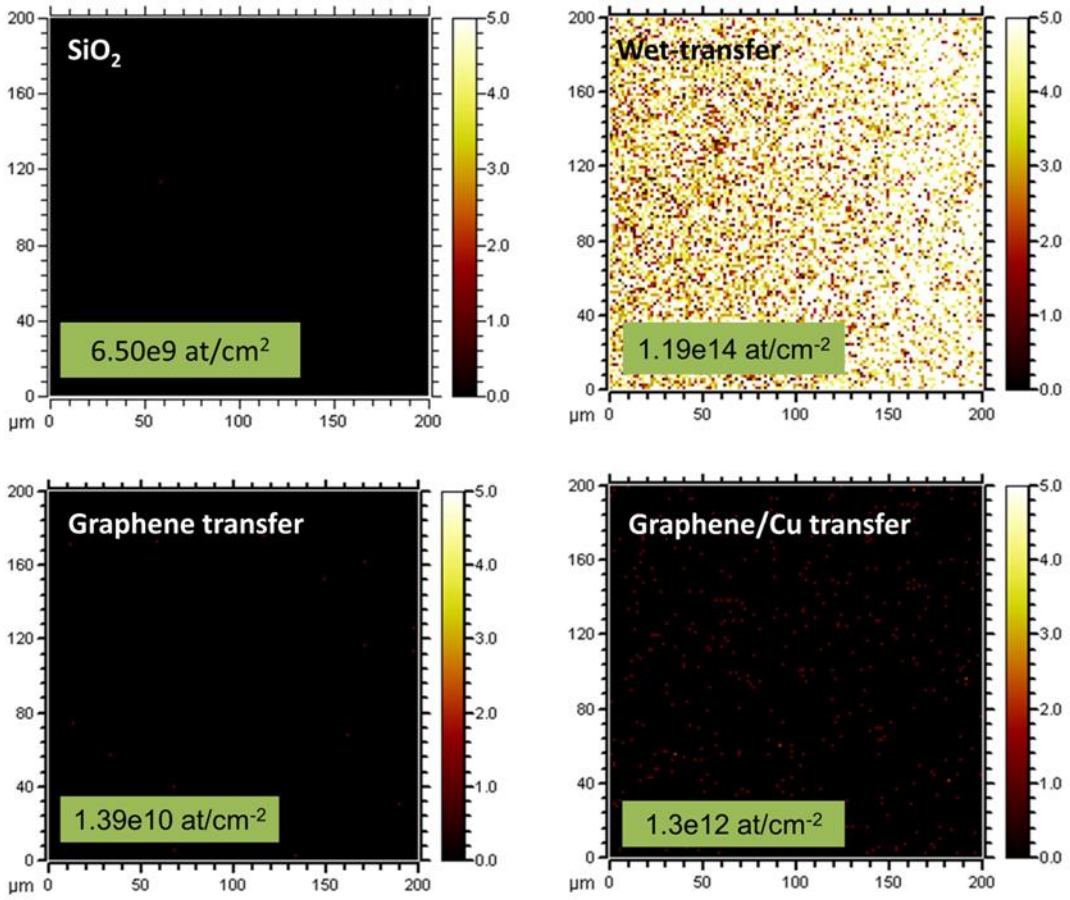

Figure 3.12: Cu^{+} secondary ion maps of transferred graphene samples. Bare SiO_2 substrate analyzed for comparison. Traditional PMMA-supported wet transferred graphene showing very high residual Cu. Bottom left shows direct mechanical delamination graphene with very little residual Cu. Bottom right shows direct mechanical delamination with a Cu bonding layer that is etched away showing some small quantity of residual Cu.[118] Adapted from Reference 118 with permission from The Royal Society of Chemistry.

The results shown in Figure 3.12 show orders of magnitude improvement in copper contamination on graphene transferred by the new DCB technique. This suggests that mechanical delamination results in very low copper contamination on graphene and is nearly comparable to the reference silicon oxide sample. These TOF SIMS results show

the ability for the characterization method to quantify a specific contaminant species relevant for 2D materials down to very low concentration.

3.6 2D Materials Characterization Conclusions

The objective of these 2D materials characterization studies was to demonstrate a new and effective characterization method suited to these unique materials. TOF SIMS, used in conjunction with other characterization methods such as Raman and AFM, is effective in analyzing 2D materials and 2D material heterostructures. It was shown that this characterization could give chemical analysis at very narrow and shallow depths, while also being sensitive to low concentrations.[79,118]

Chapter Four: 2D Materials Device Applications

As was described in chapter 1, the unique properties which have been demonstrated using 2D materials are consequential for a wide range of applications.[23] Devices which take advantage of the dimensionality and confinement within a layer of 2D material, or multiple materials, have shown high performance in electronic and optical applications as well as energy applications.[23,96] Other areas such as structural/mechanical and biomedical fields have also had reports of device applications that utilize 2D materials. The range for 2D materials device applications is continually expanding and increasing in complexity. In this chapter, research will be presented which returns to the relatively simple system of graphene to try and apply its many unique properties for a photovoltaic device.

4.1 Device Applications Introduction

Graphene, whose many unique properties were described in section 1.3, led other 2D materials in device applications in large part because of a relatively simple synthesis processes, as described in section 2.2, which allowed many researchers to experiment with the material. Due to its excellent conductivity at even a few or a single atomic layer, graphene garnered early attention for use in transparent conducting film applications.[25] Optically transparent films are critical for photovoltaic devices. Figure 4.1 shows a schematic of a traditional photovoltaic device and a Schottky junction photovoltaic device, with the transparent conducting film layer as the top film layer.

Work described in this chapter is also published in Reference 133 where I co-led that study with Jaehyun Ahn and designed experiments and performed sample fabrication and characterization. Appropriate citations appear in the text and figures as well.

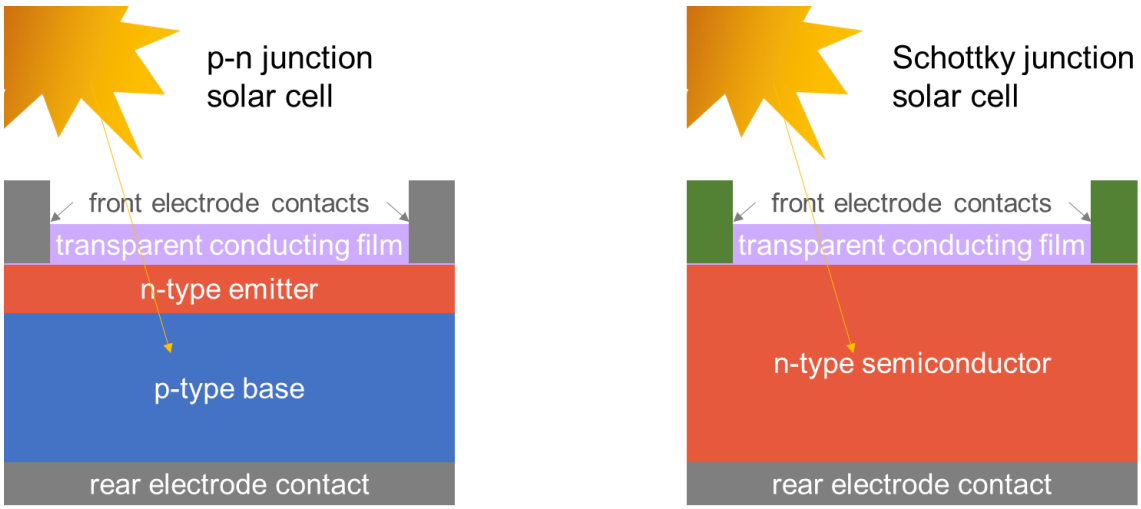

Figure 4.1: Schematic of two solar cell devices, on the left is a traditional p-n junction cell and on the right a Schottky junction solar cell.

The traditional solar cell in Figure 4.1 shows a p-n junction across the bulk semiconductor material. In this case the emitter is n-type doped and the base is p-type doped. The bottom layer is the backside metal contact and the top layer is the transparent conducting film. The top and bottom layers make up the electrodes which take the charges out of the cell. Photons entering the cell from the top are absorbed in the base where excitonic electron-hole pairs are formed. The electrons are moved across the junction to the n-type emitter and the holes are extracted out the bottom contact through the p-type base. In contrast, the Schottky junction solar forms a junction between the semiconductor (its conduction band edge) and the Fermi level of the metal used for the front contact. This gives band bending and charge separation. For the p-n junction solar cell, where the electrodes are connected to an external load voltage V, the current flow is given by

$$J = J_S \left[exp\left(\frac{qV}{kT}\right) - 1 \right] - J_{SC} \qquad (4.1)$$

Where

$$J_S = qN_C N_V exp\left(\frac{-E_g}{kT}\right)\left[\frac{1}{N_A}\sqrt{\frac{D_n}{\tau_n}} + \frac{1}{N_D}\sqrt{\frac{D_p}{\tau_p}}\right] \quad (4.2)$$

$$J_{SC} = qG(L_n + L_p) \quad (4.3)$$

Here J is the current density through the circuit, J_S is the saturation current density, and J_{SC} is the short circuit current density. T is temperature, q is the charge of an electron, k is the Boltzmann constant, N_C (N_V) is the density of states in the conduction (valence) band, D_n (D_p) is the diffusivity of electrons (holes), τ_n (τ_p) is the lifetime of electrons (holes) and N_A (N_D) is the density of acceptors (donors). By reducing the saturation current of the cell, the open circuit voltage (V_{OC}) can be maximized

$$V_{OC} = \frac{kT}{q} ln\left(\frac{J_{SC}}{J_S} + 1\right) \quad (4.4)$$

The short circuit current density (J_{SC}) and open circuit voltage (V_{OC}) are defining figures of merit for a solar cell's performance. These figures of merit relate the solar cell maximum power output (P_{max}) to the fill factor (FF), another important figure of merit

$$FF = \frac{P_{max}}{V_{OC} \cdot J_{SC}} \quad (4.5)$$

$$\eta = \frac{V_{OC} \cdot J_{SC} \cdot FF}{P_{in}} \quad (4.6)$$

Where η is the power conversion efficiency (PCE) and P_{in} is the power incident light on the cell. Improving solar cell performance is a matter of improving one of the figures of merit (J_{SC}, V_{OC}, and FF) or all of them.

The initial effort in building a graphene device was to use the graphene as the transparent conducting layer in a Schottky junction solar cell with a single crystal silicon absorber. Photons pass through the graphene layer and are absorbed by the silicon, where excitons are formed. If the electrons and holes can be efficiently separated by the metal back contact to the silicon and by the graphene, we would have a useful solar cell.

4.2 GS AND GIS SOLAR CELL

The project to demonstrate a graphene and silicon solar cell was undertaken by myself and Jaehyun Ahn. Similar devices have been reported with 2D graphene layers forming a heterojunction with bulk semiconductors such as Si and GaAs, so called graphene-semiconductor Schottky barrier solar cells.[119,120] While early results showed power conversion efficiencies (PCE) of less than 2 %, more recent work has shown up to 15.6 % though various techniques such as graphene doping, insertion of a thin insulator between the graphene and Si, anti-reflective coatings, and semiconductor and backside passivation processes.[121–125]

Another property of graphene is its mechanical strength and flexibility, which contrasts with the rigid single crystal silicon base. However, there is a technique to exfoliate a thin layer of single crystal silicon such that it is mechanically flexible. That technique is described in detail below in section 4.2.2. In this device, the thin Si allows using the mechanical flexibility of graphene. The initial effort yielded a graphene-silicon (GS) flexible cell giving 3.0 % PCE, and more details below. The initial device was also improved with an insulating Al_2O_3 film between the graphene and Si, a graphene-insulator-

semiconductor (GIS) flexible cell, giving 7.8 % PCE. The effects of the Al_2O_3 interlayer are also detailed below. This thin insulator layer, deposited by atomic layer deposition (ALD), increases the overall performance of the device by preventing recombination and increasing charge carrier lifetime.

4.2.1 Thin and Flexible Device Advantages

Graphene has remarkable mechanical properties and flexibility,[1] it is optically transparent (absorbing less than 3% of incident light per layer),[15] and it is highly conductive electrically and thermally.[14] One application for graphene which has garnered early attention is its use as a transparent conducting film.[25,126] For many applications, the current market standard transparent conductor is indium tin oxide (ITO, with sheet resistance of ~ 15 Ω/□) and graphene can provide unique advantages over ITO, namely mechanical flexibility and lower cost with earth abundant materials.[127]

Thin solar cells possess the advantage of reducing the material cost as well as potentially increasing the PCE.[128] Additionally, thin solar cells can be made flexible, which opens a whole new range of applications such as wearable devices.[129,130] Utilizing the inherent flexibility of graphene, GS solar cells fabricated on thinned Si have been demonstrated with efficiencies up to 8.4%.[131,132] These flexible GS solar cells are fabricated on bendable Si films which are produced by wet etching a bulk Si wafer. In this paper, we demonstrate GS solar cells on bendable, thin silicon foils obtained by a kerf-less mechanical exfoliation technique. The exfoliation process does not require the strong etchants of the other processes and the "parent" wafer can be subsequently used to generate additional thin Si films, thus both aspects bolster the effort of reducing material cost.

4.2.2 Device Fabrication

The fabrication of the GS solar cells can be separated into the graphene synthesis, doping and transfer portion, and the silicon exfoliation portion. My experience with 2D materials made it such that my contribution to solar cell fabrication was with the graphene portion and Jaehyun Ahn, based on his extensive experience, contributed to fabrication primarily with the silicon exfoliation portion. We worked in collaboration on process development and device testing and analysis.

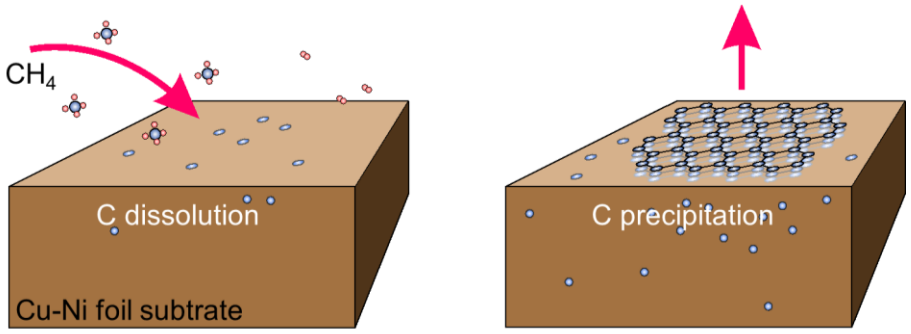

Figure 4.2: MLG growth and analysis, schematic of the dissolution and precipitation mechanism of MLG on Cu-Ni alloy.[133] Adapted from Reference 133 with permission from AIP Publishing.

The multi-layer graphene (MLG) was grown by chemical vapor deposition (CVD) on Cu-Ni alloy foils through an understanding of the growth mechanism on Cu,[10,38] as well as on Ni and Cu-Ni alloy (as discussed in Chapter 2),[48,49] where MLG can be formed by precipitating carbon out during cooling. The dissolution and precipitation process are shown schematically in Figure 4.2. After growth and graphene transfer, the characterization result for the MLG film is also shown in Figure 4.3. The Raman characterization gives a spectrum consistent for MLG and a narrow distribution for the G

band position.[134,135] The AFM scan at the edge of a MLG film shows a step height of ~ 10 nm, which corresponds to 27 – 29 layers of graphene.

After synthesis, the MLG is charge-transfer doped p-type with $AuCl_3$ and the doping effect is verified by sheet resistance and transmission measurement, as shown in Figure 4.3.[136,137] The $AuCl_3$ dopant, applied by spin coating a 10 mM solution of $AuCl_3$ in nitromethane at 2000 rpm for 1 minute, does adversely impact the transmission of the MLG layer. Figure 4.3 shows a trade-off between loss in transmission and a boost in conductivity which arises from additional graphene layers and doping. The doped MLG is then transferred with a PMMA supporting layer and is lifted directly by the target substrate,[68] here the Si foil. The doping was done prior to the transfer for reasons discussed below. The performance tradeoff favors utilizing MLG (as opposed to single layer graphene, SLG) and doping it. Doping the graphene (with $AuCl_3$) reduces the graphene sheet resistance which is measured by van der Pauw method. Un-doped and pre-doped MLG were transferred onto SiO_2/Si bulk substrate followed by metal contact formation using silver paste for measurement. Sheet resistances of 448 and 11 Ω/□ were obtained for un-doped and doped MLG, respectively, with an encapsulating layer of PMMA on top. Like the transfer processes described in chapters 2 and 3, the PMMA film is spin coated onto the graphene at 2000 rpm and baked for 1 min. at 90° C. The PMMA-graphene stack is floated on 0.5 M ammonia persulfate solution to etch away the Cu-Ni alloy substrate. The PMMA-graphene is then rinsed in deionized water to remove any etchant or byproducts from the Cu-Ni removal process. The PMMA-graphene is lifted from the water directly by the target substrate, the silicon foil.

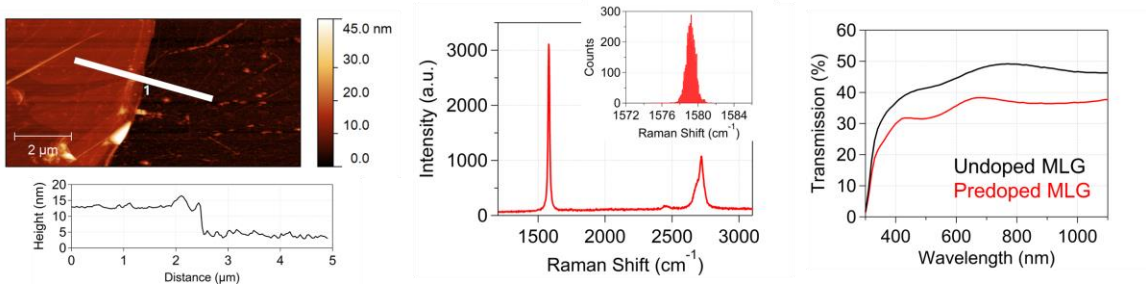

Figure 4.3: MLG analysis. At left, AFM at a transferred MLG film edge showing a step height of ~ 10 nm. The middle shows Raman spectrum and G peak position distribution (inset) showing high quality MLG. At right, transmission of MLG and doped MLG showing significant absorption in the MLG.[133] Adapted from Reference 133 with permission from AIP Publishing.

Figure 4.4 illustrates the kerf-less exfoliation process based on spalling, and resulting exfoliated Si film on metal foil.[138–140] Bulk Si wafers (n-type, <100>, 1 ~ 5 Ω·cm) were covered with a dual-layer of hydrogenated amorphous silicon (α-Si:H) using remote plasma chemical vapor deposition (RPCVD). 5 nm, intrinsic α-Si:H was deposited on the front side to passivate the surface, and 7 nm, n^+ doped α-Si:H was deposited on the back side to achieve ohmic contact with backside metal.[138] A seed layer of Cr (10 nm) and Ni (100 nm) was deposited by electron beam evaporation, followed by electroplating nickel (50 – 55 µm) on to bulk Si. Exfoliation was initiated with a crack at the edge of the wafer after the thermal annealing process and followed by controlled spalling. The exfoliated Si thickness was controlled by the thermal cycling process (270 °C ~ 310 °C, 10 min.) where the difference in coefficient of thermal expansion (CTE) in the different materials induced thermal stress at the metal/Si interface. Si thicknesses down to 8 µm can be successfully exfoliated with surface RMS roughness less than 2 nm. Other parameters such as metal thickness, annealing time, current density during electroplating and the mechanical exfoliation conditions can further control the Si thickness.[141]

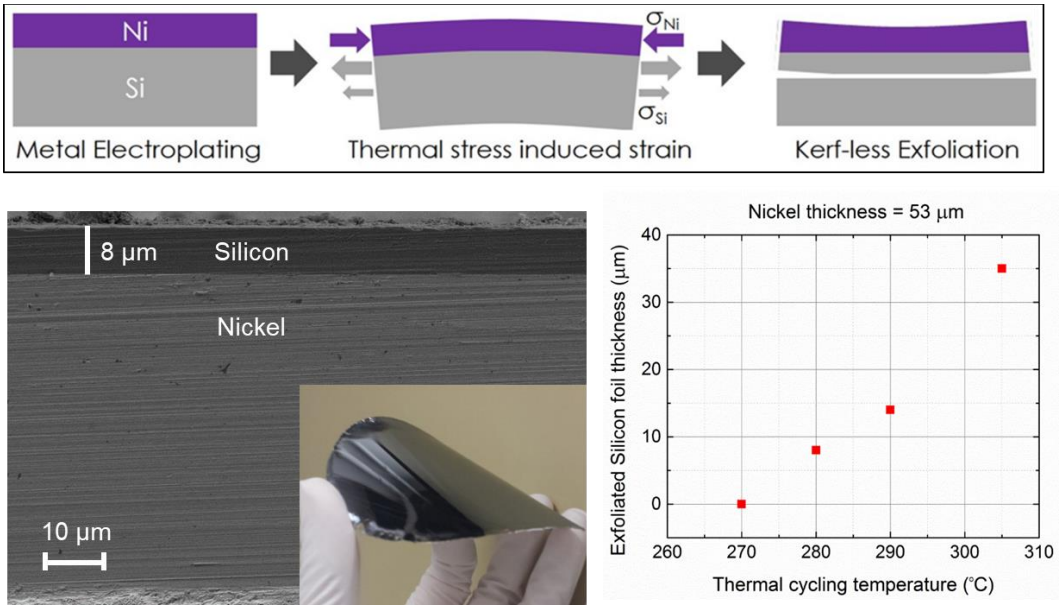

Figure 4.4: Single crystal silicon exfoliation process schematic shown at the top. Bottom left shows SEM cross-section of exfoliated silicon and electroplated nickel. Inset photo of flexible silicon. Bottom right shows trend of exfoliated silicon thickness as a function of thermal cycling temperature.[133] Adapted from Reference 133 with permission from AIP Publishing.

Solar cells fabricated by this method reduce the material cost through re-use of the parent wafer for subsequent exfoliation. This method is also beneficial with respect to handling issues and preventing cracks in thin Si films because of the mechanical support provided by the electroplated Ni layer.

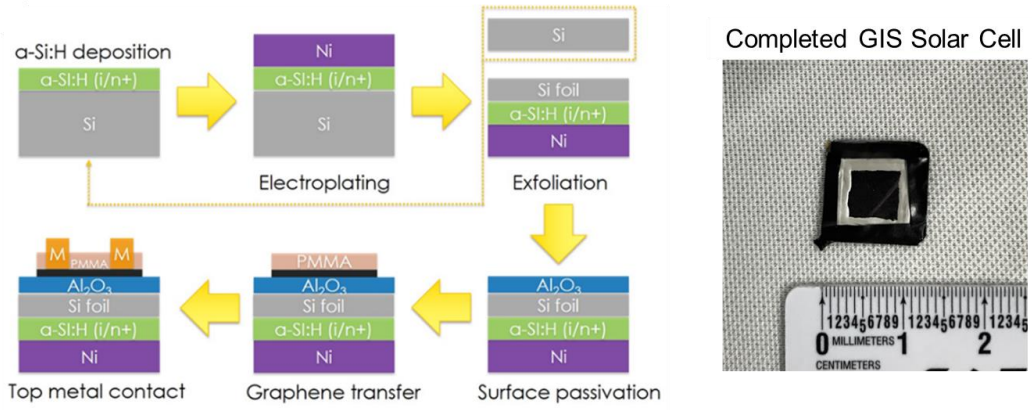

Figure 4.5: Left shows schematic of the GIS solar cell fabrication process. Right shows a photo of the completed device.[133] Adapted from Reference 133 with permission from AIP Publishing.

Figure 4.5 illustrates the GS/GIS solar cell device fabrication and a photograph of the completed solar cell. Si films with thicknesses of 35 μm were used to maximize absorption, while maintaining the flexibility of the film. In the case where an interlayer oxide was inserted (GIS cells), Al_2O_3 was deposited by atomic layer deposition (ALD). To fabricate the GS solar cell (or GIS solar cell), MLG was then transferred onto the Si surface (with or without an intervening Al_2O_3 layer). To aid adhesion and remove wrinkles in the MLG, an additional application of PMMA (spin coated at 3000 rpm for 1 min. and then baked at 90 °C for 1 min) was made on top of the PMMA-graphene.[142,143] It has been previously reported that removing the PMMA after graphene transfer can degrade the graphene quality.[131] To effectively dope the graphene while retaining the graphene quality, the graphene is pre-doped prior to PMMA coating. Silver paste was directly applied onto the PMMA/$AuCl_3$/graphene to form top contact of the graphene. All remaining areas were covered with black tape to ensure precise measurements. The active area of the solar cells is 0.17 ~ 0.37 cm^2.

4.2.3 Device Performance

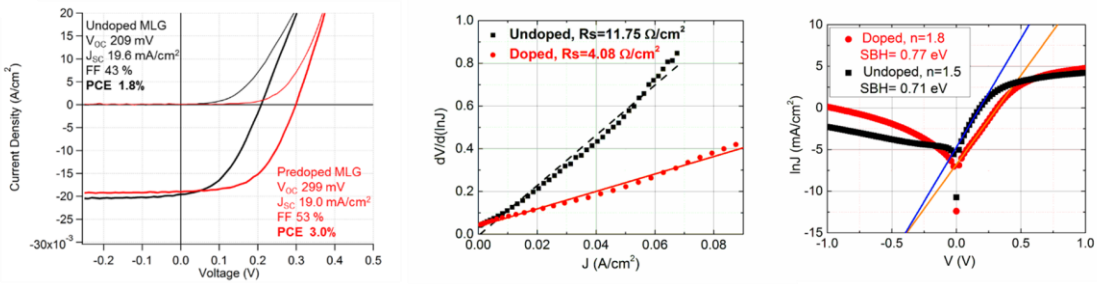

Figure 4.6: GS solar cell comparison between using doped MLG and un-doped MLG. J-V comparison plotted at the left. Middle plot shows *dV/d(lnJ)* for determining series resistance. Right plot shows *ln(J)* as a function of voltage to determine the Schottky barrier height (SBH).[133] Adapted from Reference 133 with permission from AIP Publishing.

Figure 4.6 shows the current density-voltage (J-V) characteristics of un-doped and pre-doped heterojunction MLG GS solar cell on thin exfoliated Si films. Results, from an ABET solar simulator (Model Sun 2000, calibrated with a reference cell ABET model #15150) show that doping the graphene increases open circuit voltage (V_{OC}) from 209 to 299 mV, fill factor (FF) from 43 to 53 % and improving the PCE from 1.8 to 3.0 %. The increase in performance after doping can be explained by analyzing the GS solar cell dark I-V graph and band diagram. Figure 4.7 illustrates the band diagram for un-doped and p-type doped graphene on n-type Si. According to the Schottky-Mott rule of Schottky barrier formation, the Schottky barrier height (ϕ_{SBH}) between the MLG and thin Si film is described based on the work function of the MLG (W_G) and the electron affinity of the Si (χ), thus

$$\phi_{SBH} \sim W_G - \chi \tag{4.7}$$

Doping the graphene with $AuCl_3$ is known to shift the graphene work function (ϕ'_{SBH})[136] and can be extracted from the equation

$$J_S = A^* T^2 exp\left(\frac{-\phi_{SBH}}{kT}\right) \quad (4.8)$$

where J_S is the saturation current extrapolated at V = 0 from the linear portion of the forward current (solid lines in Figure 4.6, un-doped J_S = 8.9 μA/cm^2, doped J_S = 1.14 μA/cm^2), A^* is the Richardson constant (~ 112 A/cm^2·K^2 for n-Si), T is the absolute temperature, q is the electron charge and k is the Boltzmann constant. The Schottky barrier height for un-doped and doped GS solar cells was found to be 0.71 and 0.77 eV, respectively.

The change in saturation current results in a change of V_{OC} given by the following relation,

$$V_{OC} = \frac{nkT}{q} ln\left(\frac{J_{ph}}{J_S}\right) \quad (4.9)$$

where n is the ideality factor of the graphene/Si interface, and J_{ph} is the light-induced photocurrent density of the solar cell.[144] The ideality factor can be extracted by fitting the device response in the dark, giving n of 1.5 and 1.8, respectively, which is shown in Figure 4.6 as well. Following the above equation, an increase in n and decrease in J_S leads to an increase in V_{OC} for doped MLG solar cells. The drop in J_{SC} can be explained due to the decrease in transmitted photons after doping. There is a loss in transmission through the MLG due to $AuCl_3$ charge-transfer doping, which results in a decrease of light reaching the Si absorber as shown in Figure 4.3.

The increase in FF is due to the reduction in series resistance (R_S) after graphene doping. The R_S for un-doped and doped GS solar cells are extracted using the slope of the dV/d(lnJ) plot, which is shown in Figure 4.6 also. The R_S is shown to decrease from 11.75

to 4.08 Ω·cm^2 for doped GS solar cells. Since *FF* is strongly related to R_S, the decrease in R_S gives the increase in *FF*. Overall, the GS solar cell performance is improved from 1.8 % PCE to 3.0 % PCE upon doping with 10 mM $AuCl_3$ in nitromethane.

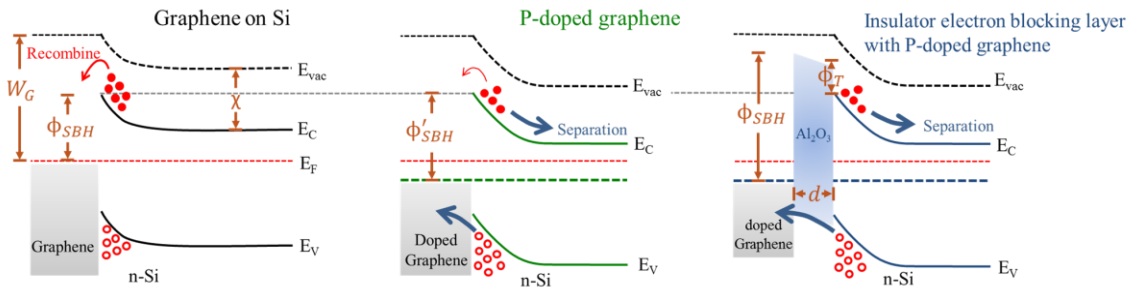

Figure 4.7: Band diagrams comparing solar cell with and without doped graphene and also with interlayer Al_2O_3 dielectric.[133] Adapted from Reference 133 with permission from AIP Publishing.

The next advance to boost cell efficiency, was to include an insulating thin film between the MLG and the Si. A film of Al_2O_3 was deposited between the graphene and Si, forming a graphene-insulator-semiconductor (GIS) cell. Previous studies have shown that materials such as silicon oxide,[125] graphene oxide (GO),[122] and 2-D materials such as hexagonal boron nitride (h-BN)[145] and MoS_2[146] increase the overall efficiencies of GS solar cells. Introducing an inter-layer between graphene and Si were proven to improve the overall performance of GS heterojunction solar cells by blocking carriers from recombining at the interface, reducing the density of interface states, and increasing the carrier lifetime (τ).

Here, we introduce a different inter-layer material, Al_2O_3, which was selected because it has been shown to effectively passivate c-Si by suppressing surface recombination and increase τ.[147–149] To check the passivation quality of our Al_2O_3, a thin layer was deposited on both sides of a cleaned float zone (FZ) n-type Si wafer (1 ~ 5 Ω·cm)

and the carrier lifetime determined by the photoconductance method (Sinton instruments WCT-120). The carrier lifetime before and after deposition was 2 and 27 µs, respectively, with 2 nm of Al_2O_3, which approaches the 33 µs lifetime reported for a cell with a graphene oxide (GO) interlayer.[122]

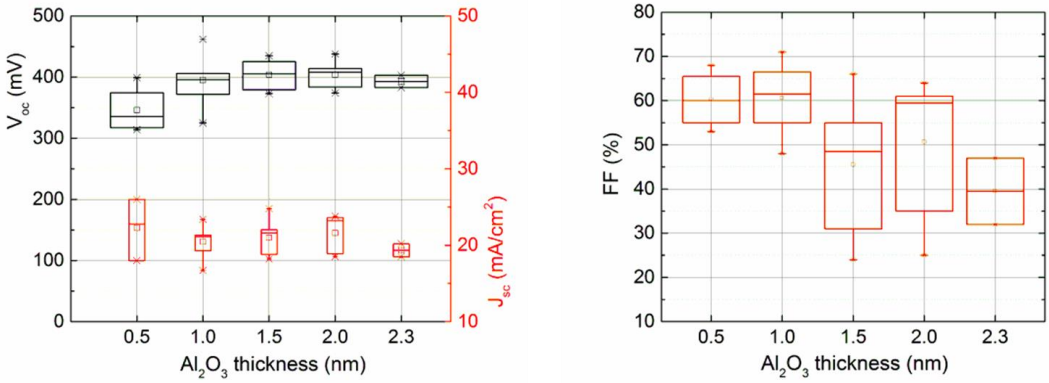

Figure 4.8: GIS solar cell device performance as a function of interlayer Al_2O_3 film thickness. V_{OC} shows a trend of increasing with thickness, and saturating above ~ 1 nm. A competing figure merit is seen with *FF* in the right plot which decreases with increasing thickness.[133] Adapted from Reference 133 with permission from AIP Publishing.

Figure 4.8 compares the V_{OC} and J_{SC} of GIS solar cells on thin Si films with different Al_2O_3 thicknesses. The J_{SC} shows limited variation for the different Al_2O_3 thicknesses, while the V_{OC} increases up to 1 nm Al_2O_3 and then saturates. This increase in V_{OC} upon including the Al_2O_3 layer shows that the interlayer indeed passivates the Si surface of the GIS solar cells.

To extract additional information about the GIS device performance, we consider the diode characteristics. For the case of a device with the metal-insulator-semiconductor (MIS) structure, with the thin insulator material at the interface, the saturation current density J_S is described as

$$J_S = A^* T^2 exp\left(\frac{-\phi_{SBH}}{kT}\right) exp\left(-d\sqrt{\phi_T}\right) \quad (4.10)$$

where ϕ_T is the barrier height presented by Al_2O_3, and d is the Al_2O_3 thickness.[150] Figure 4.7 illustrates the band diagram of the GIS solar cell. While the current density is inverse exponentially proportional to insulator thickness, changing the thickness does not drastically affect J_{SC}, which is consistent with previous publications.[122,125] For our GIS structure with Al_2O_3, while increasing the Al_2O_3 thickness initially increases the V_{OC}, a competing process of photocurrent suppression occurs for thicker Al_2O_3 devices, resulting in V_{OC} saturation. This phenomenon is also consistent with previous studies, such as with Si native oxides.[125] The addition of Al_2O_3 also gives a boost to the *FF* compared with the GS solar cells, as seen in Figure 4.6 and 4.8. This phenomenon may be understood by considering the interaction between MLG and its substrate. ALD deposition of the Al_2O_3 gives a uniform and conformal high-*k* dielectric substrate for the MLG, compared with bare Si, and it is understood to impact the mobility (and R_S) of graphene.[151–153] For the GIS solar cells, enhancement in hole transport in the MLG would lower the device R_S with thin Al_2O_3. As the oxide layer is made thicker, the insulating nature of the layer becomes dominant and an increase in R_S and decrease in *FF* is observed.[125]

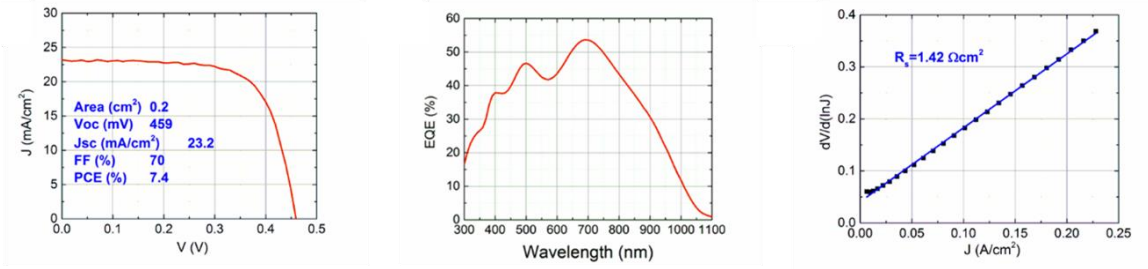

Figure 4.9: J-V and EQE measurements for GIS solar cell, and extracting series resistance R_S.[133] Adapted from Reference 133 with permission from AIP Publishing.

Figure 4.9 shows J-V and external quantum efficiency (EQE) measurements for the optimum GIS device with n and R_S values extracted from dark current. The highest efficiency of the GIS solar cell on exfoliated thin Si film was 7.4 % with an Al_2O_3 interlayer thickness of 1 nm, showing V_{OC} of 459 mV, J_{SC} of 23.2 mA/cm^2 and FF of 70 %. A low R_S leading to high FF, given by controlling the Al_2O_3 thickness, provided the path to optimize the GIS device and maximize efficiency.

Previous GS and GIS devices have been reported to have unstable performance over time. For example, some devices have utilized volatile dopants for the graphene layer which degraded over time[154] or utilized PMMA encapsulation to show stability for a few days.[131] To check the stability of our devices, the optimum GIS sample was initially measured after fabrication and then left in ambient before re-measurement. The temperature and humidity of the facility is maintained at approximately 21 ˚C and 50 %, respectively. The device performance showed < 1 % degradation after 40 days, which is very long stability for a GIS cell. We attribute the increase in stability of these GIS cells to a combination of high quality CVD MLG and ALD AL_2O_3 materials and encapsulation with PMMA.

4.3 GBIS AND GBS SOLAR CELLS

The next advance for solar cell work was to incorporate more 2D materials into the device. Based on enhancements for graphene performance as referenced in chapter 1 and 2, it was natural to try including an h-BN insulator film for different GIS solar cell device structure. There has been no demonstrated GIS solar cell with thin Si and h-BN interlayer, though such solar cells have been made on bulk Si.[145] With the caution about interfacial and surface contamination as shown in chapter 3, several devices were made with the graphene-h-BN-thin silicon structure. GBS solar cells refer to cells with an h-BN interlayer and GBIS solar cells refer to cells with a dual h-BN and Al_2O_3 interlayer.

4.3.1 Device Fabrication

Recall from chapter 3 the difficulty with contamination and residue from transferring CVD-grown 2D materials. To minimize residue stuck between the h-BN and graphene layers of the GBS solar cell, a different approach was taken for transfer. The aim was to limit the amount of processing and possibility of introducing contaminants. Therefore, the transfer of 2D materials was done sequentially, the graphene transparent conducting layer was lifted after Cu-Ni etching and rinsing directly by the h-BN sample (still on its growth substrate of nickel). Figure 4.10 shows a doped MLG on top of CVD h-BN on top of its nickel substrate. After drying and storing overnight in a benchtop vacuum box, another spin coating of PMMA was applied. The nickel substrate from the h-BN was etched away using the method described in section 2.3.2. The PMMA/MLG/h-BN stack (shown in Figure 4.10) was lastly lifted out of the DI water rinse using the bottom thin silicon and nickel foil. From that stage, the solar cell fabrication process was the same as GS and GIS solar cells described in section 4.2. GBIS solar cells were also fabricated where the last lift out was with an ALD Al_2O_3/exfoliated silicon/nickel foil stack. This sequential

transfer avoided having additional PMMA residue between the graphene and h-BN layers as would be the case if the two 2D materials were transferred separately.

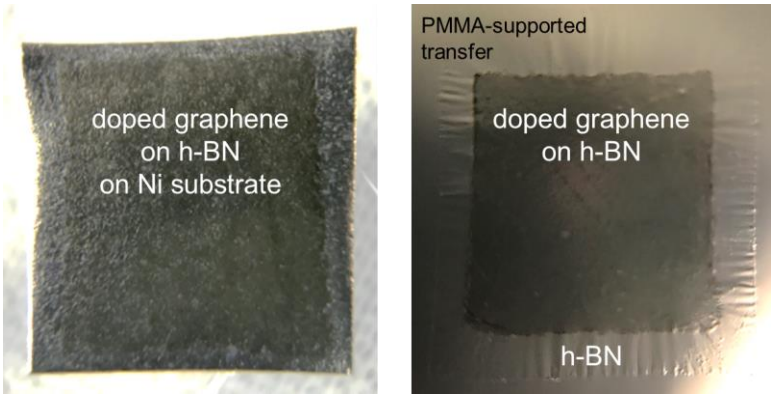

Figure 4.10: Photograph of sequential transfer of 2D materials graphene and h-BN to minimize interfacial contaminants.

4.3.2 Device Performance

Figure 4.11 compares the figures of merit for GBS and GBIS solar cells with GS and GIS cells from section 4.2. The GBS and GBIS solar cells did not perform as well as the GIS. While the results reported in Reference 145 suggest that the GBS device should also show high performance, it is likely that more effective countermeasures are needed to reduce further interfacial contaminants detrimental to the device performance. Increasing the number of interfaces using 2D materials increases the chances of incorporating interfacial contaminants as we saw in chapter 3. In particular, the adsorbed surface contaminants shown on the h-BN flake in Figure 3.7 would likely be present on h-BN handled in ambient. The development of cleaner transfer techniques which are broadly applicable to CVD-grown 2D materials is necessary to achieve improved performance. Reference 145 showed improved solar cell performance using a graphene/h-BN heterostructure which was sequentially grown, and thus not needing an extra transfer step.

Also adding interlayers for the GIS-type solar cell gradually increases the R_S of the device and degrades its overall performance as was seen in section 4.2.3. It is supposed that this effect also contributed to the relatively weak performance of the GBS and GBIS solar cell devices.

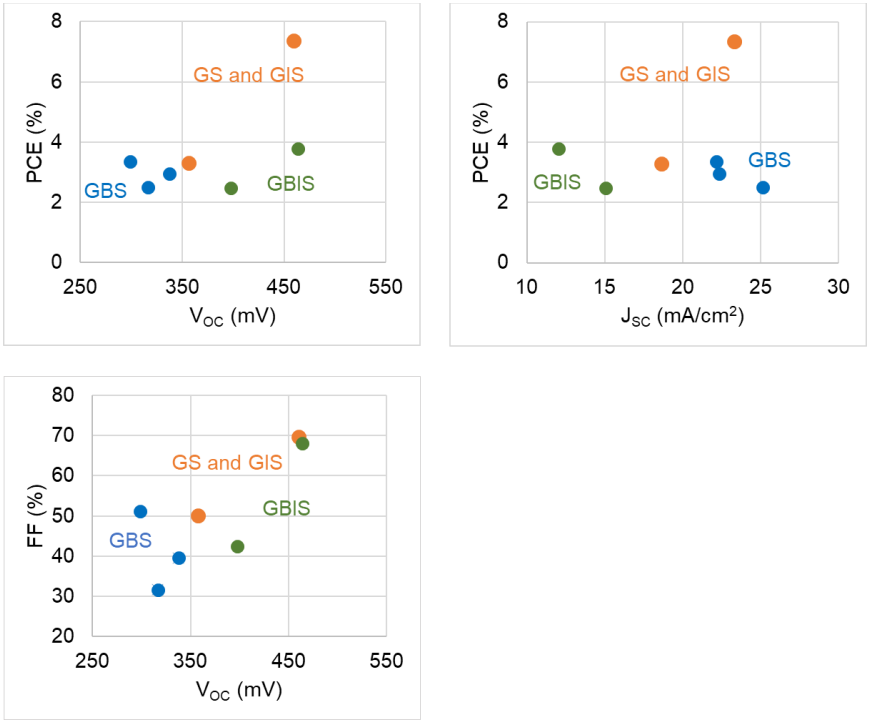

Figure 4.11: Figures of merit plotted for solar cells with h-BN interlayer integrated, GBS solar cells having h-BN as the only insulator and GBIS solar cells having h-BN and Al_2O_3 interlayer. The performance did not exceed the performance of the best GIS solar cell.

4.4 Suggested Future Device Work

A lesson learned from chapter 3 is also evident in the device research described here in chapter 4, that optimized performance depends on optimal and uncontaminated materials and interfaces. It is likely that higher performance flexible solar cells could be fabricated with cleaner transfer techniques and also optimizing layer thicknesses, as was

done for the Al_2O_3 I-layer in section 4.2.3. For one layer thickness, the MLG thickness, the solar cells had relatively thick films and the transmission measurements (Figure 4.3) showed that a considerable amount of incident light is absorbed in the graphene layer. Work by collaborators earlier here at the University of Texas at Austin showed growth temperature as an effective method for achieving layer control.[48] A thinner MLG film would increase incident light and boost efficiency. Another obvious layer thickness control is the h-BN layer. As was the case for Al_2O_3, a similar thickness optimization should be done for an h-BN I-layer. It is also considered remaining work to do a complete dielectric performance measurement of the synthetic h-BN. Dr. Sushant Sonde reported dielectric breakdown (and also graphene mobility on top of) h-BN grown with diborane and ammonia precursors.[55] An informative next test for integrating h-BN as a dielectric for 2D materials devices would be to create 2D material devices with h-BN substrates and gate dielectrics. Others have reported encouraging results in this regard,[155,156] but it will be useful to understand distinctions in performance based on materials synthesized with different processes. For example, the grain size of the growth substrate (or its orientation) affecting the grains of h-BN and defect density.

4.5 2D Materials Devices Conclusions

Demonstrations of lightweight and flexible solar cells which incorporate multi-layer graphene as a transparent conducting film are discussed here. Work was also done to incorporate h-BN insulating layers to try and improve the solar cell performance, with mixed results. The lessons from the earlier chapter 3 are re-learned in device applications, that clean interfaces are a critical challenge facing large area synthetic 2D materials.

Chapter Five: Conclusion

The conclusions written here are reiterated from the conclusion sections for each of the above chapters 2, 3, and 4. There are minor edits made for readability. The purpose of this section is to have one section where a future researcher may find conclusions and suggestions for continuing work in a single location.

5.1 Synthesis Conclusions

The objective of the 2D materials synthesis work was to better understand the mechanisms during CVD for graphene and h-BN. The methods which have been used include characterization methods (SIMS and XPS) and analysis of thermodynamic driving forces. The characterization results provide evidence that furthers the understanding of graphene and h-BN CVD synthesis mechanisms, and the thermodynamic analysis suggests a specific CVD synthesis mechanism for h-BN which is backed up by characterization evidence. The growth mechanism has multiple of forces acting on it, in competition, and many of those are outlined in chapter 2. For graphene synthesis, kinetic control was shown in comparing Cu and Ni substrate growth in sections 2.2.1 and 2.2.3 and 2.2.4. We showed energetic control with oxygen in growth in section 2.2.2. For h-BN synthesis, kinetic control was shown in B and N diffusion on single crystal substrates in section 2.3.6. We showed energetic control by carbon dosing in section 2.3.4 and also observed an energetic phenomenon in section 2.3.3.

The question about the competing forces acting on the growth mechanism remains to be disentangled, particularly for h-BN CVD synthesis as seen in section 2.3.6. One area of focus that may prove fruitful is to work on nucleation and layer-by-layer growth of h-BN domains. The work around nucleation and adlayer growth with graphene CVD

synthesis in section 2.2 has not been done for h-BN and well-executed experiments would clarify the growth mechanism significantly.

5.2 Characterization Conclusions

The objective of the 2D materials characterization studies was to demonstrate a new and effective characterization method suited to these unique materials. TOF SIMS, used in conjunction with other characterization methods such as Raman and AFM, is effective in analyzing 2D materials and 2D material heterostructures. It was shown that this characterization could give chemical analysis at very narrow and shallow depths, while also being sensitive to low concentrations.[79,118]

Combining the methods detailed in chapter 3 with devices like those in chapter 4 is the logical next work to focus on. The results shown here characterized structures but not functional devices, or characterized materials that were later incorporated into devices. Comparing the interlayer contamination, for example, between a functioning and non-functioning 2D material heterostructure device would be of great interest to those working with these materials.

5.3 Device Applications Conclusions

The 2D materials devices here demonstrated lightweight and flexible solar cells which incorporated multi-layer graphene as a transparent conducting layer. Work was also done to incorporate h-BN insulating layers to try and improve the solar cell performance, with mixed results. The lessons from chapter 3 are re-learned in device applications; that clean interfaces are a critical challenge facing large area synthetic 2D materials.

A lesson learned from chapter 3 is also evident in the device research described in chapter 4, that optimized performance depends on optimal and uncontaminated materials

and interfaces. It is likely that higher performance flexible solar cells could be fabricated with cleaner transfer techniques and also optimizing layer thicknesses, as was done for the Al_2O_3 I-layer in section 4.2.3. For example, the MLG thickness (the solar cells had relatively thick films) and the transmission measurements (Figure 4.3) showed that a considerable amount of incident light is absorbed in the graphene layer. Work by collaborators earlier here at the University of Texas at Austin showed growth temperature was an effective method for achieving layer control.[48] A thinner MLG film would increase incident light and boost efficiency. Another obvious layer thickness control is the h-BN layer. As was the case for Al_2O_3, a similar thickness optimization should be done for an h-BN I-layer. It is also considered remaining work to do a complete dielectric performance measurement of the synthetic h-BN. Dr. Sushant Sonde reported dielectric breakdown (and also graphene mobility on top of) h-BN grown with diborane and ammonia precursors.[55] An informative next test for integrating h-BN as a dielectric for 2D materials devices would be to create 2D material devices with h-BN substrates and gate dielectrics. Others have reported encouraging results in this regard,[155,156] but it will be useful to understand distinctions in performance based on materials synthesized with different processes. For example, the grain size of the growth substrate (or its orientation) affecting the grains of h-BN and defect density.

Appendix: Four-inch CVD System Operation

A.1 Introduction

This section describes the CVD system and its operation. The system is currently located in the 2.406 lab at the Microelectronics Research Center. Concepts about the growth process and mechanism are described in detail in Chapter 2. The system is a larger scale hot wall CVD growth system used for graphene growth on Cu and Ni substrates. This system has unique capabilities and constraints compared with the benchtop tube furnaces. Control of various components of the system are made through a LabView program. The system logs several process parameters and has a residual gas analyzer (RGA) attachment. The system was originally designed and built by Dr. Carl Magnuson with Nishant Jayant and Claire Spradling. The system was deconstructed, moved, and rebuilt by myself in 2014. Much thanks is given to the facilities staff, particularly James Hitzfelder, Darren Robbins, and Jesse James, for their support and hard work during the move and rebuild.

A.2 System Parts

The furnace and growth chamber portions of the system are shown in Figure A.1 and components are grouped by function. The furnace is marked by orange at (1) and the power supply and controller for the furnace is (1a). In the center of the furnace is the quartz tube. The flanges at the end of the tube are steel conflat bolted to the other steel components of the vacuum system. The steel components are sealed with copper rings which are replaced any time a connection is opened and bolted together again. The quartz tube and steel flange are bonded by JB Weld and TorrSeal. The quartz tube (and steel flanges) should be replaced when copper deposition in the interior of the tube is excessive to the point of flaking off or if the tube becomes otherwise contaminated. Cooling water lines and brass plate heat shields keep the flanges cool so they do not leak during heating. Automatically

controlled valves are indicated in light blue, (1) is the “Loadlock” valve, (2) is the “Roughing” valve, and (3) is the “Turbo” valve. These are controlled through the LabView program. Manually controlled valves are indicated in dark blue, (1) is the argon leak valve, (2) is the precursor gases leak valve, (3) is the manual loadlock valve, and (4) are the RGA leak valves. System and process monitoring components are marked in dark green, (1) are the pressure gauges and (2) is the residual gas analyzer (RGA). Vacuum pumps are marked in grey, (1) is the turbo pump backing roughing pump, (2) is the roughing pump, and (3) is the turbo pump. System control terminals are marked in light green, (1) is the PC control which has the LabView program and (2) is the turbo pump controller.

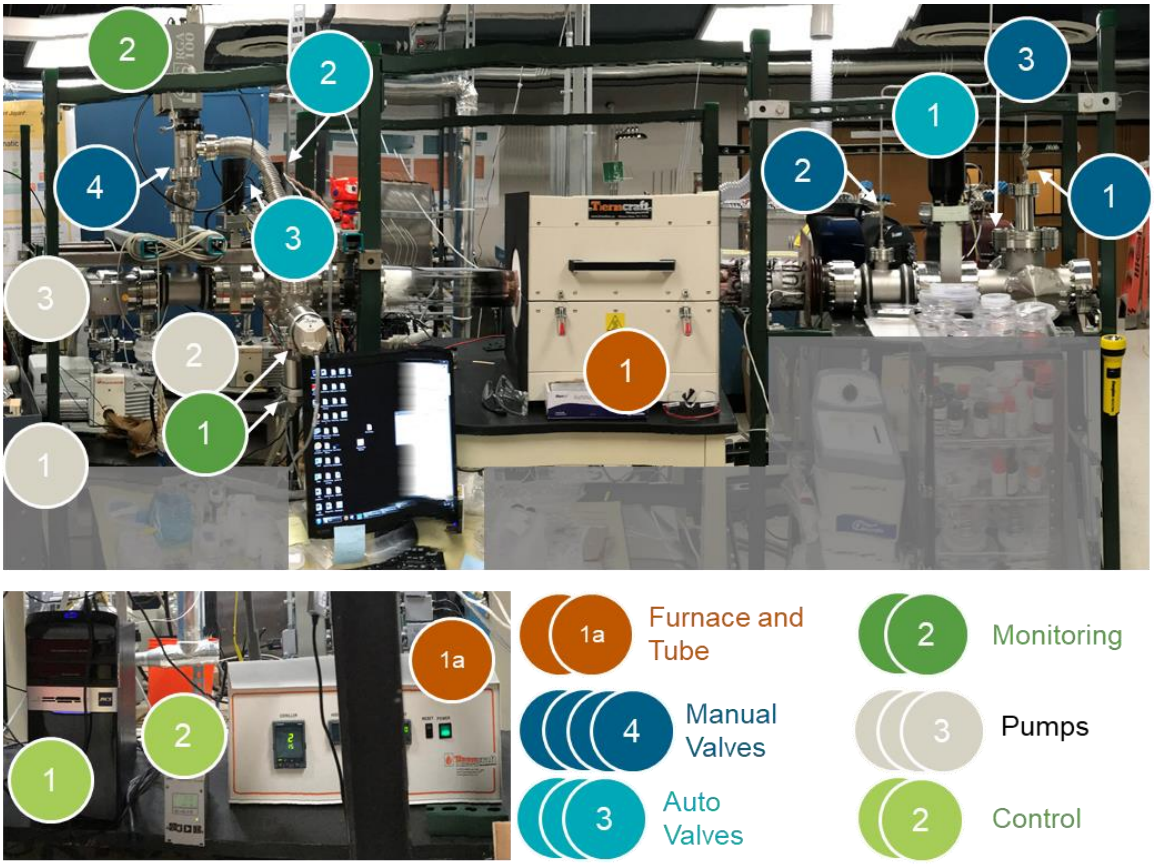

Figure A.1: Photograph of the four-inch CVD growth system. Different components are labeled and grouped.

The gas cabinet, mass flow controller (MFC) bank, and MFC control switch board are shown in Figure A.2. The gas cabinet enables gas monitoring for safety purposes. The MFCs are all controlled via the LabView program and are each connected to the switch board which is connected to the PC. Each MFC also has a manual leak valve which must be opened if that gas line is to be used in the recipe. Each gas line also has a manual leak valve for a bypass line for purging gas lines. There is a safety shut-off valve downstream of the MFCs which is triggered if the PC detects that system pressure is rising to approach atmosphere.

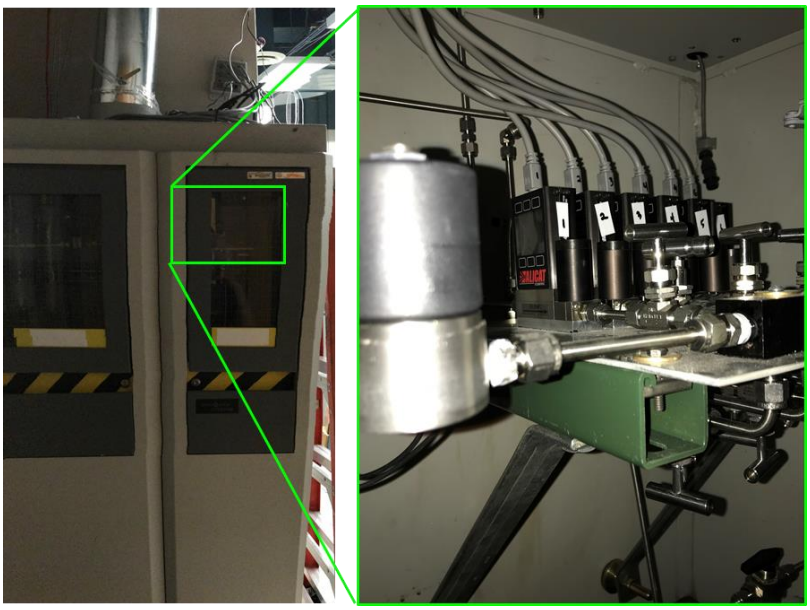

Figure A.2: Photographs of the gas cabinet and mass flow controller bank portions of the four-inch CVD growth system.

A.3 Control Terminal

The CVDSystemMonitor.vi is the LabView program for controlling the four-inch CVD system. From the bottom of the window, shown in Figure A.3, the mass spectrum from the RGA is shown. The mass range is from 1 – 100 amu and continually refreshing. The spectra are stored on the hard disk drive of the PC. In the center above the RGA mass spectrum are the "Start RGA" button and the RGA Total Pressure monitoring. The "Start RGA" button will turn green when the RGA is collecting mass spectra. The Total Pressure will update with the pressure reading every time a full spectrum is collected and the displayed units are torr. Directly above these two is the "STOP" button which will stop the LabView program. On the right side are the flange temperature monitoring, which are connected to a thermocouple touching the flange. To the left side are three toggle switches for controlling the automatic valves. Each toggle switch has its corresponding valve labeled above it; "LoadLock", "Roughing", and "Turbo". The "Turbo" valve cannot be opened if

the system pressure is above 20 mtorr. Proceeding up the window, the large dial on the left side is the System Pressure in torr. The grey box in the dial displays the pressure as well which is useful for mtorr pressure range. The white field is for the butterfly valve to the "Roughing" valve. The gas flow through the system can be attenuated by closing the butterfly valve, the value "0" is fully open and value "100" is fully closed. However, even with the butterfly valve fully closed, the pumps will still maintain vacuum and gas will still flow by the butterfly valve. Above and to the left of the pressure dial shows the monitoring lag of the "Pressure Lag" and to the right is the monitoring lag of the "Furnace Lag". To the right of the pressure dial are the Furnace Temperature and Furnace Power meters. The Furnace Temperature bar and grey box read out the current temperature in the furnace. The white field at the top of the Furnace Temperature meter allows the user to manually enter the desired temperature setpoint. The Furnace Power meter at the right displays the power consumption of the furnace in real-time. Above, and near the top of the CVDSystemMonitor.vi, are six meters for each individual MFC. The white box in the lower left allows the user to manually input a flow rate and the grey box in the lower right displays the real-time flow through the MFC. The gas line connected for each meter is written above that meter. Above and to the right shows a grey box that displays the monitoring lag of the "MFC Lag". At the upper right corner of the window is the "Load Input File" button which allows the user to load and run a recipe using the LabView program.

Recipes for the four-inch CVD system are simple tab-deliminted text files. As shown in Figure A.3, each recipe step is a row and each column is a process parameter. The first column value is the step time in seconds. The second column value is the furnace temperature setpoint. The third column value is the butterfly valve position. The fourth through ninth column values are the MFC flow setpoint for the respective MFC. In order

matching the LabView program MFC meter order, hydrogen (H2 flow), methane (CH4 flow), ^{13}C-enriched methane (13CH4 flow), argon (Ar flow), dilute oxygen in argon (Dilute O2 flow), and dilute ^{13}C-enriched methane is hydrogen (Dilute 13CH4 flow).

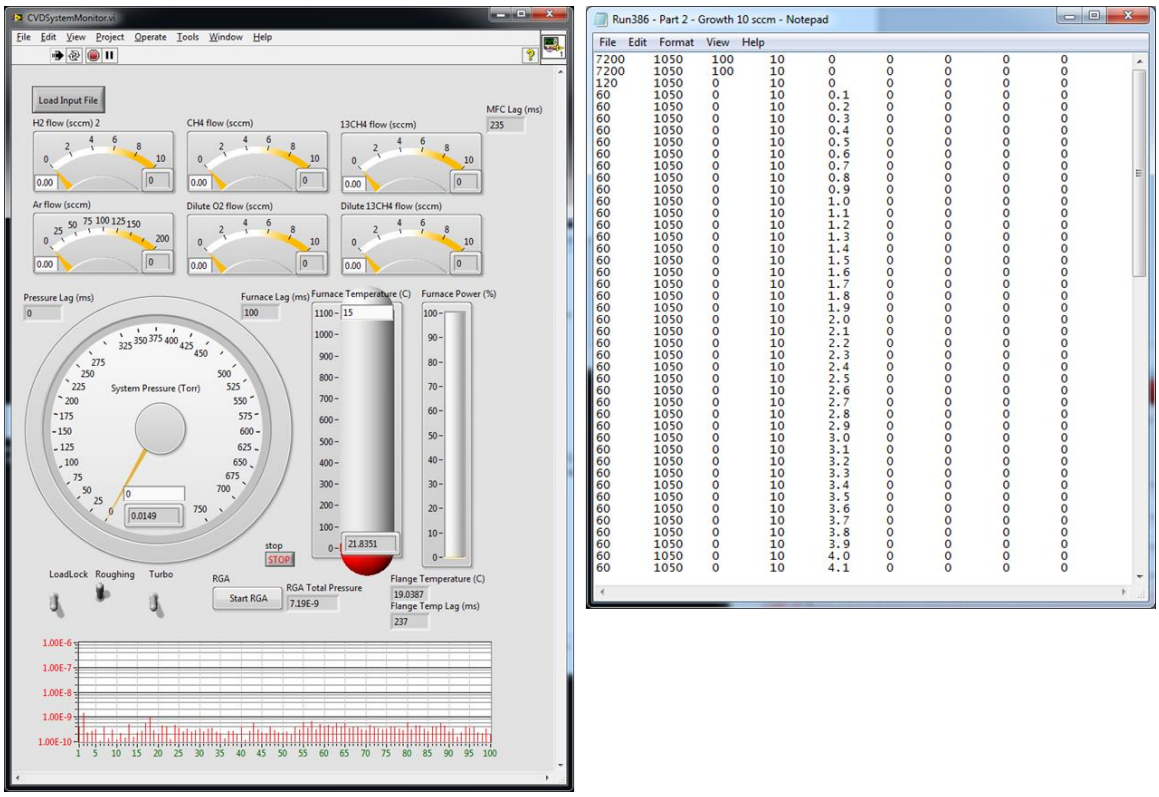

Figure A.3: Screen captures of the LabView program CVDSystemMonitor.vi and an example growth recipe.

Logged system parameters are stored on the local hard disk drive as DAT files (.dat extension) with the date and time as the file name. They are separated into two types of files, “CVD” DAT files and “RGA” DAT files. “CVD” log files contain information about the furnace temperature, gas flow rates, flange temperature, and main chamber pressure. “RGA” log files, as the name suggests, contain information about the RGA mass spectra as well as RGA pressure. There are MATLAB programs also stored on the PC which can

quickly plot useful process parameters over time, “plot_CVD_and_RGA_data.m” and “plot_CVD_data.m”. The user may plot some gas species as measured by the RGA over a growth run and the logged process parameters with the MATLAB program will give that information.

A.4 Running a Process Recipe

The standby state for the system is to be under vacuum, pumping through the “Roughing” valve. To vent the system, close the “Roughing” valve and open the “Loadlock” valve (the “Turbo” valve should be and remain closed). The pressure will likely gradually rise or will remain static if there are no leaks in the system. Loosen the latch at the loadlock door and open the leak valve from the argon line. The pressure will rise to atmosphere as the system fills with argon. At this time, the top of the furnace should be opened and propped open to observe the position of the substrate and carrier. When the pressure equilibrates with ambient, the leak valve from the argon line can be shut. Place the growth substrate onto a quartz boat carrier. Push the substrate and carrier into the center of the furnace in the quartz tube. Take care when pushing over the valves so that the substrate does not slip off the carrier. Withdraw the pipe used to push the substrate and carrier and shut and latch the loadlock door. Open the manual valve to pump out the system through the loadlock side. When the pressure drops below 30 mtorr (typically less than 10 minutes), shut the “Loadlock” valve and shut the manual valve. Open the “Roughing” valve.

Now the substrate is loaded and the system is back under vacuum. The next process is to preheat the substrate and pump down to base pressure and drive off any moisture and adsorbed water. First start the RGA (“Start RGA” button seen in Figure A.3) and note the turbo pump pressure, which should be in the 10^{-8} to 10^{-9} torr range. Shut and latch the

furnace lid and set the temperature to 200°C. Open the "Turbo" valve (the LabView program will automatically shut the "Roughing" valve). The furnace will overshoot temperatures below ~ 400°C, but so long as the pressure remains below a few mtorr it will not cause issues with the substrate. If the pressure during the preheat process does reach the mtorr range, it is an indication that there is a significant leak in the system. The pressure during the preheat process should drop to 10^{-6} torr range. At the end of the preheat process, shut the "Turbo" valve and open the "Roughing" valve.

The next process is to begin RGA monitoring of the main chamber gases and to load the growth recipe. The RGA should still be logging mass spectra from the prior preheat process and now showing the turbo chamber pressure to be again in the 10^{-8} range. There are two valves to open to leak in gas from the main chamber into the turbo chamber where the RGA is connected. Fully open the larger manual valve and then turn the leak valve 1.5 turns counter-clockwise (dark blue (4) in Figure A.1). When gas from the main chamber is leaking through properly, the pressure detected by the RGA will increase to the 10^{-7} range with noted increase in the N_2 (28 amu) species. Next open the leak valve connected to the inlet gases line and then open the associated leak valves at the MFC panel in the gas cabinet (Figure A.2). For a typical graphene growth, this will be 1 and 2 for hydrogen and methane.

At this point, the furnace temperature is around 200°C and the main chamber pressure is in the mtorr range. The RGA is continually logging spectra from the main chamber gas composition. It is now ready to load a growth recipe with the "Load Input File" button seen in Figure A.3. Once the desired file is selected, the LabView program will automatically follow each recipe step and adjust gas flow and furnace temperature. A typical growth run takes several hours to complete. Heating the furnace to 1000°C takes ~ 1 hour, while cooling from 1000°C takes 8 – 10 hours. Due to the extreme slow cooling

limitation of this system, growth recipes which continually flow precursor as well as hydrogen during cooling are preferred.

Once the growth recipe has completed, the user should manually shut gas flows and furnace heating if appropriate. This is done by manually entering desired setpoints into the appropriate fields, for example set “0” into all MFC meter fields and set “15” into the furnace temperature field. The user should also shut the leak valves to the RGA and turn off RGA monitoring through the LabView program (allow a few spectra to run after closing leak valves to ensure that the turbo pumped chamber is well-sealed). Note also the butterfly valve position after the recipe has been completed, pumping speed may be slow unless the butterfly valve is fully open (set to “0”).

To extract the carrier and sample, the loading procedure can be followed. For safety reasons, the automatic valves cannot be opened if the furnace temperature is above 100°C. Before this, manually close the gas line leak valves and the gas inlet leak valve. With the furnace cooled below 100°C and propped open and all inlet lines shut, the loading procedure can be followed. First shut the “Roughing” valve, then open the “Loadlock” valve, then unlatch the loadlock door and open the manual argon leak valve. Once the system has pressurized, the loadlock door can be opened and the pipe can be used to pull out the carrier and sample. After the sample has been retrieved, the loadlock door should be shut and latched and then the system should be pumped back to vacuum. First this should be done through the manual loadlock valve.

A.5 System Power Down and Maintenance

In the event of facilities maintenance, for example process cooling water shut off, the four-inch CVD system should be fully powered off to prevent damage to components or other unexpected issues. The most sensitive equipment in this regard are the RGA and

the turbo pump. Other components can be simply powered off by power toggle switches or powering off power strips. The RGA and turbo pump power off process and start up process are described below.

To power off the RGA, first stop any monitoring as controlled through the LabView program. The RGA should not be monitoring gases and pressure until a recipe is running. The power off toggle switch is on top of the RGA box shown as dark green (2) in Figure A.1. To power off the turbo pump, check the turbo pump controller seen at light green (2) in Figure A.1. Press the power button on the front of the turbo pump controller and watch as the rotation speed decreases gradually to zero. Once the turbo has stopped rotating the toggle switch on the back of the turbo pump controller can be switched off.

The power on procedure for both components is the inverse of the power off procedure. For the RGA, switch on the toggle switch and wait for the RGA power LED light to come on and stabilize. For the turbo pump, turn on the toggle switch at the back of the turbo pump controller. After starting up, the green LED on the turbo pump will flash. Select the display on the turbo pump controller to display the rotation speed (typically set for 1000 rpm). When the green LED is flashing, the power button on the front of the turbo pump controller can be pressed and the rotation speed will increase from zero to the setpoint value. When the turbo speed has reached the setpoint and no errors are detected, the greed LED will be steady and illuminated.

Maintaining the system is limited to changing the tube when it has too much copper deposition or if it has become contaminated. This was described briefly in section A.2. In addition to bonding the quartz tube to steel flanges, the user is advised to ensure the bond is fully dry (usually left for a few days) before installing. Besides bolting the new tube in place and replacing the copper rings, the user should take care to remove/replace the cooling water lines (and thermal grease) and brass heat shields. The work of replacing a

tube requires at least two people. Another routine maintenance is to change the pump oil for each of the wet pumps. Pump oil can be drained at the bottom of the pump and refilled at the indicated port on the top. The pump oil should be changed quarterly if the system is used often. Be sure to power off pumps (including turbo pump) when changing oil.

References

1. C. Lee, X. Wei, J. W. Kysar, and J. Hone: Measurement of the Elastic Properties and Intrinsic Strength of Monolayer Graphene. *Science (80-.).* **321**(5887), 385 (2008).
2. K. I. Bolotin, K. J. Sikes, Z. Jiang, M. Klima, G. Fudenberg, J. Hone, P. Kim, and H. L. Stormer: Ultrahigh electron mobility in suspended graphene. *Solid State Commun.* **146**(9–10), 351 (2008).
3. G. Fiori, F. Bonaccorso, G. Iannaccone, T. Palacios, D. Neumaier, A. Seabaugh, S. K. Banerjee, and L. Colombo: Electronics based on two-dimensional materials. *Nat. Nanotechnol.* **9**(10), 768 (2014).
4. K. S. Novoselov, A. K. Geim, S. V Morozov, D. Jiang, Y. Zhang, S. V Dubonos, I. V Grigorieva, and A. A. Firsov: Electric field effect in atomically thin carbon films. *Science* **306**(5696), 666 (2004).
5. A. K. Geim and K. S. Novoselov: The rise of graphene. *Nat. Mater.* **6**(3), 183 (2007).
6. D. R. Dreyer, S. Park, C. W. Bielawski, and R. S. Ruoff: The chemistry of graphene oxide. *Chem. Soc. Rev.* **39**(1), 228 (2010).
7. M. S. Dresselhaus and G. Dresselhaus: Intercalation compounds of graphite. *Adv. Phys.* **51**(1), 1 (2002).
8. H. Shioyama: Cleavage of graphite to graphene. *J. Mater. Sci. Lett.* **20**(6), 499 (2001).
9. C. Berger, Z. Song, T. Li, X. Li, A. Y. Ogbazghi, R. Feng, Z. Dai, A. N. Marchenkov, E. H. Conrad, and P. N. First: Ultrathin epitaxial graphite: 2D electron gas properties and a route toward graphene-based nanoelectronics. *J. Phys. Chem. B* **108**(52), 19912 (2004).
10. X. Li, W. Cai, J. An, S. Kim, J. Nah, D. Yang, R. Piner, A. Velamakanni, I. Jung, E. Tutuc, S. K. Banerjee, L. Colombo, and R. S. Ruoff: Large-area synthesis of high-quality and uniform graphene films on copper foils. *Science* **324**(5932), 1312 (2009).
11. G. R. Bhimanapati, Z. Lin, V. Meunier, Y. Jung, J. Cha, S. Das, D. Xiao, Y. Son, M. S. Strano, V. R. Cooper, L. Liang, S. G. Louie, E. Ringe, W. Zhou, S. S. Kim, R. R. Naik, B. G. Sumpter, H. Terrones, F. Xia, Y. Wang, J. Zhu, D. Akinwande, N. Alem, J. A. Schuller, R. E. Schaak, M. Terrones, and J. A. Robinson: Recent Advances in Two-Dimensional Materials beyond Graphene. *ACS Nano* **9**(12), 11509 (2015).
12. C. R. Dean, A. F. Young, I. Meric, C. Lee, L. Wang, S. Sorgenfrei, K. Watanabe, T. Taniguchi, P. Kim, K. L. Shepard, and J. Hone: Boron nitride substrates for high-quality graphene electronics. *Nat. Nanotechnol.* **5**(10), 722 (2010).
13. M. H. Khan, H. K. Liu, X. Sun, Y. Yamauchi, Y. Bando, D. Golberg, and Z. Huang: Few-atomic-layered hexagonal boron nitride: CVD growth, characterization, and applications. *Mater. Today* No. June (2017).
14. M. Fuhrer, C. Lau, and A. MacDonald: Graphene: materially better carbon. *MRS*

Bull. **35**(April), 289 (2010).
15. R. R. Nair, P. Blake, A. N. Grigorenko, K. S. Novoselov, T. J. Booth, T. Stauber, N. M. R. Peres, and A. K. Geim: Fine Structure Constant Defines Visual Transparency of Graphene. *Science (80-.).* **320**(5881), 1308 (2008).
16. A. C. Ferrari and D. M. Basko: Raman spectroscopy as a versatile tool for studying the properties of graphene. *Nat. Nanotechnol.* **8**(4), 235 (2013).
17. A. Pakdel, Y. Bando, and D. Golberg: Nano boron nitride flatland. *Chem. Soc. Rev.* **43**(3), 934 (2014).
18. A. Falin, Q. Cai, E. J. G. Santos, D. Scullion, D. Qian, R. Zhang, Z. Yang, S. Huang, K. Watanabe, T. Taniguchi, M. R. Barnett, Y. Chen, R. S. Ruoff, and L. H. Li: Mechanical properties of atomically thin boron nitride and the role of interlayer interactions. *Nat. Commun.* **8**, 1 (2017).
19. L. H. Li and Y. Chen: Atomically Thin Boron Nitride: Unique Properties and Applications. *Adv. Funct. Mater.* **26**(16), 2594 (2016).
20. L. H. Li, E. J. G. Santos, T. Xing, E. Cappelluti, R. Roldán, Y. Chen, K. Watanabe, and T. Taniguchi: Dielectric screening in atomically thin boron nitride nanosheets. *Nano Lett.* **15**(1), 218 (2015).
21. K. S. Novoselov, A. K. Geim, S. V. Morozov, D. Jiang, Y. Zhang, S. V Dubonos, I. V. Grigorieva, and A. A. Firsov: Electric Field Effect in Atomically Thin Carbon Films. *Science (80-.).* **306**(5696), 666 (2004).
22. S. Das, M. Kim, J. Lee, and W. Choi: Synthesis, Properties, and Applications of 2-D Materials: A Comprehensive Review. *Crit. Rev. Solid State Mater. Sci.* **39**(4), 231 (2014).
23. A. C. Ferrari, F. Bonaccorso, V. Fal'ko, K. S. Novoselov, S. Roche, P. Bøggild, S. Borini, F. H. L. Koppens, V. Palermo, N. Pugno, J. a. Garrido, R. Sordan, A. Bianco, L. Ballerini, M. Prato, E. Lidorikis, J. Kivioja, C. Marinelli, T. Ryhänen, A. Morpurgo, J. N. Coleman, V. Nicolosi, L. Colombo, A. Fert, M. Garcia-Hernandez, A. Bachtold, G. F. Schneider, F. Guinea, C. Dekker, M. Barbone, Z. Sun, C. Galiotis, A. N. Grigorenko, G. Konstantatos, A. Kis, M. Katsnelson, L. Vandersypen, A. Loiseau, V. Morandi, D. Neumaier, E. Treossi, V. Pellegrini, M. Polini, A. Tredicucci, G. M. Williams, B. Hee Hong, J.-H. Ahn, J. Min Kim, H. Zirath, B. J. van Wees, H. van der Zant, L. Occhipinti, A. Di Matteo, I. a. Kinloch, T. Seyller, E. Quesnel, X. Feng, K. Teo, N. Rupesinghe, P. Hakonen, S. R. T. Neil, Q. Tannock, T. Löfwander, and J. Kinaret: Science and technology roadmap for graphene, related two-dimensional crystals, and hybrid systems. *Nanoscale* **7**(11), 4598 (2015).
24. L. Banszerus, M. Schmitz, S. Engels, J. Dauber, M. Oellers, F. Haupt, K. Watanabe, T. Taniguchi, B. Beschoten, and C. Stampfer: Ultrahigh-mobility graphene devices from chemical vapor deposition on reusable copper. *Sci. Adv.* **1**(6), e1500222 (2015).
25. S. Bae, H. Kim, Y. Lee, X. Xu, J.-S. Park, Y. Zheng, J. Balakrishnan, T. Lei, H. R. Kim, Y. Il Song, Y.-J. Kim, K. S. Kim, B. Ozyilmaz, J.-H. Ahn, B. H. Hong, and S. Iijima: Roll-to-roll production of 30-inch graphene films for transparent

electrodes. *Nat. Nanotechnol.* **5**(8), 574 (2010).
26. Y. Shi, C. Hamsen, X. Jia, K. K. Kim, A. Reina, M. Hofmann, A. L. Hsu, K. Zhang, H. Li, Z. Y. Juang, M. S. Dresselhaus, L. J. Li, and J. Kong: Synthesis of few-layer hexagonal boron nitride thin film by chemical vapor deposition. *Nano Lett.* **10**(10), 4134 (2010).
27. L. Song, L. Ci, H. Lu, P. B. Sorokin, C. Jin, J. Ni, A. G. Kvashnin, D. G. Kvashnin, J. Lou, B. I. Yakobson, and P. M. Ajayan: Large scale growth and characterization of atomic hexagonal boron nitride layers. *Nano Lett.* **10**(8), 3209 (2010).
28. R. Y. Tay, M. H. Griep, G. Mallick, S. H. Tsang, R. S. Singh, T. Tumlin, E. H. T. Teo, and S. P. Karna: Growth of large single-crystalline two-dimensional boron nitride hexagons on electropolished copper. *Nano Lett.* (2014).
29. G. Kim, A.-R. Jang, H. Y. Jeong, Z. Lee, D. J. Kang, and H. S. Shin: Growth of high-crystalline, single-layer hexagonal boron nitride on recyclable platinum foil. *Nano Lett.* **13**(4), 1834 (2013).
30. A.-R. Jang, S. Hong, C. Hyun, S. I. Yoon, G. Kim, H. Y. Jeong, T. J. Shin, S. O. Park, K. Wong, S. K. Kwak, N. Park, K. Yu, E. Choi, A. Mishchenko, F. Withers, K. S. Novoselov, H. Lim, and H. S. Shin: Wafer-Scale and Wrinkle-Free Epitaxial Growth of Single-Orientated Multilayer Hexagonal Boron Nitride on Sapphire. *Nano Lett.* **16**(5), 3360 (2016).
31. Y. Zhan, Z. Liu, S. Najmaei, P. M. Ajayan, and J. Lou: Large-area vapor-phase growth and characterization of MoS2 atomic layers on a SiO2 substrate. *Small* **8**(7), 966 (2012).
32. Y.-H. Lee, X.-Q. Zhang, W. Zhang, M.-T. Chang, C.-T. Lin, K.-D. Chang, Y.-C. Yu, J. T.-W. Wang, C.-S. Chang, L.-J. Li, and T.-W. Lin: Synthesis of large-area MoS2 atomic layers with chemical vapor deposition. *Adv. Mater.* **24**(17), 2320 (2012).
33. K.-K. Liu, W. Zhang, Y.-H. Lee, Y.-C. Lin, M.-T. Chang, C.-Y. Su, C.-S. Chang, H. Li, Y. Shi, and H. Zhang: Growth of large-area and highly crystalline MoS2 thin layers on insulating substrates. *Nano Lett.* **12**(3), 1538 (2012).
34. G. Eda and M. Chhowalla: Chemically derived graphene oxide: towards large-area thin-film electronics and optoelectronics. *Adv. Mater.* **22**(22), 2392 (2010).
35. S. Gilje, S. Han, M. Wang, K. L. Wang, and R. B. Kaner: A chemical route to graphene for device applications. *Nano Lett.* **7**(11), 3394 (2007).
36. C. L. Tsai, Y. Kobayashi, T. Akasaka, and M. Kasu: Molecular beam epitaxial growth of hexagonal boron nitride on Ni(111) substrate. *J. Cryst. Growth* **311**(10), 3054 (2009).
37. K. V Emtsev, A. Bostwick, K. Horn, J. Jobst, G. L. Kellogg, L. Ley, J. L. McChesney, T. Ohta, S. A. Reshanov, and J. Röhrl: Towards wafer-size graphene layers by atmospheric pressure graphitization of silicon carbide. *Nat. Mater.* **8**(3), 203 (2009).
38. X. Li, W. Cai, L. Colombo, and R. S. Ruoff: Evolution of graphene growth on Ni and Cu by carbon isotope labeling. *Nano Lett.* **9**(12), 4268 (2009).

39. X. Li, C. W. Magnuson, A. Venugopal, J. An, J. W. Suk, B. Han, M. Borysiak, W. Cai, A. Velamakanni, Y. Zhu, L. Fu, E. M. Vogel, E. Voelkl, L. Colombo, and R. S. Ruoff: Graphene films with large domain size by a two-step chemical vapor deposition process. *Nano Lett.* **10**(11), 4328 (2010).
40. F. Bonaccorso, A. Lombardo, T. Hasan, Z. Sun, L. Colombo, and A. C. Ferrari: Production and processing of graphene and 2d crystals. *Mater. Today* **15**(12), 564 (2012).
41. Y. Hao, M. S. Bharathi, L. Wang, Y. Liu, H. Chen, S. Nie, X. Wang, H. Chou, C. Tan, B. Fallahazad, H. Ramanarayan, C. W. Magnuson, E. Tutuc, B. I. Yakobson, K. F. McCarty, Y. Zhang, P. Kim, J. Hone, L. Colombo, and R. S. Ruoff: The role of surface oxygen in the growth of large single-crystal graphene on copper. *Science* **342**(6159), 720 (2013).
42. Y. Hao, L. Wang, Y. Liu, H. Chen, X. Wang, C. Tan, S. Nie, J. W. Suk, T. Jiang, T. Liang, J. Xiao, W. Ye, C. R. Dean, B. I. Yakobson, K. F. McCarty, P. Kim, J. Hone, L. Colombo, and R. S. Ruoff: Oxygen-activated growth and bandgap tunability of large single-crystal bilayer graphene. *Nat. Nanotechnol.* **11**(5), 426 (2016).
43. X. Li, C. W. Magnuson, A. Venugopal, R. M. Tromp, J. B. Hannon, E. M. Vogel, L. Colombo, and R. S. Ruoff: Large-area graphene single crystals grown by low-pressure chemical vapor deposition of methane on copper. *J. Am. Chem. Soc.* **133**(9), 2816 (2011).
44. Q. Li, H. Chou, J.-H. Zhong, J.-Y. Liu, A. Dolocan, J. Zhang, Y. Zhou, R. S. Ruoff, S. Chen, and W. Cai: Growth of adlayer graphene on Cu studied by carbon isotope labeling. *Nano Lett.* **13**(2), 486 (2013).
45. S. Nie, W. Wu, S. Xing, Q. Yu, J. Bao, S. Pei, and K. F. McCarty: Growth from below: bilayer graphene on copper by chemical vapor deposition. *New J. Phys.* **14**(9), 93028 (2012).
46. K. Lee and J. Ye: Significantly improved thickness uniformity of graphene monolayers grown by chemical vapor deposition by texture and morphology control of the copper foil substrate. *Carbon N. Y.* **100**, 441 (2016).
47. W. Fang, A. L. Hsu, R. Caudillo, Y. Song, A. G. Birdwell, E. Zakar, M. Kalbac, M. Dubey, T. Palacios, M. S. Dresselhaus, P. T. Araujo, and J. Kong: Rapid identification of stacking orientation in isotopically labeled chemical-vapor grown bilayer graphene by Raman spectroscopy. *Nano Lett.* **13**(4), 1541 (2013).
48. S. Chen, W. Cai, R. D. Piner, J. W. Suk, Y. Wu, Y. Ren, J. Kang, and R. S. Ruoff: Synthesis and Characterization of Large-Area Graphene and Graphite Films on Commercial Cu–Ni Alloy Foils. *Nano Lett.* **11**(9), 3519 (2011).
49. Y. Wu, H. Chou, H. Ji, Q. Wu, S. Chen, W. Jiang, Y. Hao, J. Kang, Y. Ren, R. D. Piner, and R. S. Ruoff: Growth Mechanism and Controlled Synthesis of AB-Stacked Bilayer Graphene on Cu–Ni Alloy Foils. *ACS Nano* **6**(9), 7731 (2012).
50. H. Wang, Y. Zhao, Y. Xie, X. Ma, and X. Zhang: Recent progress in synthesis of two-dimensional hexagonal boron nitride. *J. Semicond.* **38**(3), 031003 (2017).
51. G. R. Bhimanapati, N. R. Glavin, and J. A. Robinson: in *Semicond. Semimetals*,

1st ed. (Elsevier Inc., 2016), pp. 101–147.
52. A. Nagashima, N. Tejima, Y. Gamou, T. Kawai, and C. Oshima: Electronic dispersion relations of monolayer hexagonal boron nitride formed on the Ni(111) surface. *Phys. Rev. B* **51**(7), 4606 (1995).
53. S. M. Kim, A. Hsu, M. H. Park, S. H. Chae, S. J. Yun, J. S. Lee, D.-H. Cho, W. Fang, C. Lee, T. Palacios, M. Dresselhaus, K. K. Kim, Y. H. Lee, and J. Kong: Synthesis of large-area multilayer hexagonal boron nitride for high material performance. *Nat. Commun.* **6**, 8662 (2015).
54. A. Ismach, H. Chou, D. a Ferrer, Y. Wu, S. McDonnell, H. C. Floresca, A. Covacevich, C. Pope, R. Piner, M. J. Kim, R. M. Wallace, L. Colombo, and R. S. Ruoff: Toward the controlled synthesis of hexagonal boron nitride films. *ACS Nano* **6**(7), 6378 (2012).
55. S. Sonde, A. Dolocan, N. Lu, C. Corbet, M. J. Kim, E. Tutuc, S. K. Banerjee, and L. Colombo: Ultrathin, wafer-scale hexagonal boron nitride on dielectric surfaces by diffusion and segregation mechanism. *2D Mater.* **4**(2), 25052 (2017).
56. A. Ismach, H. Chou, P. Mende, A. Dolocan, R. Addou, S. Aloni, R. Wallace, R. Feenstra, R. S. Ruoff, and L. Colombo: Carbon-assisted chemical vapor deposition of hexagonal boron nitride. *2D Mater.* **4**(2), 025117 (2017).
57. H. Cho, S. Park, D.-I. Won, S. O. Kang, S.-S. Pyo, D.-I. Kim, S. M. Kim, H. C. Kim, and M. J. Kim: Growth kinetics of white graphene (h-BN) on a planarised Ni foil surface. *Sci. Rep.* **5**, 11985 (2015).
58. Y.-H. Lee, K.-K. Liu, A.-Y. Lu, C.-Y. Wu, C.-T. Lin, W. Zhang, C.-Y. Su, C.-L. Hsu, T.-W. Lin, K.-H. Wei, Y. Shi, and L.-J. Li: Growth selectivity of hexagonal-boron nitride layers on Ni with various crystal orientations. *RSC Adv.* **2**(1), 111 (2012).
59. C. Tan, X. Cao, X.-J. Wu, Q. He, J. Yang, X. Zhang, J. Chen, W. Zhao, S. Han, G.-H. Nam, M. Sindoro, and H. Zhang: Recent Advances in Ultrathin Two-Dimensional Nanomaterials. *Chem. Rev.* **117**(9), 6225 (2017).
60. D. Akinwande, N. Petrone, and J. Hone: Two-dimensional flexible nanoelectronics. *Nat. Commun.* **5**, 5678 (2014).
61. J.-H. Park, J. C. Park, S. J. Yun, H. Kim, D. H. Luong, S. M. Kim, S. H. Choi, W. Yang, J. Kong, K. K. Kim, and Y. H. Lee: Large-Area Monolayer Hexagonal Boron Nitride on Pt Foil. *ACS Nano* **8**(8), 8520 (2014).
62. S. Behura, P. Nguyen, S. Che, R. Debbarma, and V. Berry: Large-area, transfer-free, oxide-assisted synthesis of hexagonal boron nitride films and their heterostructures with MoS2 and WS2. *J. Am. Chem. Soc.* **137**(40), 13060 (2015).
63. Y.-C. Lin, N. Lu, N. Perea-Lopez, J. Li, Z. Lin, X. Peng, C. H. Lee, C. Sun, L. Calderin, P. N. Browning, M. S. Bresnehan, M. J. Kim, T. S. Mayer, M. Terrones, and J. a Robinson: Direct Synthesis of Van der Waals Solids. *ACS Nano* (2014).
64. Z. Liu, L. Song, S. Zhao, J. Huang, L. Ma, J. Zhang, J. Lou, and P. M. Ajayan: Direct growth of graphene/hexagonal boron nitride stacked layers. *Nano Lett.* **11**(5), 2032 (2011).
65. Q. Wu, S. K. Jang, S. Park, S. J. Jung, H. Suh, Y. H. Lee, S. Lee, and Y. J. Song:

In situ synthesis of a large area boron nitride/graphene monolayer/boron nitride film by chemical vapor deposition. *Nanoscale* **7**(17), 7574 (2015).
66. M. G. Hu, R. A. Geanangel, and W. W. Wendlandt: The thermal decomposition of ammonia borane. *Thermochim. Acta* **23**(2), 249 (1978).
67. A. Brockman, Y. Zheng, and J. Gore: A study of catalytic hydrolysis of concentrated ammonia borane solutions. *Int. J. Hydrogen Energy* **35**(14), 7350 (2010).
68. J. W. Suk, A. Kitt, C. W. Magnuson, Y. Hao, S. Ahmed, J. An, A. K. Swan, B. B. Goldberg, and R. S. Ruoff: Transfer of CVD-grown monolayer graphene onto arbitrary substrates. *ACS Nano* **5**(9), 6916 (2011).
69. J. Chan, A. Venugopal, A. Pirkle, S. McDonnell, D. Hinojos, C. W. Magnuson, R. S. Ruoff, L. Colombo, R. M. Wallace, and E. M. Vogel: Reducing extrinsic performance-limiting factors in graphene grown by chemical vapor deposition. *ACS Nano* **6**(4), 3224 (2012).
70. Y.-C. Lin, C.-C. Lu, C.-H. Yeh, C. Jin, K. Suenaga, and P.-W. Chiu: Graphene annealing: how clean can it be? *Nano Lett.* **12**(1), 414 (2012).
71. M. Hubáček and M. Ueki: Chemical Reactions in Hexagonal Boron Nitride System. *J. Solid State Chem.* **123**(2), 215 (1996).
72. A. Nag, K. Raidongia, K. Hembram, R. Datta, U. Waghmare, and C. Rao: Graphene analogues of BN: novel synthesis and properties. *ACS Nano* **4**(3), 1539 (2010).
73. A. Ismach, H. Chou, P. Mende, A. Dolocan, R. Addou, S. Aloni, R. Wallace, R. Feenstra, L. Colombo, and R. S. Ruoff: Carbon Assisted Chemical Vapor Deposition of Hexagonal Boron Nitride. *Submiss.* (2017).
74. S. Caneva, R. S. Weatherup, B. C. Bayer, R. Blume, A. Cabrero-Vilatela, P. Braeuninger-Weimer, M. B. Martin, R. Wang, C. Baehtz, R. Schloegl, J. C. Meyer, and S. Hofmann: Controlling Catalyst Bulk Reservoir Effects for Monolayer Hexagonal Boron Nitride CVD. *Nano Lett.* **16**(2), 1250 (2016).
75. W. Auwärter, M. Muntwiler, J. Osterwalder, and T. Greber: Defect lines and two-domain structure of hexagonal boron nitride films on Ni(1 1 1). *Surf. Sci.* **545**(1–2) (2003).
76. W. Auwärter, H. U. Suter, H. Sachdev, and T. Greber: Synthesis of One Monolayer of Hexagonal Boron Nitride on Ni(111) from B-Trichloroborazine (ClBNH)3. *Chem. Mater.* **16**(2), 343 (2004).
77. J. K. Hite, Z. R. Robinson, C. R. Eddy, and B. N. Feigelson: Electron Backscatter Diffraction Study of Hexagonal Boron Nitride Growth on Cu Single-Crystal Substrates. *ACS Appl. Mater. Interfaces* **7**(28), 15200 (2015).
78. L. Vitos, A. V. Ruban, H. L. Skriver, and J. Kollár: The surface energy of metals. *Surf. Sci.* **411**(1–2), 186 (1998).
79. H. Chou, A. Ismach, R. Ghosh, R. S. Ruoff, and A. Dolocan: Revealing the Planar Chemistry of Two-Dimensional Heterostructures At the Atomic Level. *Nat. Commun.* **6**(May), 1 (2015).
80. X. Wang, L. Tao, Y. Hao, Z. Liu, H. Chou, I. Kholmanov, S. Chen, C. Tan, N.

Jayant, Q. Yu, D. Akinwande, and R. S. Ruoff: Direct delamination of graphene for high-performance plastic electronics. *Small* **10**(4), 694 (2014).
81. N. Azzerri and R. L. Colombo: Surface diffusion measurements in nickel using a modified relaxation technique. *Metallography* **9**(3), 233 (1976).
82. P. S. Maiya and J. M. Blakely: Surface self diffusion and surface energy of nickel. *J. Appl. Phys.* **38**, 698 (1967).
83. H. Oh, J. Jo, Y. Tchoe, H. Yoon, H. Hwi Lee, S.-S. Kim, M. Kim, B.-H. Sohn, and G.-C. Yi: Centimeter-sized epitaxial h-BN films. *NPG Asia Mater.* **8**(11), e330 (2016).
84. M. Pons, M. Caillet, and A. Galerie: High-temperature oxidation of boron-implanted nickel. Comparison with ion-implanted iron and copper. *React. Solids* **2**(1–2), 125 (1986).
85. P. S. Barlow, R. A. Collins, and G. Dearnaley: Oxidation behaviour of ion-bombarded boron-coated nickel. *Surf. Coatings Technol.* **46**, 111 (1991).
86. C. Zhang, L. Fu, S. Zhao, Y. Zhou, H. Peng, and Z. Liu: Controllable co-segregation synthesis of wafer-scale hexagonal boron nitride thin films. *Adv. Mater.* **26**(11), 1776 (2014).
87. S. Caneva, R. S. Weatherup, B. Bayer, B. Brennan, S. J. Spencer, K. Mingard, A. Cabrero-Vilatela, C. Baehtz, A. J. Pollard, and S. Hofmann: Nucleation Control for Large, Single Crystalline Domains of Monolayer Hexagonal Boron Nitride via Si-Doped Fe Catalysts. *Nano Lett.* 150209115635009 (2015).
88. T. P. Beebe, D. W. Goodman, B. D. Kay, and J. T. Yates: Kinetics of the activated dissociative adsorption of methane on the low index planes of nickel single crystal surfaces. *J. Chem. Phys.* **87**(4), 2305 (1987).
89. H. Wise and J. Oudar: Material Concepts in Surface Reactivity and Catalysis (Elsevier, 1990).
90. R. M. Desrosiers, D. W. Greve, and A. J. Gellman: Decomposition of B2H6 on Ni(100). *J. Vac. Sci. Technol. A Vacuum, Surfaces, Film.* **15**(4), 2181 (1997).
91. J. M. Blakely and H. Mykura: Self Diffusion Measurements By the Mass Transfer Method *. *Acta Metall.* **9**(2), 23 (1961).
92. A. C. Ferrari and D. M. Basko: Raman spectroscopy as a versatile tool for studying the properties of graphene. *Nat. Nanotechnol.* **8**(4), 235 (2013).
93. K. F. Mak, C. Lee, J. Hone, J. Shan, and T. F. Heinz: Atomically thin MoS2: A new direct-gap semiconductor. *Phys. Rev. Lett.* **105**(13), 2 (2010).
94. H. Fang, C. Battaglia, C. Carraro, S. Nemsak, B. Ozdol, J. S. Kang, H. a Bechtel, S. B. Desai, F. Kronast, A. a Unal, G. Conti, C. Conlon, G. K. Palsson, M. C. Martin, A. M. Minor, C. S. Fadley, E. Yablonovitch, R. Maboudian, and A. Javey: Strong interlayer coupling in van der Waals heterostructures built from single-layer chalcogenides. *Proc. Natl. Acad. Sci. U. S. A.* **111**(17), 6198 (2014).
95. A. K. Geim and I. V Grigorieva: Van der Waals heterostructures. *Nature* **499**(7459), 419 (2013).
96. G. Fiori, F. Bonaccorso, G. Iannaccone, T. Palacios, D. Neumaier, A. Seabaugh, S. K. Banerjee, and L. Colombo: Electronics based on two-dimensional materials.

Nat Nanotechnol **9**(10), 768 (2014).
97. A. Hsu, H. Wang, Y. C. Shin, B. Mailly, X. Zhang, L. Yu, Y. Shi, Y. H. Lee, M. Dubey, K. K. Kim, J. Kong, and T. Palacios: Large-Area 2-D Electronics: Materials, Technology, and Devices. *Proc. IEEE* **101**(7), 1638 (2013).
98. M. C. Lemme, L.-J. Li, T. Palacios, and F. Schwierz: Two-dimensional materials for electronic applications. *MRS Bull.* **39**(08), 711 (2014).
99. S. J. Haigh, a Gholinia, R. Jalil, S. Romani, L. Britnell, D. C. Elias, K. S. Novoselov, L. a Ponomarenko, a K. Geim, and R. Gorbachev: Cross-sectional imaging of individual layers and buried interfaces of graphene-based heterostructures and superlattices. *Nat. Mater.* **11**(9), 764 (2012).
100. A. Pirkle, J. Chan, A. Venugopal, D. Hinojos, C. W. Magnuson, S. McDonnell, L. Colombo, E. M. Vogel, R. S. Ruoff, and R. M. Wallace: The effect of chemical residues on the physical and electrical properties of chemical vapor deposited graphene transferred to SiO2. *Appl. Phys. Lett.* **99**(12), 122108 (2011).
101. C.-C. Chen, Z. Li, L. Shi, and S. B. Cronin: Thermal interface conductance across a graphene/hexagonal boron nitride heterojunction. *Appl. Phys. Lett.* **104**(8), 081908 (2014).
102. A. G. F. Garcia, M. Neumann, F. Amet, J. R. Williams, K. Watanabe, T. Taniguchi, and D. Goldhaber-Gordon: Effective cleaning of hexagonal boron nitride for graphene devices. *Nano Lett.* **12**(9), 4449 (2012).
103. J.-H. Chen, C. Jang, S. Xiao, M. Ishigami, and M. S. Fuhrer: Intrinsic and extrinsic performance limits of graphene devices on SiO2. *Nat. Nanotechnol.* **3**(4), 206 (2008).
104. S. Haigh, A. Gholinia, R. Jalil, and S. Romani: Cross-sectional imaging of individual layers and buried interfaces of graphene-based heterostructures and superlattices. *Nat. Mater.* 2 (2012).
105. A. Benninghoven, F. G. Rüdenauer, and H. W. Werner: Secondary Ion Mass Spectrometry: Basic Concepts, Instrumental Aspects, Applications, and Trends (J. Wiley, 1987).
106. K. Iltgen: Optimized time-of-flight secondary ion mass spectroscopy depth profiling with a dual beam technique. *J. Vac. Sci. Technol. A Vacuum, Surfaces, Film.* **15**(3), 460 (1997).
107. L. Wang, Z. Chen, C. R. Dean, and T. Taniguchi: Negligible environmental sensitivity of graphene in a hexagonal Boron Nitride/Graphene/h-BN Sandwich structure. *ACS Nano* **6**(10), 9314 (2012).
108. G.-H. Lee, Y.-J. Yu, C. Lee, C. Dean, K. L. Shepard, P. Kim, and J. Hone: Electron tunneling through atomically flat and ultrathin hexagonal boron nitride. *Appl. Phys. Lett.* **99**(24), 243114 (2011).
109. X. Li, W. Cai, I. Jung, and J. An: Synthesis, characterization, and properties of large-area graphene films. *ECS Trans.* **19**(5), 41 (2009).
110. R. V Gorbachev, I. Riaz, R. R. Nair, R. Jalil, L. Britnell, B. D. Belle, E. W. Hill, K. S. Novoselov, K. Watanabe, T. Taniguchi, A. K. Geim, and P. Blake: Hunting for monolayer boron nitride: optical and Raman signatures. *Small* **7**(4), 465 (2011).

111. J. D. Zimmerman, B. E. Lassiter, X. Xiao, K. Sun, A. Dolocan, R. Gearba, D. a Vanden Bout, K. J. Stevenson, P. Wickramasinghe, M. E. Thompson, and S. R. Forrest: Control of interface order by inverse quasi-epitaxial growth of squaraine/fullerene thin film photovoltaics. *ACS Nano* **7**(10), 9268 (2013).
112. T. D. M. Elko-Hansen, A. Dolocan, and J. G. Ekerdt: Atomic Interdiffusion and Diffusive Stabilization of Cobalt by Copper During Atomic Layer Deposition from Bis (N-tert-butyl-N'-ethylpropionamidinato) Cobalt (II). *J. Phys. Chem. Lett.* **5**(7), 1091 (2014).
113. S. Hofmann: Sputter depth profile analysis of interfaces. *Reports Prog. Phys.* **61**(7), 827 (1998).
114. S. Hofmann: Profile reconstruction in sputter depth profiling. *Thin Solid Films* **398**–**399**, 336 (2001).
115. N. Sai, R. Gearba, A. Dolocan, J. R. Tritsch, W.-L. Chan, J. R. Chelikowsky, K. Leung, and X. Zhu: Understanding the Interface Dipole of Copper Phthalocyanine (CuPc)/C60: Theory and Experiment. *J. Phys. Chem. Lett.* **3**(16), 2173 (2012).
116. K. Q. Ngo, P. Philipp, Y. Jin, S. E. Morris, M. Shtein, J. Kieffer, and T. Wirtz: Analysis and fragmentation of organic samples by (low-energy) dynamic SIMS. *Surf. Interface Anal.* **43**(1–2), 88 (2011).
117. A. M. van der Zande, P. Y. Huang, D. a Chenet, T. C. Berkelbach, Y. You, G.-H. Lee, T. F. Heinz, D. R. Reichman, D. a Muller, and J. C. Hone: Grains and grain boundaries in highly crystalline monolayer molybdenum disulphide. *Nat. Mater.* **12**(6), 554 (2013).
118. S. R. Na, S. Rahimi, L. Tao, H. Chou, S. K. Ameri, D. Akinwande, and K. M. Liechti: Clean graphene interfaces by selective dry transfer for large area silicon integration. *Nanoscale* **8**(14), 7523 (2016).
119. X. Li, H. Zhu, K. Wang, A. Cao, J. Wei, C. Li, Y. Jia, Z. Li, X. Li, and D. Wu: Graphene-on-silicon schottky junction solar cells. *Adv. Mater.* **22**(25), 2743 (2010).
120. W. Jie, F. Zheng, and J. Hao: Graphene/gallium arsenide-based Schottky junction solar cells. *Appl. Phys. Lett.* **103**(23), 233111 (2013).
121. X. Miao, S. Tongay, M. K. Petterson, K. Berke, A. G. Rinzler, B. R. Appleton, and A. F. Hebard: High Efficiency Graphene Solar Cells by Chemical Doping. *Nano Lett.* **12**, 6 (2012).
122. L. Yang, X. Yu, M. Xu, H. Chen, and D. Yang: Interface engineering for efficient and stable chemical-doping-free graphene-on-silicon solar cells by introducing a graphene oxide interlayer. *J. Mater. Chem. A* **2**(40), 16877 (2014).
123. D. Xu, X. Yu, L. Zuo, and D. Yang: Interface engineering and efficiency improvement of monolayer graphene–silicon solar cells by inserting an ultra-thin LiF interlayer. *RSC Adv.* **5**(58), 46480 (2015).
124. E. Shi, H. Li, L. Yang, L. Zhang, Z. Li, P. Li, Y. Shang, S. Wu, X. Li, J. Wei, K. Wang, H. Zhu, D. Wu, Y. Fang, and A. Cao: Colloidal antireflection coating improves graphene-silicon solar cells. *Nano Lett.* **13**(4), 1776 (2013).
125. Y. Song, X. Li, C. Mackin, X. Zhang, W. Fang, T. Palacios, H. Zhu, and J. Kong:

Role of Interfacial Oxide in High-Efficiency Graphene–Silicon Schottky Barrier Solar Cells. *Nano Lett.* **15**(3), 2104 (2015).
126. K. S. Kim, Y. Zhao, H. Jang, S. Y. Lee, J. M. Kim, K. S. Kim, J.-H. Ahn, P. Kim, J.-Y. Choi, and B. H. Hong: Large-scale pattern growth of graphene films for stretchable transparent electrodes. *Nature* **457**(7230), 706 (2009).
127. Y. Song, W. Fang, R. Brenes, and J. Kong: Challenges and opportunities for graphene as transparent conductors in optoelectronics. *Nano Today* **10**(6), 681 (2015).
128. P. Kowalczewski and L. C. Andreani: Towards the efficiency limits of silicon solar cells: How thin is too thin? *Sol. Energy Mater. Sol. Cells* **143**, 260 (2015).
129. M. B. Schubert and J. H. Werner: Flexible solar cells for clothing. *Mater. Today* **9**(6), 42 (2006).
130. M. J. Yun, S. I. Cha, S. H. Seo, and D. Y. Lee: Highly Flexible Dye-sensitized Solar Cells Produced by Sewing Textile Electrodes on Cloth. *Sci. Rep.* **4**, 5322 (2014).
131. T. Jiao, D. Wei, J. Liu, W. Sun, S. Jia, W. Zhang, Y. Feng, H. Shi, and C. Du: Flexible solar cells based on graphene-ultrathin silicon Schottky junction. *RSC Adv.* **5**, 73202 (2015).
132. K. Ruan, K. Ding, Y. Wang, S. Diao, Z. Shao, X. Zhang, and J. Jie: Flexible graphene/silicon heterojunction solar cells. *J. Mater. Chem. A* **3**(27), 14370 (2015).
133. J. Ahn, H. Chou, and S. K. Banerjee: Graphene-Al2O3-silicon heterojunction solar cells on flexible silicon substrates. *J. Appl. Phys.* **121**(16) (2017).
134. A. C. Ferrari: Raman spectroscopy of graphene and graphite: Disorder, electron–phonon coupling, doping and nonadiabatic effects. *Solid State Commun.* **143**(1–2), 47 (2007).
135. A. C. Ferrari, J. C. Meyer, V. Scardaci, C. Casiraghi, M. Lazzeri, F. Mauri, S. Piscanec, D. Jiang, K. S. Novoselov, S. Roth, and A. K. Geim: Raman spectrum of graphene and graphene layers. *Phys. Rev. Lett.* **97**(18), 187401 (2006).
136. Y. Shi, K. K. Kim, A. Reina, M. Hofmann, L. J. Li, and J. Kong: Work function engineering of graphene electrode via chemical doping. *ACS Nano* **4**(5), 2689 (2010).
137. K. K. Kim, A. Reina, Y. Shi, H. Park, L. J. Li, Y. H. Lee, and J. Kong: Enhancing the conductivity of transparent graphene films via doping. *Nanotechnology* **21**(28), 285205 (2010).
138. E. U. Onyegam, D. Sarkar, M. M. Hilali, S. Saha, L. Mathew, R. A. Rao, R. S. Smith, D. Xu, D. Jawarani, R. Garcia, M. Ainom, and S. K. Banerjee: Realization of dual-heterojunction solar cells on ultra-thin ~ 25 μ m, flexible silicon substrates. *Appl. Phys. Lett.* **104**(15), 153902 (2014).
139. R. A. Rao, L. Mathew, S. Saha, S. Smith, D. Sarkar, R. Garcia, R. Stout, A. Gurmu, E. Onyegam, and D. Ahn: in *Photovolt. Spec. Conf. (PVSC), 2011 37th IEEE* (IEEE, 2011), pp. 1504–1507.
140. L. Mathew and D. Jawarani: US7749884 B2 (2010).
141. Y. H. Lee, Y.-J. Kim, S. M. J. Han, H. Song, and J. Oh: Sub-5 μm-thick spalled

single crystal Si foils by decoupling crack initiation and propagation. *Appl. Phys. Lett.* **109**(13), 132101 (2016).
142. X. Li, Y. Zhu, W. Cai, M. Borysiak, B. Han, D. Chen, R. D. Piner, L. Colombo, and R. S. Ruoff: Transfer of large-area graphene films for high-performance transparent conductive electrodes. *Nano Lett.* **9**(12), 4359 (2009).
143. Y. Chen, X. L. Gong, and J. G. Gai: Progress and Challenges in Transfer of Large-Area Graphene Films. *Adv. Sci.* **3**(8) (2016).
144. D. K. Schroder: Semiconductor Material and Device Characterization (John Wiley & Sons, 2006).
145. J.-H. Meng, X. Liu, X.-W. Zhang, Y. Zhang, H.-L. Wang, Z.-G. Yin, Y.-Z. Zhang, H. Liu, J.-B. You, and H. Yan: Interface engineering for highly efficient graphene-on-silicon Schottky junction solar cells by introducing a hexagonal boron nitride interlayer. *Nano Energy* 1 (2016).
146. Y. Tsuboi, F. Wang, D. Kozawa, K. Funahashi, S. Mouri, Y. Miyauchi, T. Takenobu, and K. Matsuda: Enhanced photovoltaic performances of graphene/Si solar cells by insertion of a MoS_2 thin film. *Nanoscale* **7**(34), 14476 (2015).
147. R. Hezel and K. Jaeger: Low-temperature surface passivation of silicon for solar cells. *J. Electrochem. Soc.* **136**(2), 518 (1989).
148. B. Hoex, S. B. S. Heil, E. Langereis, M. C. M. Van De Banden, and W. M. M. Kessels: Ultralow surface recombination of c-Si substrates passivated by plasma-assisted atomic layer deposited Al2O3. *Appl. Phys. Lett.* **89**(4) (2006).
149. B. Hoex, J. Schmidt, P. Pohl, M. C. M. Van de Sanden, and W. M. M. Kessels: Silicon surface passivation by atomic layer deposited Al2O3. *J. Appl. Phys.* **104**(4), 44903 (2008).
150. H. C. Card and E. H. Rhoderick: Studies of tunnel MOS diodes I. Interface effects in silicon Schottky diodes. *J. Phys. D. Appl. Phys.* **4**(10), 1589 (1971).
151. M. Houssa: High k Gate Dielectrics (CRC Press, 2003).
152. L. Liao, J. Bai, Y. Qu, Y. Huang, and X. Duan: Single-layer graphene on Al2O3/Si substrate: better contrast and higher performance of graphene transistors. *Nanotechnology* **21**(1), 015705 (2010).
153. A. Y. Serov, Z.-Y. Ong, M. V. Fischetti, and E. Pop: Theoretical analysis of high-field transport in graphene on a substrate. *J. Appl. Phys.* **116**(3), 034507 (2014).
154. T. Cui, R. Lv, Z.-H. Huang, S. Chen, Z. Zhang, X. Gan, Y. Jia, X. Li, K. Wang, D. Wu, and F. Kang: Enhanced efficiency of graphene/silicon heterojunction solar cells by molecular doping. *J. Mater. Chem. A* **1**(18), 5736 (2013).
155. S. M. Kim, A. Hsu, M. H. Park, S. H. Chae, S. J. Yun, J. S. Lee, D.-H. Cho, W. Fang, C. Lee, T. Palacios, M. Dresselhaus, K. K. Kim, Y. H. Lee, and J. Kong: Synthesis of large-area multilayer hexagonal boron nitride for high material performance. *Nat. Commun.* **6**, 8662 (2015).
156. S. K. Jang, J. Youn, Y. J. Song, and S. Lee: Synthesis and Characterization of Hexagonal Boron Nitride as a Gate Dielectric SI. *Sci. Rep.* **6**, 30449 (2016).